RCA

Review

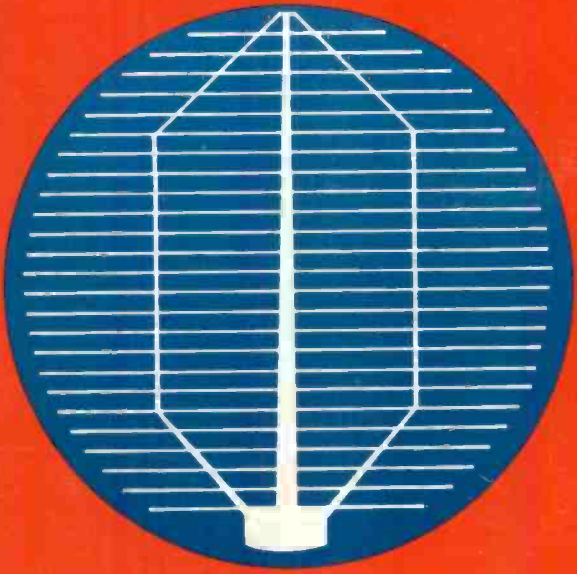

June 1980 Volume 41 No. 2

RCARCI 41 (2) 131-270 (1980)

RCA Review, published quarterly in March, June, September and December by RCA Research and Engineering, RCA Corporation, Princeton, New Jersey 08540. Entered as second class matter July 3, 1950 under the Act of March 3, 1879. Second-class postage paid at Princeton, New Jersey, and at additional mailing offices. Effective January 1, 1978, subscription rates as follows: United States and Canada: one year $8.00, two years $14.00, three years $18.00; in other countries, one year $8.60, two years $15.20, three years $19.80. Single copies (except for special issues) up to five years old $3.00.

The cover figure represents the front side of a single-crystal silicon solar cell. The white pattern is the metallization grid and the bonding area used for electrical lead attachment. The cell was coated with an antireflective film of TiO_2 by the spray-on process described in the Kern/Tracy paper in this issue. The antireflection coating, which exhibits a deep blue interference color on silicon, is only one quarter-wavelength thick but effects an increase in the photovoltaic conversion efficiency of the cell by over 40 percent.

RCA
Review

RCA Review (ISSN 0033-6831) is a technical journal published quarterly by RCA Research and Engineering in cooperation with the subsidiaries and divisions of RCA.

Contents

RCA Corporation

Editorial Advisory Board

Editor **Ralph F. Ciafone**

Associate Editors

Titanium Dioxide Antireflection Coating for Silicon Solar Cells by Spray Deposition*

Werner Kern and Edwin Tracy**

RCA Laboratories, Princeton, NJ 08540

Abstract—A high-speed production process is described for depositing a single-layer, quarter-wavelength thick antireflection coating of titanium dioxide on metal-patterned single-crystal silicon solar cells for terrestial applications. Controlled atomization spraying of an organotitanium solution was selected as the most cost effective method of film deposition using commercial automated equipment. The optimal composition consists of titanium isopropoxide as the titanium source, *n*-butyl acetate as the diluent solvent, sec-butanol as the leveling agent, and 2-ethyl-1-hexanol to render the material uniformly depositable. Application of the process to the coating of circular, large-diameter solar cells with either screen-printed silver metallization or with vacuum evaporated Ti/Pd/Ag metallization showed increases of over 40 percent in the electrical conversion efficiency. Optical characteristics, corrosion resistance, and several other important properties of the spray-deposited film are reported. Experimental evidence is presented that indicates a wide tolerance in the coating thickness upon the overall efficiency of the cell. In addition, considerations pertaining to the optimization of AR coatings in general are discussed and a comprehensive critical survey of the literature is presented.

1. Introduction

1.1 Overview of Paper

The objective of the work described was the development of a low-cost, mass production process for producing an antireflection (AR) coating

---

* This work was performed as part of the Low-Cost Solar Array project, Jet Propulsion Laboratory, California Institute of Technology under Contract 954868, and was jointly sponsored by the U.S. Department of Energy through an agreement with NASA.

** Present address: SERI Branch 641, Golden, Colorado 80401.

on silicon photovoltaic cells. The process was to be applicable to cells featuring saw-cut and chemically etched (non-planar) surfaces of single-crystal silicon with metallization grids of screen-printed and fired conductive inks.

Several processes were explored and tested for technical feasibility and cost viability. These processes included physical vapor deposition techniques, such as vacuum evaporation and sputtering processes; chemical vapor deposition at normal and reduced pressure, including plasma-enhanced deposition; and mechanical deposition techniques, such as spinning, dipping/draining, and spraying, followed by chemical conversion of the deposit to a solid AR film.

Several materials of high refractive index were tested for their suitability with respect to optical properties, cost effectiveness, and stability. Materials considered included dielectrics such as TiO_2, TiO_2-SiO_2, SiO, Ta_2O_5, ZrO_2, HfO_2, Si_3N_4 and $Si_xN_yH_z$, as well as electrically conductive and transparent semiconductors such as SnO_2, In_2O_3, In_2O_3:Sn, and SnO_2:Sb.

Our final analysis indicated that spray-deposition of organo-metallic titanium compounds followed by chemical reaction to produce films of

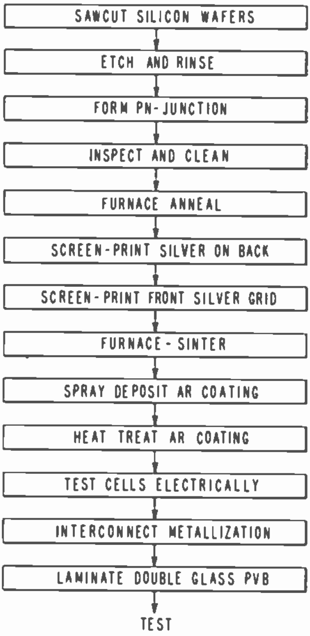

Fig. 1—Major steps in the manufacturing sequence of single-crystal silicon solar cells indicating the application of the spray-on AR coating.

titanium dioxide met the stated requirements most effectively. Consequently, we developed a process on this basis, with the successful result reported in this paper.

In addition, a very comprehensive review of the literature on AR coatings for solar cells is presented which covers references to early 1980.[1-54] Also, fundamental optical considerations are discussed, since they form the basis of our observations for optimizing the properties of AR films.

Our work on AR coatings has been part of a larger, partly government-sponsored RCA solar cell development project designed to devise manufacturing sequences that should ultimately be suitable for the mass production of single-crystal silicon photovoltaic array modules at a cost of less than $700 per peak kW (in 1980 dollars). The major steps in the manufacturing sequence investigated at RCA are presented in the flow chart in Fig. 1; it shows at which step in the sequence the AR coating is applied.

1.2 Historical Perspective and Literature Review

Lord Rayleigh is generally credited with the first experimental observation of the antireflection effect in 1887, while Bauer offered the first successful theoretical treatment based on interference effects in 1934.[44] Since then the theory and application of optical interference phenomena has been well documented, especially with respect to thin film filters, and has resulted in a multi-million dollar optical coating industry. Antireflection coatings for solar cells, however, are a relatively recent event beginning primarily in the 1960's with the advent of photovoltaics as remote power sources for spacecrafts and satellites.

A comprehensive search of the literature from 1968 to the present was made in an effort to review the types of antireflection coatings used, the deposition methods employed, and the various solar cell substrates upon which they were deposted. Table 1 lists the articles we found to be the most informative; they were carefully reviewed and selected from the initial search and rated with respect to the extent of the author's discussion of antireflection characteristics of the coating (E for extensive, M for moderate, and L for limited in scope). The references themselves are given at the end of the paper. The table shows the AR coating material, deposition method, and substrate, respectively, in terms of the author's original description. In the few cases where the deposition method was not specified, the abbreviation n.s. indicates the omission.

None of the articles reviewed that were published prior to 1971 were deemed appropriate to include in the table. A quarter-wavelength

Table 1—Survey Abstract of Literature References Pertaining to AR Coatings

Ref. (Scope of Discussion of AR Coatings)/Year (E = extensive, M = moderate, L = limited)	AR Coating	Deposition Method (n.s. = not specified)	Solar Cell Substrate
1 (M)/1979	Indium tin oxide (ITO)	Neutralized ion beam sputtering	Single crystal silicon (SIS type)
2 (E)/1979	TiO_2	Spin-on or dipping with air and vacuum baking at ~325°C	Silicon (round wafer and dendritic-web ribbon type)
3(L)/1979	SnO_2	300°C–400°C pyrolysis of $SnCl_4$–H_2O–ethyl acetate solutions	Single-silicon and polysilicon SnO_2/n-Si
4(L)/1979	SiO	Evaporation	n^+p single crystal silicon (MIS type)
49 (M)/1979	SnO_2	Hydrolysis of $SnCl_4$	n^+/p single crystal silicon
50 (E)/1979	ZnS, cryolite	n.s.	Ag/p-Si (Schottky barrier type)
5 (L)/1978	SiO	n.s.	Cr/oxide/p-silicon (MIS type)
6 (M)/1978	TiO_2, In_2O_3	n.s.	Single and polycrystalline silicon
7 (L)/1978	SnO_2	400°C oxidation of tetramethyltin	Thin film polycrystalline silicon
8 (L)/1978	Ta_2O_5, Nb_2O_5	n.s.	GaAs (polycrystalline AMOS type)
9 (L)/1978	TiO_2	80–100°C hydrolysis of tetraiospropyl titanate	Thin film GaAs (MOS type)
51 (L)/1978	SiO_2-Ta_2O_5	rf diode sputtering of SiO_2-Ta_2O_5 Targets	Fused Silica (for integrated optical circuits)
10 (L)/1978	Oxide of n^+GaAs	Electrolytic anodization	Shallow-homojunction $n^+/p/p^+$ single crystal GaAs
11 (L)/1978	SiO_x, TiO_x, Ta_xO_y, Ta_2O_5	n.s.	Silicon (non-reflective, violet type cell)
12 (L)/1978	All types (review article)	n.s.	All types
13 (M)/1978	TiO_2	100–400°C hydrolysis of tetraisopropyl titanate	Silicon, GaAs
14 (L)/1978	Krylon, SiO_x TiO_x	n.s. 80–100°C hydrolysis of tetraisopropyl titanate	Polycrystalline GaAs on tungsten/graphite substrates
15 (M)/1978	SiO	Evaporation	Single crystal and polycrystalline InP/Cds
16 (M)/1977	TiO_x SiO_2	Spin-on CVD and thermal	Silicon (MIS inversion layer type)
17 (M)/1977	Si_3N_4, SiO_2 dual layer	n.s.	Epi-silicon (concentrator type)
18 (M)/1977	ZnS	Evaporation	Al/p-type silicon (MIS type)

Table 1—(Contd)

Ref. (Scope of Discussion of AR Coatings)/Year (E = extensive, M = moderate, L = limited)	AR Coating	Deposition Method (n.s. = not specified)	Solar Cell Substrate
19 (L)/1977	TiO_2-SiO_2 dual layer	n.s.	pnn^+ silicon (concentrator type)
52 (L)/1977	TiO_2-SiO_2	Spin-on	p^+/n silicon
20 (M)/1977	Sb_2O_3	E-beam and laser beam evaporation	Silicon (AMOS type)
21 (E)/1977	SiO_2, TiO_x, Ta_2O_5	n.s.	All types
22 (L)/1977	Glycerol	n.s.	Cds/CdTe heterojunction
23 (L)/1977	SnO_2	E-beam evaporation	SnO_2/Si heterojunction
24 (M)/1977	In_2O_3	Vacuum evaportion	Silicon (MIS type)
25 (M)/1977	SiO, TiO_x, Ta_2O_5, CeO_2	n.s.	Silicon
26 (L)/1977	MgF_2	n.s.	n-ITO/p-ITO
27 (L)/1977	ZrO_2, Si_3N_4	n.s.	α-silicon (Schottky barrier type)
28 (M)/1976	TiO_2	Spin-on of tetrabutyl titanate	Silicon
29 (M)/1976	Arsenic-doped SiO_2	Spin-on	Diffused n^+-p-p^+ silicon
30 (L)/1976	Silicon nitride	n.s.	Textured silicon
31 (L)/1976	SiO	Evaporation	Cr/p-silicon (MIS type)
32 (E)/1976	Ta_2O_5	Evaporation	Any metal/ semiconductor or Schottky barrier type
33 (E)/1976	Ta_2O_5, Nb_2O_5	E-beam evaporation	Silicon (violet or Comsat non-reflective types)
34 (E)/1976	Ta_2O_5	Thermal oxidation of metallic Ta	Silicon
35 (M)/1975	SiO, TiO_x, Ta_2O_5, Nb_2O_5	n.s.	Silicon
36 (M)/1975	Ta_2O_5, Nb_2O_5	n.s.	Silicon (conventional, violet, and non-reflective type)
37 (M)/1975	Ta_2O_5	E-Gun evaporation	GaAs, GaAs/P (Schottky barrier type)
38 (M)/1975	TiO_2-SiO_2	Spin-on	Silicon (single crystal, p/n diffused junction)
	SiO	n.s.	
39 (L)/1975	Ta_2O_5, SiO_x	n.s.	Silicon (violet and non-reflective types)
53 (M)/1975	Ta_2O_5	n.s.	Silicon (non-reflective type)
40 (M)/1975	Ta_2O_5, SiO_x	n.s.	Silicon (shallow junction type)
41 (L)/1975	SIPOS	n.s.	Multilayer epi on silicon
42 (E)/1975	Ta_2O_5	E-beam evaporation	Au/GaAs (AMOS type)
43 (E)/1974	Ta_2O_5, Nb_2O_5, SiO_x, TiO_x	n.s.	Silicon (violet type)

Table 1—(Contd)

Ref. (Scope of Discussion of AR Coatings)/Year (E = extensive, M = moderate, L = limited)	AR Coating	Deposition Method (n.s. = not specified)	Solar Cell Substrate
44 (E)/1974	SiO, Si_3N_4, Ta_2O_5 (single and dual layers)	n.s.	Silicon
45 (L)/1974	SiO	Vacuum deposition	Silicon (Schottky barrier type)
46 (M)/1973	TiO_2, SiO	Vacuum deposition	Cr-silicon (Schottky barrier type)
47 (M)/1972	SiO_2 CeO_2 TiO	Thermally grown E-beam evaporation Reactive evaporation in an O_2 atmosphere	n/p-silicon
48 (L)/1972	SiO_x, TiO_x	E-beam evaporation	Silicon
54 (L)/1972	Ge	CVD of GeH_4 300–450°C	Silicon (no cells)
	Si	CVD of SiH_4 325–575°C	Germanium (no cells)

thickness of SiO ($n \sim 1.8$) was practically the only AR coating used on solar cells prior to 1970[25,35] due to an oversimplification in matching the refractive index of silicon to that of air. Until 1972, investigators in the field were still primarily concerned with improving the characteristics of the cell itself and probably considered AR coatings a peripheral subject. Furthermore, the improvement in J_{sc} afforded by SiO was apparently considered satisfactory at that stage of development.

Some time later, the realization that cells needed to be encapsulated with an organic adhesive and cover glass prompted research workers to examine the utilization of higher refractive index coatings ($n \sim 2.0$) such as TiO_x, Si_3N_4, and CeO_2. Subsequently, with the arrival of solar cells having improved short-wavelength response (violet cells), high-index coatings with good transmission extending to $\lambda = 0.35$ μm for AM = 0 applications were investigated such as Ta_2O_5 and Nb_2O_5.

The current mode of research emphasis is basically two-fold: (1) low-cost AR coatings capable of high-speed automation for large-scale terrestial applications (AM = 1,2), and (2) transparent conductive coatings, such as In_2O_3, SnO_2, or In_2O_3:Sn, for reducing or eliminating the inactive cell area masked by the opaque top-contact metallization.

The survey table should prove useful to those interested in quickly acquiring information about a specific AR coating material or about a coating used on a specific type of cell. In addition to the more commonly accepted types of AR coatings, such as SiO, TiO_2, Si_3N_4, Ta_2O_5, SnO_2, etc., Table 1 lists some rather atypical coating trials with films such as acrylics, glycerol, and SIPOS. A considerable effort has been expended to include all pertinent papers in this survey to the best of our awareness and judgment.

1.3 Basic Optical Considerations

The percentage of incident energy reflected from a given substrate depends on the relative indices of refraction across the interface and the angle at which the radiation strikes the surface. With normal incidence, the reflectance (R) from the silicon substrate is given by the Fresnel relation:

$$R = [(n_1 - n_2)/(n_1 + n_2)]^2, \qquad [1]$$

where n_1 = refractive index of silicon and n_2 = refractive index of the surrounding media. For an air interface ($n_2 = 1$), a considerable amount of energy is wasted in reflection from a silicon surface due to its high index of refraction ($n_{si} = 3.9$ for radiation of $\lambda = 0.6\ \mu$m).[61] Substitution of these refractive index values into Eq. [1] results in a reflectance loss of 35%. Without the application of an AR coating, only 65% of the available sunlight is coupled into the cell. Thus, a 100% effective AR coating resulting in zero reflectance and zero absorbance has the theoretical capability of increasing the electrical output of a silicon solar cell by 54%.

Quarter-wave antireflection (QWAR) coatings of appropriate refractive index and thickness reduce reflection from the silicon surface by reflecting light from the film's front and back surfaces such that the light waves are of equal amplitude and are 180° out of phase, resulting in destructive interference. To satisfy the laws of energy conservation, this light must necessarily be transmitted into the cell rather than being reflected. The optimum index of refraction (n_{ar}) of a thin film to achieve this effect is governed by the following relation:

$$n_{ar} = \sqrt{n_1 n_2}. \qquad [2]$$

Appropriate substitution results in $n_{ar} \sim 2.0$ and $n_{ar} \sim 2.4$ for silicon cells in air ($n_2 = 1$) and under a plastic-laminated glass cover ($n_2 = 1.5$), respectively.

The film thickness (T_f) to achieve minimum reflectance with a QWAR coating is given by

$$T_f = \frac{1}{4}\frac{\lambda_{min}}{n_{ar}}, \qquad [3]$$

where λ_{min} is the wavelength of light at which a minimum is desired. For silicon solar cells λ_{min} is usually chosen equal to or very near 0.6 μm, resulting in an optimum thickness of $T_f \sim 750$ Å for an AR coating with a refractive index of 2.2.

Eqs. [1], [2], [3], and related mathematical examples represent an over-simplification of the parameters that must be analyzed to determine the refractive index and thickness of a QWAR coating and are applicable for only one particular wavelength and temperature. Further discussion of these parameters with respect to broad-band antireflection across the solar spectrum and ramifications with respect to spray-on TiO_2 coatings will be postponed to a later section of this paper in order to preserve continuity of presentation. (See Sec. 3.5.)

2. Experimental

2.1 Materials

Several organotitanium compounds, numerous types of organic solvents, a few organic surfactant additives, and several acid catalysts were used during the investigation for formulating suitable spray mixtures. The best spray mixture, "RCA-TiO_2", is specified in Table 2; it is based on titanium(IV) isopropoxide and was used for processing most of the cells and samples described in this paper. Three other titanium sources were comparatively evaluated using analogous mixture formulations: titanium(IV) ethoxide, titanium(IV) butoxide, and "Titaniumsilicafilm C"

Table 2—Components Used to Prepare the Optimized Final Titanium Spray Liquid RCA-TiO_2

Function	Compound	Specifications	Composition		Source
			(vol)	(vol %)	
Titanium source	titanium(IV) isopropoxide, $Ti[OCH(CH_3)_2]_4$	mp 20°C, d 0.9550 g/cm^3	9.2	7.7	Alfa Division, Ventron Corp.
Diluent solvent	n-butylacetate, $CH_3CO_2(CH_2)_3CH_3$	99+%, bp 127°C, d 0.882 g/cm^3	20	17	Aldrich Chemical Co.
Sprayability agent	2-ethyl-1-hexanol, $CH_3(CH_2)_3CH(C_2H_5)CH_2OH$	99+%, bp 180–182°C, d 0.832–0.833 g/cm^3	40	33	Eastman Organic Chemicals
Leveling agent	sec-butanol, $C_2H_5CH(OH)CH_3$	99%, bp 98°C, d 0.808 g/cm^3	50	42	Aldrich Chemical Co.
	or isopropanol, $(CH_3)_2CHOH$	99+% anhydrous, bp 82–83°C, d 0.785 g/cm^3			Aldrich Chemical Co.
Spray liquid	Composite mixture		119.2	100	(prepared from the above ingredients)

spin-on solution concentrate of proprietary composition (Emulsitone Company, Whippany, NJ).

The mixture is prepared by diluting the titanium source liquid with the *n*-butyl acetate. The 2-ethyl-1-hexanol mixed with the sec-butanol is then added with agitation. The mixture, if stored in the dark in a tightly sealed and full bottle, has a shelf life of at least several months.

Substrate materials consisted of single-crystal, 7.5-cm diameter silicon solar cells made primarily with $POCl_3$-diffused junction, and metal patterned by screen-printed silver ink followed by firing resulting in a film thickness of typically 8 μm. Cells with vacuum-evaporated Ti/Pd/Ag metallization of about 2.7 μm film thickness were also used, mainly for comparison. Test substrates consisted of 7.5-cm diameter single-crystal silicon wafers polished on one side. Plates of fused quartz and microscope glass slides were used for optical transmission measurements.

Chemicals for cleaning test substrates included a hot mixture (1:1 by volume) of H_2O_2 30% – H_2SO_4 98%, and of H_2O – HF 49% (1:1 by volume) for stripping oxide layers from silicon wafers.

Solar cells usually required no cleaning prior to spray coating. They were handled and stored to be as free from contamination as possible. Cells that did require cleaning were rinsed in methylethylketone followed by *n*-butyl acetate and spin-drying.

2.2 Spray Deposition and Heating Equipment

Several types and commercial makes of spray machines were examined for suitability for our purpose. The spray machine (Fig. 2) we used in our laboratory for the pilot production tests was a Series 9000 Autocoater from Zicon Corporation, Mount Vernon, NY. This unit for batch operation is a smaller and less automated version of the fully automated inline Series 11000 machine we consider suitable for large-scale continuous mass production. The spraying is conducted in a closed, class 100, laminar downdraft clean-booth supplied with HEPA-filtered air which is conditioned to a relative humidity not exceeding 45%. The exhaust air exits through a flow-adjustable duct. The spray liquid is contained in a nitrogen-pressurized stainless steel tank, as seen in Fig. 2, and is transported through stainless steel tubing to the liquid reservoir above the spray nozzle. The reciprocating spray gun (Figs. 3 and 4) traverses prependicularly to the substrate cells, which are moved by an incremental advancing transport mechanism. The machine operates automatically over a wide range of programmed cycles adjustable by front-panel controls. A solvent-resistant final filter (0.5-μm Millipore Filter,

Fig. 2—Zicon Series 9000 Autocoater.

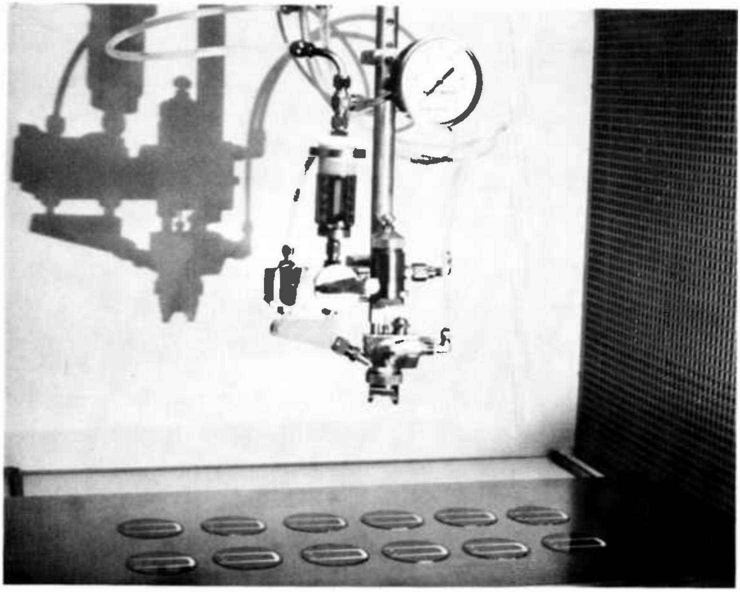

Fig. 3—Spray gun assembly.

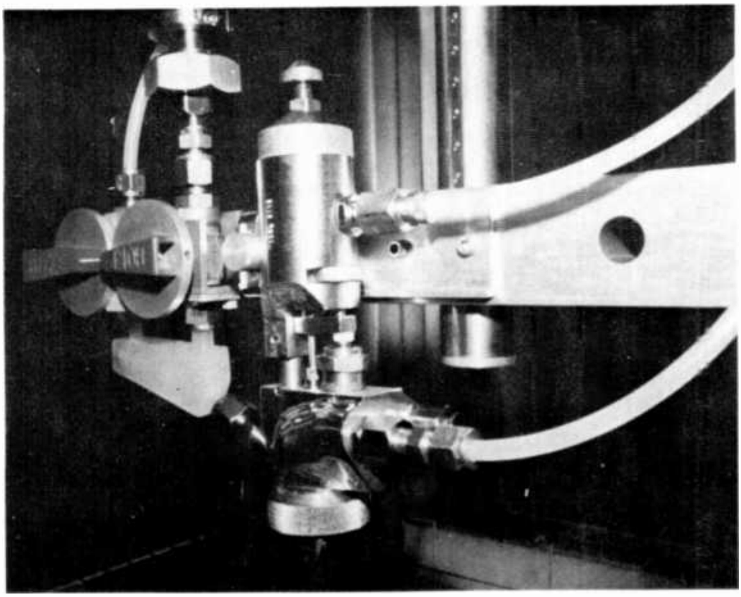

Fig. 4—Close-up of atomization spray gun.

Millipore Corporation) has been placed at the exit port of the spray solution reservoir above the spray head to remove any traces of particulates. The diameter of the spray nozzle used in our work was 0.33 mm (0.013 in.).

It is important that the air in the spray booth be dust-free and of low humidity (≤45% RH). High humidity can cause premature reaction of the atomized droplets in the gas phase, leading to hazy film deposits.

A perforated metal tray, elevated 1.5 cm above the stainless steel substrate platform, for holding the cells has normally been used to simulate the support mechanism featured in the in-line spray coating machine for continuous mass production. No problems with backside contamination by the spray occurred, in contrast to techniques based on dipping and draining. Our machine accepts comfortably up to 15 cells of 7.5 cm diameter. A series of cells being spray coated is shown in Fig. 5.

A vapor-exhaust convection oven with thermostatic temperature control is used for the initial drying of a batch of coated cells. We have used a gravity convection oven, but recommend a forced air convection type for improved performance. The subsequent heat treatments at higher temperature of large batches of cells are carried out in convection ovens in which the cells can be positioned vertically in trays or cassettes for greatly increased packing density. For laboratory processing we have

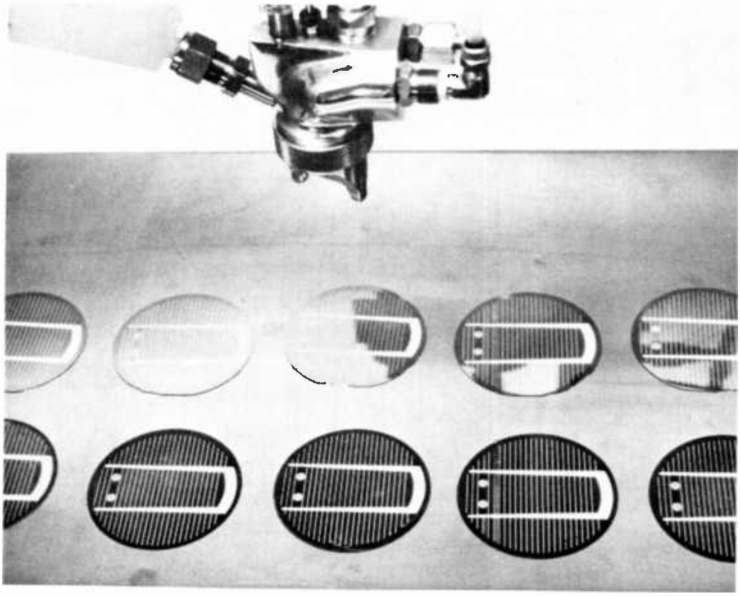

Fig. 5—Solar cells being spray-coated: front row coated, rear row uncoated.

used Corning PC-100 Pyroceram hotplates covered with an aluminum plate for uniform heat distribution.

A layout plan for large-scale, automated, continuous in-line production spraying and heat treatments is shown in Fig. 6. The cells are transfered

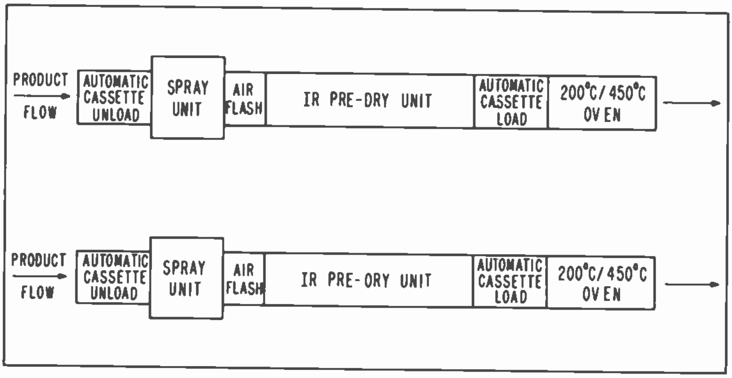

Fig. 6—Layout plan for large-scale production equipment. This equipment would occupy an area 20 × 40 feet.

in and out of the conveyor system by automatic cassette unloaders and reloaders. The estimated production throughput is 4500 cells per hour per machine. The combined output would correspond to 55 million cells annual production, assuming continuous operation and 90% machine uptime. On the basis of 0.548 W/cell and a 99% yield this quantity represents a total of 30 megawatts per year.

2.3 Film Deposition and Heating Treatments

The step at which the AR coating is applied has been shown in the manufacturing sequence flow chart in Fig. 1. The procedure for spray coating cells for laboratory production is described below.

The cells as received from metallization sintering are placed on the perforated substrate tray. The glass doors of the spray booth are closed and the room air displaced with dry, filtered air. The automatic spray cycle is activated 10 seconds later. Spray coating of one load of cells takes half a minute. After the substrate table has returned to its starting position the doors are opened and the substrate tray is transferred into the convection oven.

The automatic spray cycle of the machine can be adjusted according to the specific requirements of film thickness and throughput. Of the various variable factors, the source delivery pressure is the major variable utilized for adjusting the amount of solution sprayed, thereby controlling the resulting solid film thickness. We have typically used a liquid delivery pressure of 6.97 kPa (28 in. H_2O). The atomization spray pressure and the spray gun-to-substrate distance can be used as secondary variables, but were kept constant at 207 kPa (30 psig) and 17.8 cm with all other parameters maintained at a specific setting.

The first heat treatment immediately after the spray deposition of the liquid film is performed in a convection oven set to an air temperature of 95°C. A 40-sec heating period in the oven has been found equivalent to a previously used 30-sec heating on a hot plate at 70°C, as determined by comparing refractive index and thickness changes for the two techniques. The humidity level in the first solvent evaporation and film drying oven should also be low to assure the formation of clear films. Several trays filled with a thick bed of anhydrous calcium sulfate desiccant (Drierite, The W. A. Hammond Drierite Company) remain permanently loaded in the oven.

The solid but soft and still solvent-soluble film is next treated at 200°C in room air. We found, by measurements of thickness, refractive index, and solubility, that substantial property changes have occured by the end of this treatment. Ambient moisture and oxygen might aid in the reaction to transform the organometallic to essentially titanium dioxide.

However, there is no need for controlling the ambient atmosphere other than keeping it clean.

The third and final heat treatment is designed to remove the last traces of organic solvents, to complete the hydrolytic reaction to TiO_2, and to densify the film to obtain a stable structure of maximum refractive index. A temperature of 450°C in room air or oxygen is needed to accomplish these objectives. For practical purposes a period of 30 seconds is sufficient for each of the heat treatments (200°C and 450°C) if done on hot plates in air. Processing batch-wise in an oven or continuously in a tube or tunnel furnace is, of course, much more economical even though it requires a longer period of time to achieve thermal equilibration.

2.4 Metallization Bondability After AR Coating

The surface of the metallization grid collector pad must be free of AR coating in order to permit effective bonding of cell-to-cell interconnects. The simplest technique, suitable for laboratory applications, is masking of the pad with a special solvent-resistive polyethylene pressure tape with acrylic adhesive prior to spraying (Tape No. 480, 3M Company, St. Paul, Minn.). The tape tab is readily peeled off after coating but before heat treatments, leaving a clean and bondable surface.

Mechanical and chemical techniques can be used for automated high-speed processing. Selective mechanical removal of the AR coating can be accomplished most readily by momentary application of an automatic ultrasonic vibrating or buffing tool combined with vacuum suction to remove the debris. Alternatively, since the solder connection techniques used require fluxing of the bonding area, a flux composition can be applied that contains a fluoride capable of selectively dissolving the thin AR coating. Rinsing with a jet of deionized water prevents metal corrosion problems.

2.5 Processing Control and Analytical Instrumentation

An Orthoplan universal large-field microscope (Leitz) with a TV projection screen (RCA) was used for optical scanning and inspection of coated cells in differential interference contrast.

An AutoEL-II automatic ellipsometer (Rudolph Research) with an accuracy of delta of 0.1° and psi of 0.05° was used for measuring thickness and refractive index of the AR films on test samples and on cells. A multiple adjustable sample stage, an auto-collimating alignment and viewing telescope, and special optics allow precision measurements of areas down to approximately 50-μm spots. The system uses a helium-neon laser (λ = 6328 Å) as the light source. A computerized data reduction unit and printer expedites high-speed data analysis. Some of the measurements were carried out using a manual broad-beam ellipsometer with an Hg light source ($\lambda = 5461$ Å).

An Alpha-Step surface profilometer (Tencor Instruments) served to measure the dimensions of surface features and metallization grids, as well as to double-check the ellipsometric AR film thicknesses.

Precision grating spectrophotometers (Cary model 14 CMR and Perkin-Elmer model 457) were used for measuring reflectance, transmittance, and infrared absorption of the films on test substrates.

Substrate temperatures during the heat treatments were measured with a calibrated thermocouple thermometer (Digital-Heat Prober by W. Wahl Corporation).

Electrical characterization of solar cells before and after AR-coating was done by measuring current-voltage and power output under simulated AM-1 illumination and determining the values of open circuit voltage (V_{oc}), short circuit current (I_{sc}), fill factor (FF), and electrical conversion efficiency (η).

The manually operated electrical test system had three 300-W ELH quartz-iodine lamps mounted on a photographic stand to provide an approximately 7.5-cm diameter circle of uniform light intensity. The solar cell under test was mounted on a gold-plated copper baseplate by means of a vacuum hold-down. The metal baseplate formed one contact to the solar cell and was the system ground. The current and voltage contacts were made to the front-side bus bar of the solar cell by means of flexible gold-ball-tipped metal fingers. The voltage contact was connected to the middle of the bus bar on the solar cell, while two current contacts were used, one on either end of the bus bar (Fig. 7).

The temperature of the cell was monitored by a thermocouple mounted underneath the solar cell in a groove in the baseplate. The temperature was maintained at 28°C by a thermoelectric cooler attached to the baseplate. The lamps were powered from the ac lines through an autotransformer. The voltage applied to the lamps was kept at 90 V to prolong the life of the ELH lamps. The I-V and power-voltage curves were obtained from an electronic circuit that sweeps a resistive load from zero to infinity across the solar cell in a few seconds.

Calibration of the lamps was obtained by placing a secondary standard solar cell, obtained from NASA-Lewis,* in the sample holder and setting the lamp–sample distance to give the short-circuit current appropriate for AM-1 conditions (100 mW/cm^2). Another standard cell was separately mounted on the sample baseplate and its short-circuit current was continuously monitored. Thus, if the lamp output changed slightly

---

* Reference cell No. 49, provided by NASA Lewis Research Center, Cleveland, Ohio.

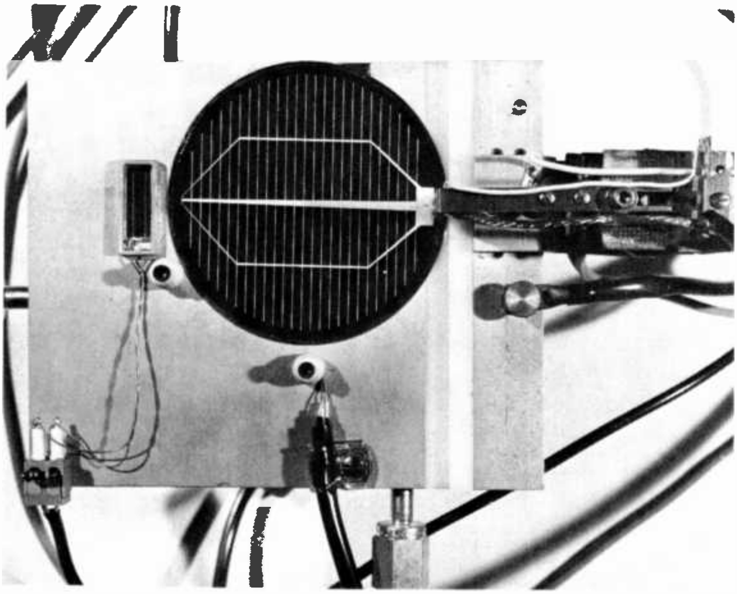

Fig. 7—Photograph of cell testing stage showing reference cell mounted adjacent to the 7.5-cm diameter cell being measured.

during a series of measurements, corrections could be made without remounting the standard cell. The calibration and measurement procedure followed that specified by NASA-Lewis in their publication NASA TM X-71771.

A calculator-based automatic probe system designed for high-speed electrical testing of the *I-V* characteristics under illumination was put into operation later in the program, in conjunction with a computerized data acquistion and analysis system.

3. Results and Discussion

3.1 Spray Liquid Composition

The following parameters must be considered in formulating a successful solution system for spray application: component solubility and miscibility characteristics, rate of solvent evaporation, surface tension and wettability, flow properties, viscosity, formation of azeotropes, chemical reactivity, cost, toxicity, and long-range stability of the mixture. The liquid mixture to be sprayed must have a viscosity compatible with the available optimal orifice sizes of the spray nozzle and the pressure range of the equipment. The sprayed-on microdroplets must spread locally on the substrate surface and coalesce to form a continuous and homogeneous liquid film of uniform composition and thickness even though the substrate surface is not perfectly smooth. Spreading must not be excessive to avoid build-up or depletion along the periphery of the cell or along the metallization grid lines. After reaction to a solid film the final coating must have good adhesion and integrity, be reasonably uniform in thickness over the entire cell surface, be free of haze and gross structural imperfections, and be chemically and physically stable; above all it must exhibit on silicon solar cell substrates an optimum index of refraction with minimum reflectance and absorbance in the visible wavelength mid-region.

Initial experiments were conducted empirically to determine the effects of different organic solvents, singly and in combination, on mixing with various ratios with the organotitanium source reagents. A great many solvent combinations were eliminated on the basis of incompatibility with the reagent, as manifested by solution immiscibility, color or gel formation, turbidity, cloudiness, precipitation, separation of components during drying of the liquid film, and haze or crystallite formation in the reacted solid film.

Film deposition in the preliminary studies was done by centrifugal spinning of small amounts of liquid mixtures on silicon wafers. This technique is much faster than spray deposition and was adequate for initial screening tests.

As a result of this work we found that a mixture for successful spray deposition must contain, in addition to the organotitanium primary reactant, the following components: (1) an inert diluent solvent consisting of a simple carboxylic acid ester; (2) a solution leveling agent, typically a low-molecular weight aliphatic alcohol; and (3) an agent that possesses optimal vapor pressure and viscosity characteristics to render the mixture successfully sprayable.

We found n-butyl acetate most effective as the diluent solvent. The titanium source material is first diluted with this solvent to form a clear, single-phase system. Other esters, ketones, alcohols, and hydrocarbons proved less successful or useless.

An important ingredient that renders the diluted titanium source suitable for atomization spraying and processing to form the AR film of the required quality is 2-ethyl-1-hexanol. The physical characteristics of this high-molecular weight alcohol are unique in that they impart to the mixture the ability to effect spreading of the liquid evenly across the substrate. This effect is due to the favorable surface tension and viscosity characteristics of 2-ethyl-1-hexanol which promote wetting and improve the uniformity of the film. Furthermore, this alcohol has an appropriate vapor measure (6 torr at 70°C,[55] the temperature of the first drying step), causing it to evaporate slowly enough so that the liquid film is not disrupted during the evaporation. Therefore, a uniform liquid film can be applied to the substrate and dried to form a uniform continuous coating on the substrate. Other high-molecular weight alcohols with similar physical properties were tested but proved either less effective or exhibited problems such as toxicity, irritation, or high cost.

Certain low-molecular weight aliphatic alcohols exhibit a leveling effect when added to the spray liquid, probably due to surface tension changes. Without this leveling agent the sprayed-on liquid mixture thickens along the metallization grid lines. The effect can be reversed by adding isopropanol, resulting in thinning along the metallization grid lines if an appropriate quantity is added. A carefully balanced ratio can effect leveling of the liquid film along the metallization grid lines, resulting in a solid AR film of practically uniform thickness throughout the surface of the solar cell areas between grid lines. The exact ratio depends on the thickness and morphology of the metalization system and must be optimized by empirical tests.

Due to undesirable side effects, the isopropanol leveling agent was subsequently replaced by sec-butanol which we found to be preferable because of its lowered chemical reactivity in the mixture, while retaining the leveling effectiveness. This reduced reactivity results in a longer shelf life of the spray liquid, greatly reduces clogging of the atomization spray nozzle, and minimizes the formation of airborne particulates during spraying. An additional advantage is the higher boiling point[56] and thus lower evaporation rate, which is the same as that of the *n*-butyl acetate solvent.[56]

Addition of surfactants to improve the wetting characteristics and of thickening agents to modify the solution viscocity were tested but found unnecessary to achieve the desired results. The incorporation of acids (HCO_2H, CH_3CO_2H, HCl, HNO_3, and HF) as potential catalysts to initiate hydrolysis was also found unnecessary.

For production work, titanium(IV) isopropoxide was used exclusively as the source for the titanium to prepare the "RCA-TiO_2" spray mixture. No advantages were found by using purified (by fractional crystallization) forms of this compound.

As noted already, several other organotitanium sources were used experimentally for comparison. These included titanium ethoxide, titanium butoxide, and "Titaniumsilicafilm C" concentrate. None of these were found superior to titanium isopropoxide; i.e., the ethoxide-based mixtures are unstable and the commercial preparation is considerably more expensive, besides not being any more effective.

Numerous compositional ratios for these mixture components were spray tested. The mixture that has consistently yielded the best results has been defined in Table 2. The exact proportions can be varied within reasonable limits without deleterious effects.

AR films with refractive indices of less than two (1.5–2.0) can be obtained with the RCA-TiO_2 spray liquid by adding appropriate amounts of a silicon alkoxide, such as tetraethoxysilane, to the titanium alkoxide spray liquid to form films of binary TiO_2-SiO_2 mixtures. However, since AR coatings for solar cells require a high refractive index no such addition is necessary or desirable.

3.2 Spray Machine Parameters

At least fifteen factors can be varied in the automatic spray system used in our work to provide the desired film thickness. These variables include (1) source solution delivery pressure, (2) atomization spray pressure, (3) gun-to-substrate distance, (4) propellant gas, (5) orifice size, (6) needle size, (7) spreader, (8) inserts, (9) gun-to-substrate distance, (10) solution flow rate, (11) number of spray guns, (12) spray gun traverse speed, (13) substrate advance rate, (14) source solution composition and reactant concentration, and (15) post-deposition heat treatments.

The first three variables are most easily manipulated for controlling film thickness with a given source solution. Three settings for each of these variables were selected to test their effect over the film-thickness range of interest. All other factors were held fixed at settings we considered near optimum. The propellant gas was nitrogen, the orifice size was 0.31 mm (12 mils), and a single spray gun was used, although multiple guns would be used in large-scale production. The standard titanium isopropoxide-based spray liquid was used with polished silicon wafers as the substrate. The results are summarized in Table 3 and are graphically presented in Figs. 8–10. All three graphs exhibit a slight curvature over the test range of practical interest. The film thickness

Table 3—AR Film* Thickness as a Function of Three Machine Variables

Source Liquid Delivery Pressure (kPa)	Source Liquid Delivery Pressure (in. H_2O)	Spray Atomization Gauge Pressure (kPa)	Spray Atomization Gauge Pressure (psig)	Spray-Gun to Substrate Distance (cm)	Spray-Gun to Substrate Distance (in.)	Film* Thickness (Å)
4.98	20	172	25	14.0	5.5	560
7.47	30	172	25	14.0	5.5	750
9.96	40	172	25	14.0	5.5	840
7.47	30	138	20	16.5	6.5	680
7.47	30	172	25	16.5	6.5	640
7.47	30	207	30	16.5	6.5	550
7.47	30	172	25	11.4	4.5	740
7.47	30	172	25	14.0	5.5	680
7.47	30	172	25	16.5	6.5	640

* TiO_2 from the standard titanium isopropoxide-based spray liquid after post-deposition heat treatments for 30 s each at 70, 200, and 450°C.

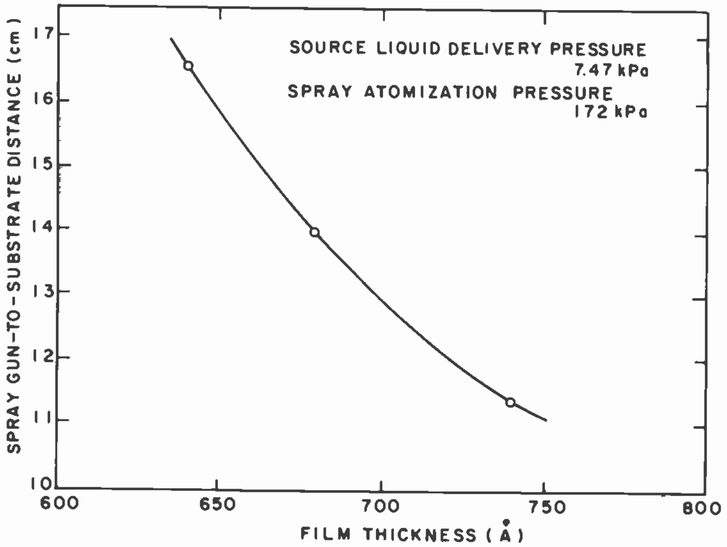

Fig. 8—Effect of spray-gun-to-substrate distance on film thickness.

increases with increasing source solution delivery pressure, with decreasing atomization spray pressure, and with decreasing gun-to-substrate distance. The uniformity of the AR film over the 7.5-cm-diameter

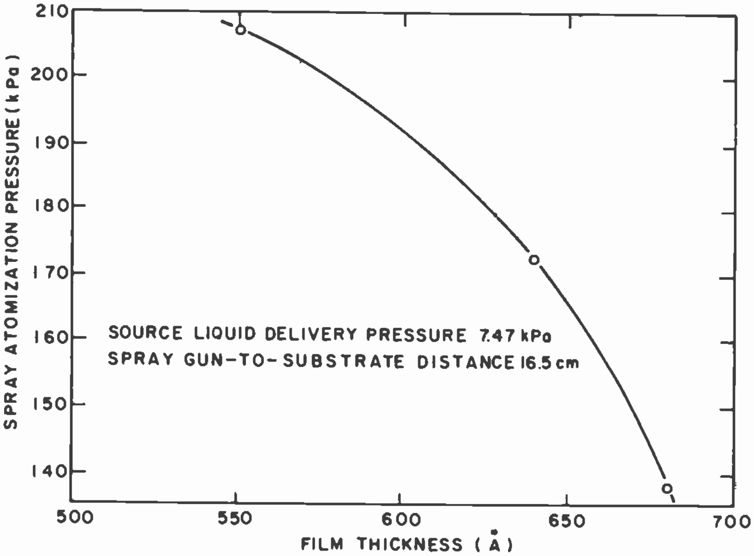

Fig. 9—Effect of spray atomization pressure on film thickness.

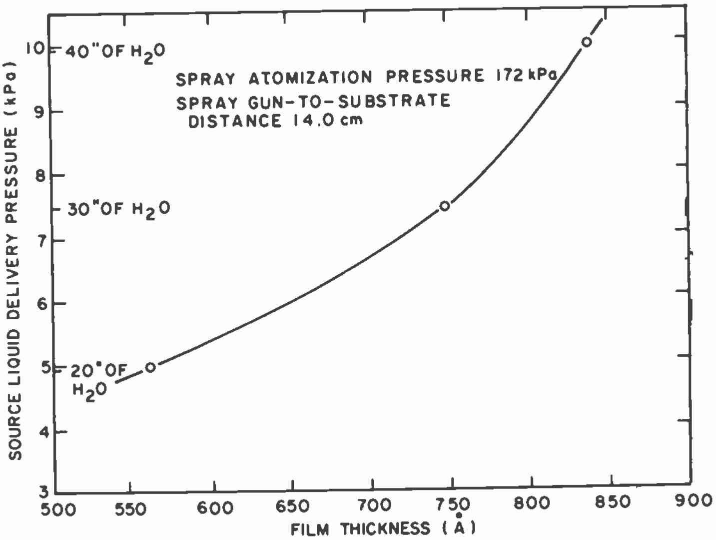

Fig. 10—Effect of source liquid delivery pressure on film thickness.

test wafers was excellent throughout, demonstrating that any of the three machine variables can be used to fine-tune the thickness with good uniformity.

3.3 Effects of Heat Treatments On Film Properties

3.3.1 Purpose and Sequence of Heat Treatments

The objective of the heat treatments is the evaporation of the organic solvents from the sprayed liquid film and the chemical transformation of the organotitanium component to the final solid TiO_2 film. The process must be conducted without adversely disrupting the film integrity and uniformity. Next to the spray deposition sequence, the heating process is the most critical and important step in successful creation of the AR coating. It determines the optical, physical, and chemical properties of the film, and therefore requires careful optimization.

We have been using three sequential heat treatment steps, each intended for a specific function. The first step at a temperature of 70°C on a hot plate, or, preferably, at 95°C air temperature in a convection oven, vaporizes nearly all of the solvents. Concurrently, definite changes of the organotitanium compound take place at this temperature, probably by partial hydrolysis. The resulting gel-like film is solid but is still soft and soluble in the *n*-butyl acetate solvent.

The second step is conducted at 200°C in room air. Extensive changes in the film occur during this heat treatment in which the organotitanium is transformed to titanium oxide by a pyrolytic decomposition reaction. Ambient oxygen and water vapor may play some role in this reaction, but experimental evidence has shown that their presence is not essential. There is no need for rigidly controlling the ambient atmosphere. However, very high moisture levels (such as steam atmospheres) are deleterious during all heat treatments; they cause hazy films due to the formation of particulate titanium hydroxide agglomerates.

The third and final heat treatment at 450°C in room air or oxygen drives off remaining OH-groups and any organic solvents that have remained from the previous steps, completes the thermal decomposition to TiO_2, and densifies the film creating a stable structure of maximum index of refraction. Higher temperatures than 450°C, or heating periods longer than specified, have little additional effect on the properties of the film, as will be shown.

Infrared spectroscopic measurements, solvent solubility tests, chemical reactivity in various ambients, and thickness and refractive index changes resulting from the heating treatments have indicated the nature of the chemical transformation to TiO_2. Titanium alkoxides are readily hydrolyzable and do not require the preparation of soluble partially hydrolyzed polymerizable species for forming glassy oxide films as would be the case for less reactive metal-organic compounds, such as silicon alkoxides.[2,57–59] Consequently, stable dilutions of titanium alkoxides can be prepared with anhydrous organic solvents. On evaporation of the solvents the film of titanium alkoxide reacts with moisture in the air resulting in partial hydrolysis with the formation of titanium hydroxide and the corresponding alcohol. The first heat treatment below 100°C accelerates hydrolysis significantly. Subsequent heating at 200°C and 450°C in air leads to dehydration, pyrolytic decomposition, vaporization of residual organic components, and densification of the film. A well-adherent, amorphous, and stable coating forms that consists of essentially TiO_2. Transformation from the initial deposit after solvent evaporation to the final coating after the 450°C heating step proceeds smoothly as is evident from the gradual changes in film thickness and refractive index. Heating for extended periods of times at 450°C or heating at higher temperatures does not significantly change the film thickness or refractive index but leads to the appearance of an undesirable crystalline phase (anatase) that tends to increase optical absorption and that greatly decreases solubility in hydrofluoric acid.

The effects of the heat treatments on film thickness, refractive index, absorbance, transmittance, reflectance, structure, and corrosion resistance are discussed below for films prepared from the titanium(IV) isopropoxide-based spray solution.

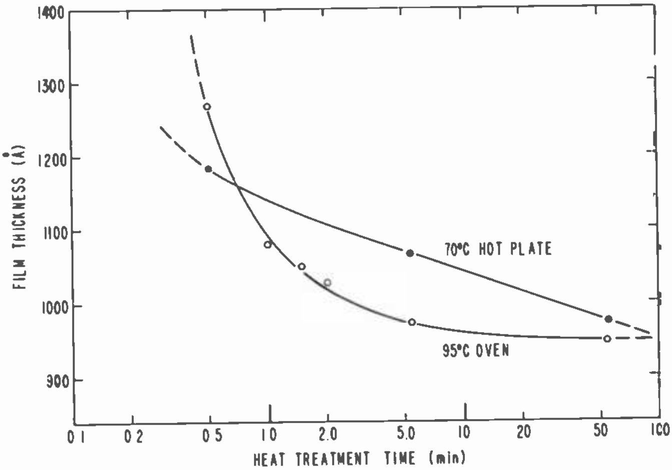

Fig. 11—Film thickness as a function of the initial heat treatment technique and duration.

3.3.2 *Film Thickness*

The effect of the initial heat treatment technique (hot plate or oven) in air on film thickness is shown in Fig. 11. The quantity of spray solution deposited in all of the tests in this and the next section was selected to yield a final film thickness of 670 Å after the 450°C-heating. The graph

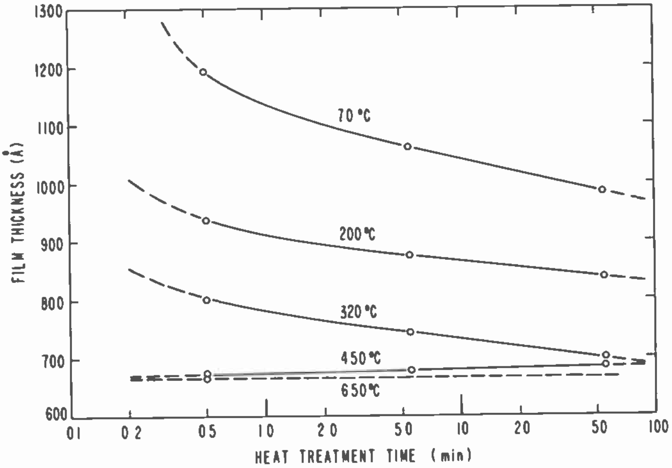

Fig. 12—Film thickness as a function of heating time at different temperatures. Hotplate technique was used. Ambient was room air except for the 650°C samples which were done in N_2 to prevent oxidation of the Si substrate.

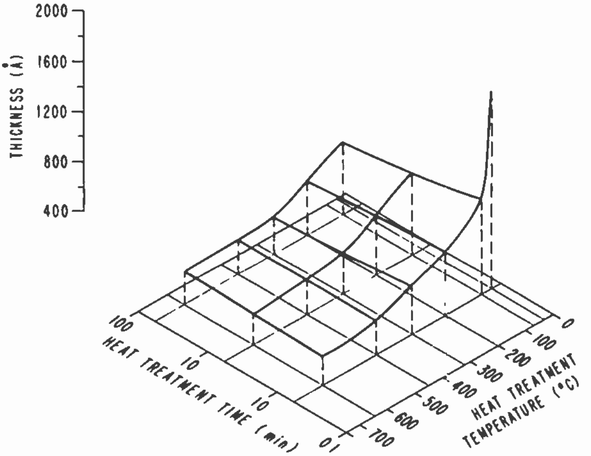

Fig. 13—Three-dimensional plot showing effects of heating time at different hotplate temperatures on film thickness.

indicates that oven-heating at 95°C is somewhat more effective for extended time periods than heating on the hot plate. However, for practical considerations we have maintained the time at a minimum compatable with the desired results and have chosen a 40-sec oven heating as our standard procedure, which is equivalent to a 30-sec hot plate heating. Subsequent heating at higher temperatures overrides effects that would result from extended periods of heating at lower temperatures.

The effect of hot plate heating at temperatures from 70° to 650°C for 0.50, 5.5, and 55.5 min on film thickness is presented in Fig. 12. It can be seen that, for heat treatments at 450°C and beyond, the film thickness attains a minimum in the first 30 sec. A very slight increase in thickness with time occurs at this temperature, which may be associated with the formation of a crystalline TiO_2 phase. A three-dimensional contour plot, which depicts the temperature/time/thickness relationship more clearly and allows useful interpolations, is shown in Fig. 13.

3.3.3 Index of Refraction

The effects of heating mode, temperature, and time on the index of refractions of the film are presented in Figs. 14–16. The same samples were used for this analysis as those for the thickness measurements in the previous sections (Figs. 11–13). The trends associated with refractive-index increase are complimentary to those of the thickness decrease. An additional 1% increase in refractive index from 2.18 to 2.20 can be obtained by extending the heating duration at 450°C from 30 sec to 5.5 min.

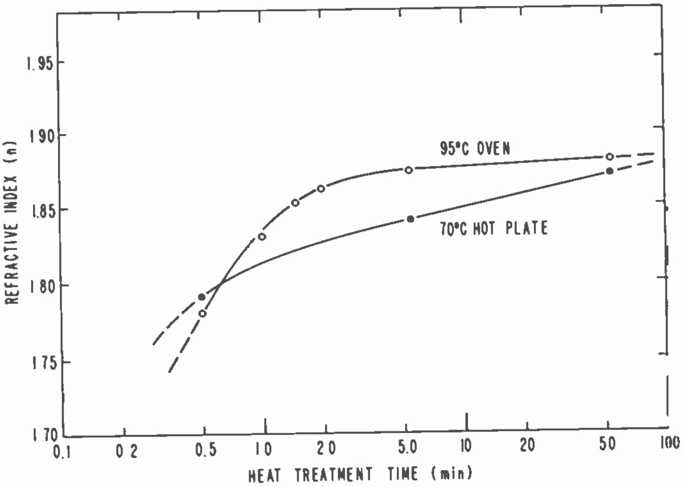

Fig. 14—Refractive index as a function of the initial heat treatment technique and duration.

No additional increase results by extending the heating duration to 1 h. For practical and economical purposes this small improvement does not warrant the extra time or higher temperature that would be required. Furthermore, excessive heat treatments must be avoided as they may cause degradation of the cells.

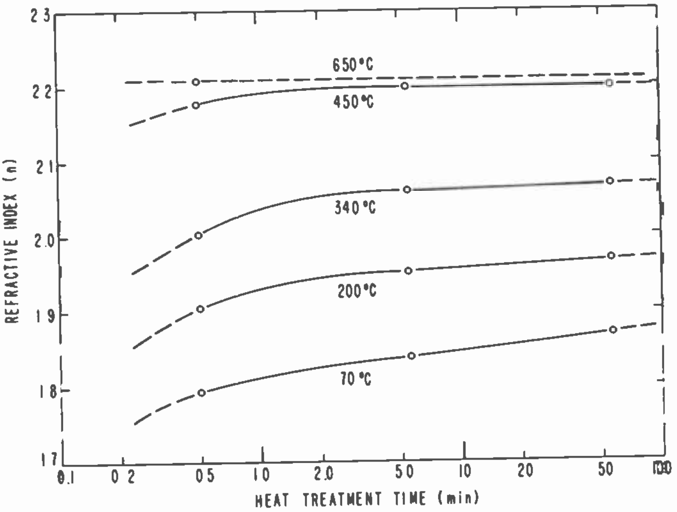

Fig. 15—Same as Fig. 12, but showing effects on refractive index.

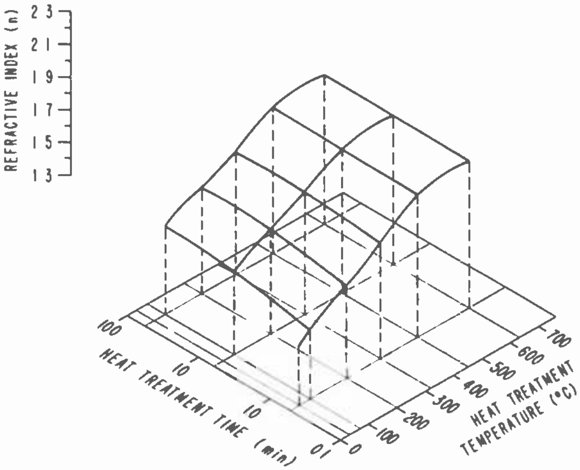

Fig. 16—Same as Fig. 13, but showing effects on refractive index.

Heat treatments in vacuum instead of normal pressure did not increase the refractive index or change the film properties to a measureable extent.

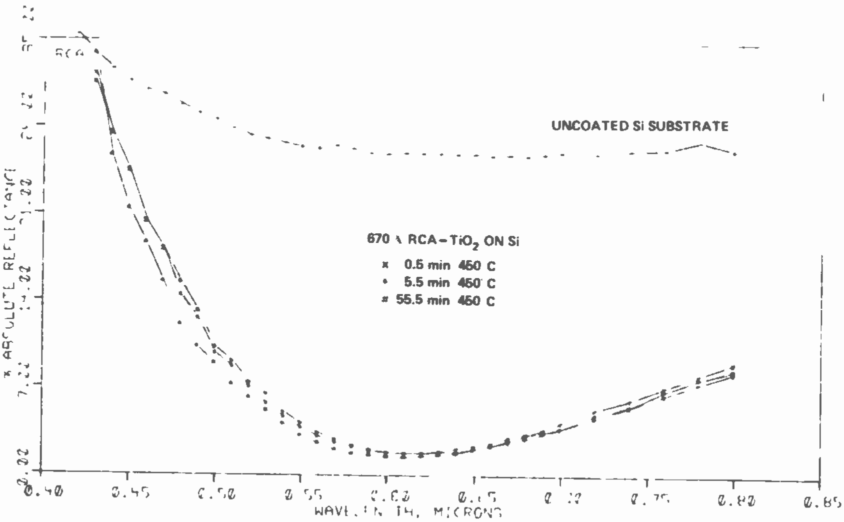

Fig. 17—Absolute reflectance of spray-on TiO$_2$ coatings on silicon as a function of wavelength after a 450°C final heat treatment for various durations. Note that the AR coating is essentially cured after only 30 sec at 450°C.

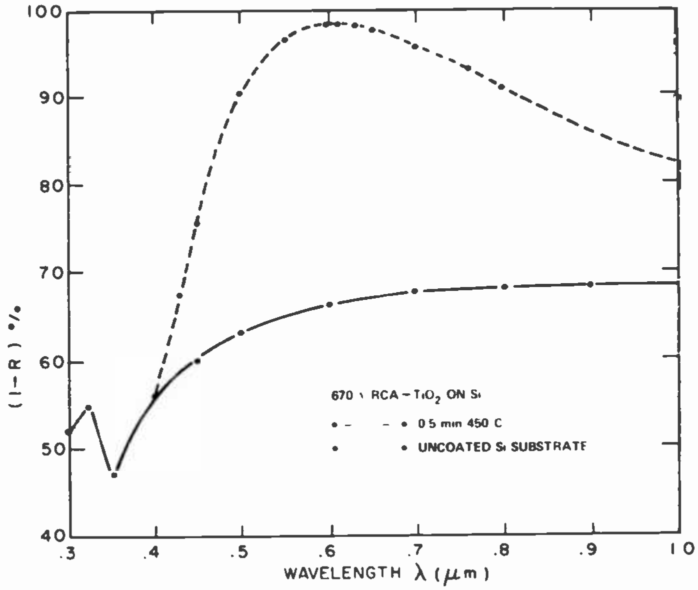

Fig. 18—Reflection spectra in terms of (1-*R*)% vs. wavelength for the silicon substrate and for a 670-Å thick TiO_2 film on silicon heated for 30 sec at 450°C.

3.3.4 Reflectance, Transmittance, and Absorbance

A computer print-out plot showing absolute reflectance as a function of wavelength of a 670-Å thick TiO_2 spray-coating on polished silicon slices is presented in Fig. 17. A broad reflectance minimum of 1.3% occurs in the desired wavelength range of 0.60 to 0.62 μm. The effects of final heat treatments at 450°C for 0.50, 5.5, and 55.5 min shows negligible reflectance differences in the region of the minimum, indicating that the coating is essentially fully cured after a final heat treatment of only 30 sec at 450°C. A comparative curve for the uncoated polished silicon substrate shows an absolute reflectance of 26 to 27 % in the wavelength range of 0.55 to 0.75 μm. Reflection spectra in terms of (1-R)% versus wavelength for the TiO_2 film heated for 30 sec at 450°C, and for the uncoated silicon substrate, are presented in Fig. 18.

On glass substrates ($n \sim 1.5$) the same TiO_2 films increase the reflectance substantially, as expected (see Fig. 19).

Transmittance curves for the identically-treated coatings on fused silica substrates are presented in Fig. 20. The data indicate that there is no significant absorption down to a wavelength of 0.35 μm.

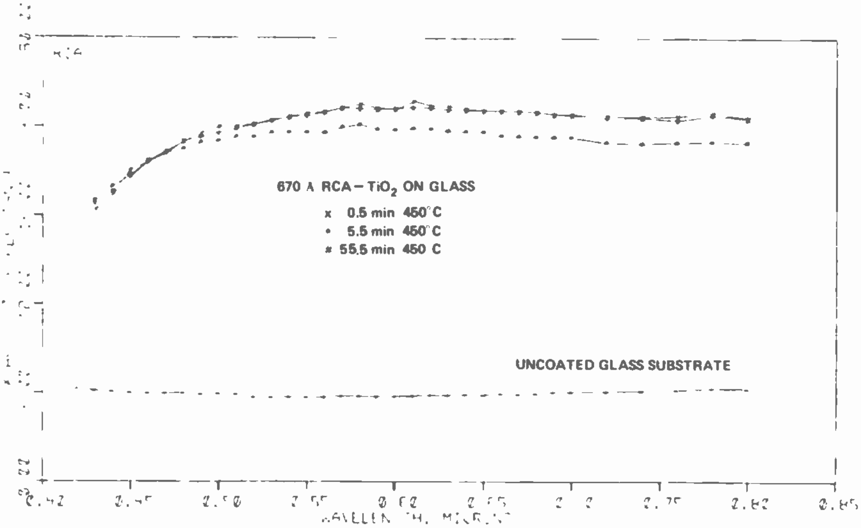

Fig. 19—Absolute reflectance of the TiO_2 films defined in Fig. 17, but on glass substrate, indicating a substantial increase in reflectance compared to that of the uncoated control.

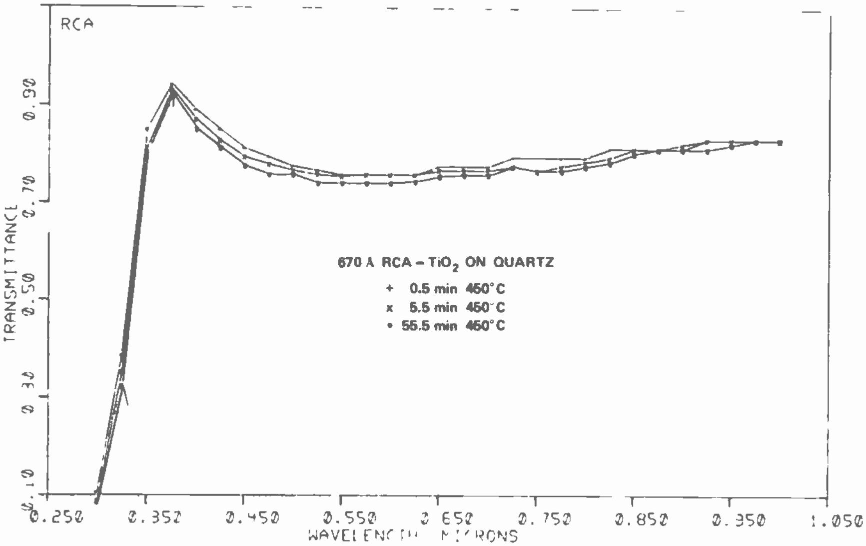

Fig. 20—Transmittance as a function of wavelength for TiO_2 films treated as defined in Fig. 17. Measurements were made with reference beam passing through air.

3.3.5 Structure

The structure of TiO_2 films was examined by x-ray diffractometry. Films of several thousand angstroms were deposited on fused silica substrates followed by our conventional heat treatment sequence. No crystalline diffraction was recorded on samples heated after the final step at 450°C for 30 sec, indicating an amorphous structure. However, in another test, samples heated for 55 min exhibited the presence of a crystalline phase which was indentified as anatase, the tetragonal form of TiO_2.

Infrared absorption spectroscopy (transmission mode) of 6000-Å thick films on silicon showed no specific absorbance maxima in the wave number range of 670 to 2700 cm^{-1} after each of the three heat-treatment steps. A strong absorbance maximum at 3500 cm^{-1} indicated the presence of OH groups. The intensity of this band decreased with progressive heating treatments from 200 to 450°C, revealing the elimination of hydroxy groups with thermal curing of the film.

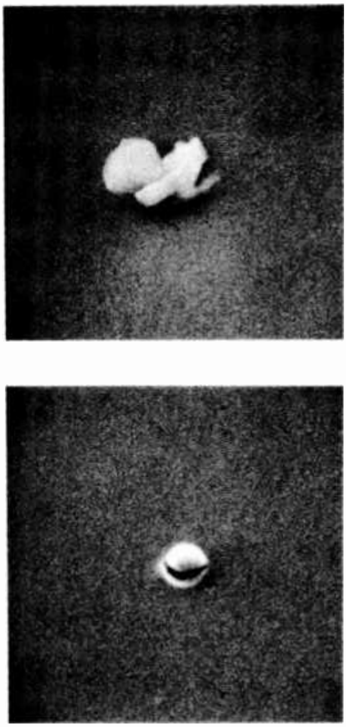

Fig. 21—SEM micrographs showing particulate agglomerates on the surface (A) and in a micropinhole (B) of a sprayed-on TiO_2 film. Vertical measure of top defect is 1.8 μm and of bottom defect is 0.6 μm.

Microscopic inspection of spray-coated TiO_2 films usually shows some defects, such as particulate oxide or hydroxide agglomerates and micropinholes. SEM micrographs of a typical defect of each type are presented in Figs. 21A and B. Electrical measurements of cell efficiency have shown that the presence of such defects does not significantly impair cell performance. Auger electron spectroscopy depth profiles indicated excellent compositional uniformity of the films, regardless of duration of heat treatment at 450°C. Carbon and sulfur were the only impurities detected during this analysis.

A few experiments were carried out to assess the possible merits of laser annealing in addition to, or instead of, the heat treatments of sprayed-on TiO_2 coatings. Silicon test wafers and metallized solar cells were subjected to a frequency-doubled Nd-YAG laser beam (0.53 μm, 5KHz, 100 ns, 100 μm beam diameter) at energy densities ranging from 0.40 to 0.85 J/cm^2. The lower energy did not lead to detectable changes in the films, whereas the higher energy density caused vaporization of the films, leaving a relatively clear substrate surface. No further detailed tests were made since the initial results showed little promise.

3.3.6 Corrosion Resistance

An important requirement of the AR coating is its resistance to corrosion, stress relief, delamination, cracking, or chemical changes over an extended time frame. A simple but rigorous functional test that has shown good correlation with long-term degradation of refractory oxide films in field conditions is the hot water test. In this procedure the sample is immersed in boiling distilled water for 10 to 20 min.[60] Typical samples of TiO_2 spray-on films on polished silicon wafers and on metallized solar cells were boiled for periods of up to 60 min to simulate exceptionally severe conditions. Ellipsometric measurements of film thickness and index of refraction showed no change after these tests. The films remained clear, without cracks or microscopically visible defects, and did not peel or delaminate on Scotch tape testing, indicating excellent stability.

Abrasion resistance of the spray-on TiO_2 films on smooth silicon surfaces is excellent, based on the simple but effective rubber eraser test.

The resistance of the film toward corrosive chemicals was tested by immersing coated silicon wafers and metallized solar cells for one hour at a temperature of 85°C in the following aqueous reagents, all at an absolute concentration of 1 wt%: HCl, HNO_3, H_2SO_4, H_3PO_4, and NH_4OH. No deterioration or visual changes of any sort occurred on the samples during these demanding corrosion tests.

Hardened TiO_2 spray-deposited films on solar cells, when subjected to 1–5 vol % aqueous solutions of concentrated HF, are removed in 2 to 5 min with no resultant degradation of cell electrical parameters. Etching is heterogeneous in the sense that a gradual thinning of the layer is often accompanied by undercutting and flaking. Cells may be stripped and recoated with no further surface preparation other than thorough rinsing and drying to eliminate potentially harmful residual HF and moisture.

Exposure of sprayed and cured TiO_2 films to polyvinylbutyrate plastic at elevated temperature and pressure, as used at RCA in the lamination to glass panels for array assemblies, likewise showed no signs of attack, deterioration, or visual changes.

3.4 Effects on Solar Cell Efficiency

The effects of AR coatings on the electrical performance of solar cells was studied as a function of film thickness for spray solutions prepared from various titanium source materials. These materials included titanium(IV) isopropoxide, titanium(IV) ethoxide, titanium(IV) butoxide, and commercial "Titaniumsilicafilm-C" concentrate. A preliminary test matrix showed that the AR coating obtained from all four sources were of high quality and of similar effectiveness. No advantages were gained by using the butoxide or the more expensive and less stable ethoxide instead of the isopropoxide specified in the RCA-TiO_2 spray mixture. The tests to be described in this section were therefore confined to the RCA-TiO_2 spray mixture and the spray solution prepared with "Titaniumsilica film C."

Throughout the remainder of the paper, AR coatings derived from spray mixtures incorporating the commerical "Titaniumsilicafilm-C" concentrate will be referred to as "SiO_2-TiO_2" for brevity and clarity.

The coating experiments were conducted with two types of solar cells for comparison: (1) RCA cells having screen-printed silver metallization and (2) OCLI cells* having conventional evaporated Ti/Pd/Ag metallization. The conversion efficiency of cells before and after AR coating was determined by the usual I_{sc} and V_{oc} measurements, as described in Sec. 2.5. *I-V* curves for typical cells of each type of metallization are presented in Figs. 22 and 23. The ratio of J_{sc} measured after AR coating over J_{sc} of the bare cell before coating was taken as a convenient approximation of the change in conversion efficiency under standardized irradiation conditions. Polished single-crystal silicon wafers were used as control substrates for the optical measurements.

---

* Manufactured by Optical Coatings Labs., Inc., Santa Clara, CA.

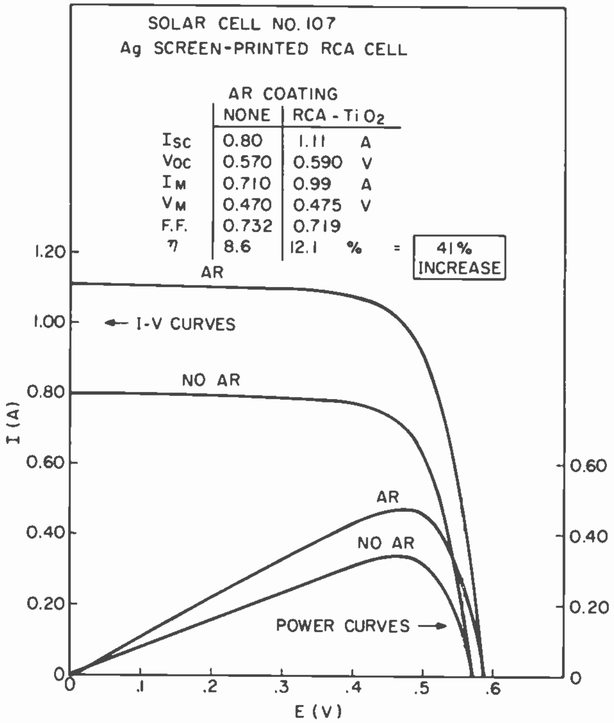

	AR COATING		
	NONE	RCA-TiO$_2$	
I$_{SC}$	0.80	1.11	A
V$_{OC}$	0.570	0.590	V
I$_M$	0.710	0.99	A
V$_M$	0.470	0.475	V
F.F.	0.732	0.719	
η	8.6	12.1	% = 41% INCREASE

Fig. 22—Solar cell *I-V* and power curves before and after RCA-TiO$_2$ AR coating; Ag screen-print metallization.

The results for RCA cells with screen-printed silver metallization, AR-coated with the RCA-TiO$_2$ source solution, are summarized in Table 4. The effect of TiO$_2$ film thickness on the increase in current density ratio Γ (J_{sc} after coating/J_{sc} before coating) is shown graphically in Fig. 24. A broad maximum of $\Gamma = 1.39$ is attained with a film thickness of 700 Å.

Film thickness measurements were done ellipsometrically on the cells as well as on analogously AR-coated polished silicon test wafers. The films on cells gave unreliable thickness readings due to the surface roughness of sawed and chemically etched silicon surfaces. The acurate film thicknesses measured on the smooth test wafers are considered representative and were used for plotting the J_{sc} increase versus thickness graphs. (Stylus profilometric traces of typical RCA cell surfaces showed silicon roughness peaks of 0.4 μm at an average frequency of 9 peaks/mm horizontal distance, rendering step-height measurements of

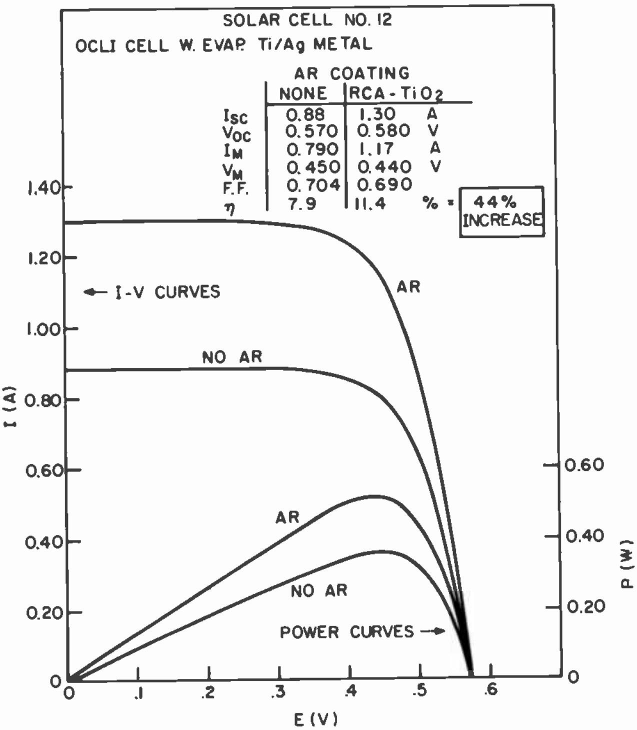

Fig. 23—Solar cell *I-V* and power curves before and after RCA-TiO_2 AR coating; evaporated Ti/Pd/Ag metallization.

Table 4—Increase in Cell Efficiency as a Function of RCA-TiO_2 AR Film Thickness for Cells with Screen-printed Metallization

Solar Cell[a] (No.)	Film Thickness[b] (Å)	Refractive Index[b] (n)	Current Density Increase[c] (Γ)	Conversion Efficiency[d] Before Coating (%)	After Coating (%)
501A-110	903	2.141	1.26	8.7	10.9
501A-109	801	2.150	1.29	8.5	10.8
501A-107	697	2.137	1.39	8.8	12.1
501A-105	639	2.137	1.36	8.5	11.7
501A-86	539	2.182	1.35	8.6	11.6
501A-85	483	2.150	1.36	8.6	11.8

[a] RCA cells (7.5-cm diam.). Screen-printed Ag metallization of 8.0-μm thickness.
[b] Ellipsometric measurement on polished silicon test wafers; Hg light at λ = 5461 Å.
[c] Ratio of J_{sc} after/before coating.
[d] AM-1 simulation ELH lamp at 100 mW/cm^2.

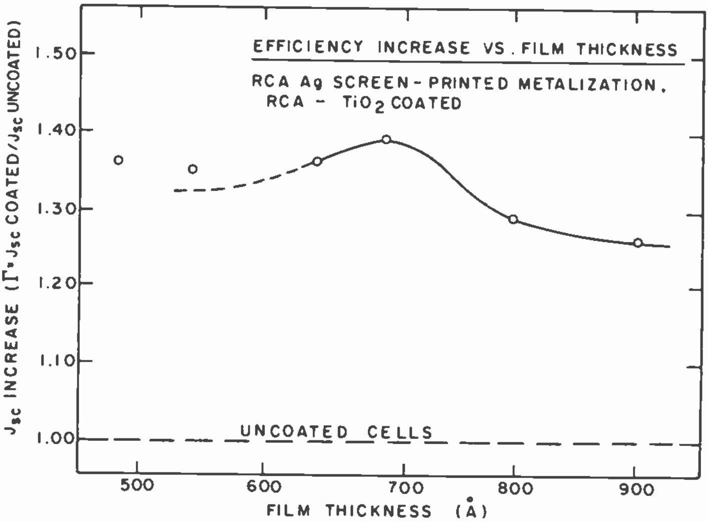

Fig. 24—Electrical performance as a function of AR film thickness. Cells have a 8-μm thick screen-printed Ag metallization grid.

the thin AR film also unreliable.) The ellipsometrically determined index of refraction averaged 2.15 for the test wafers and 2.18 for the cells.

The cell conversion efficiency η averaged 8.6% before and 11.5% after TiO_2 coating. Comparison with a vacuum-evaporated ZrO_2 AR coating of similar film thickness (725 Å) and refractive index ($n = 2.0$) showed improvements of only a few percent in efficiency despite the perfect uniformity of film thickness and absence of any particulate impurities or heat treatments.

The results we obtained for OCLI cells with 2.7-μm-thick vacuum-evaporated Ti/Pd/Ag metallization are presented in Table 5 and in Fig. 25. The effectiveness of the OCLI sputter-deposited SiO_x AR coating was determined by measuring the current density before and after chemical stripping of the coating. As indicated in Fig. 25, the ratio increase (Γ) averaged 1.45 for a nominal ellipsometric film thickness range of 820 to 870 Å. No test wafers with SiO_x were available for comparison. The cell conversion efficiency averaged 7.6% for bare cells and 11.0% for SiO_x coated cells for an optimized film thickness range within 820–870 Å.

Recoating the cells with RCA-TiO_2 led to a peak increase of Γ of at least 1.48, centered between 625 and 675-Å film thickness. Recoating with SiO_2-TiO_2 led to a Γ maximum of 1.42 for a film thickness between 700 and 740 Å. The film thicknesses stated were obtained from ellipso-

Table 5—Increase in Cell Efficiency as a Function of AR Film Thickness for Cells with Evaporated Metallization

Solar Cell[a] (No.)	Film Thickness[b] (Å)	Refractive Index[b] (n)	Current Density Increase[c] (Γ)	Conversion Efficiency[d] Before Coating (%)	Conversion Efficiency[d] After Coating (%)
		Spray-Liquid RCA-TiO_2			
10	895	2.220	1.38	7.6	10.6
11	745	2.204	1.44	7.6	10.8
12	677	2.193	1.48	7.9	11.4
9	605	2.218	1.46	7.4	10.8
7	545	2.187	1.41	7.8	11.1
8	515	2.165	1.40	7.4	10.3
		SiO_2-TiO_2			
1	940	1.973	1.38	7.3	10.2
2	816	1.950	1.39	7.6	10.6
3	745	1.940	1.42	7.4	10.0
4	702	1.929	1.42	7.8	10.9
6	604	1.933	1.39	7.4	9.9
5	572	1.916	1.38	7.6	10.3

[a] OCLI cells (7.5 cm diam.). Vacuum-evaporated Ti/Pd/Ag metallization; cells stripped of their original SiO_x AR coating. Profilometrically measured metal thickness is 2.7 μm.

[b] Ellipsometric measurement on polished silicon test wafer; Hg light at λ = 5461 Å.

[c] Ratio of J_{sc} after/before recoating.

[d] AM-1 simulation ELH lamp at 100 mW/cm^2.

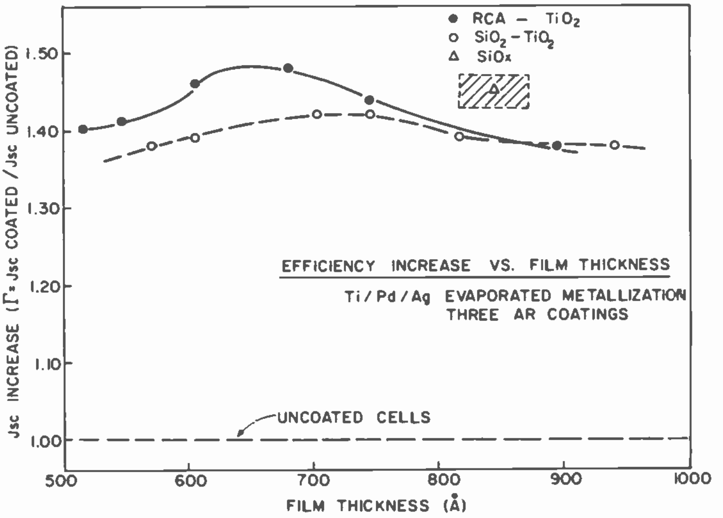

Fig. 25—Electrical performance as a function of AR film thickness. Cells have 2.7-μm thick vacuum-evaporated Ti/Pd/Ag metallization.

metrically measured silicon test wafers. Measurements on cells again deviated, but in the opposite direction than observed for RCA cells; OCLI cells averaged 17% *less* than the test wafers. Stylus profilometry indicated a cell surface roughness of typically 0.6 μm with a frequency averaging 14 peaks/mm horizontal distance.

Ellipsometric measurements of the refractive index of the AR films also gave differences between test wafer substrates and OCLI cells. RCA-TiO_2 averaged an index of 2.20 on test wafers and "2.37" on cells; SiO_2-TiO_2 was 1.94 on test wafers and "2.26" on cells; OCLI SiO_x measured "1.81" on cells, which corresponds to normalized values of 1.55 to 1.69 on test wafers. The OCLI cell conversion efficiency averaged 7.6% without AR coating, 10.8% with RCA-TiO_2, and 11.0% with OCLI-SiO_x. The values for SiO_2-TiO_2 are somewhat lower, averaging 10.3%. Several statements can be made based on these observations:

(1) Comparison of the effectiveness of RCA-TiO_2, SiO_2-TiO_2, and SiO_x AR coatings on commercial thin-film metallized cells showed that TiO_2 from RCA-TiO_2 solution is superior to both SiO_2-TiO_2 and OCLI-SiO_x, as seen from the maximal Γ values, which are 1.48+ at 625 to 675 Å, 1.42 at 700 to 740 Å, and 1.45 at 820 to 870 Å, respectively.

(2) Screen-print metallized RCA cells with RCA-TiO_2 coating exhibited a maximal Γ value of 1.39 at 700 Å. This apparently lower value is due to the higher initial cell conversion efficiency of uncoated RCA cells (8.6%) than that of OCLI cells with coating removed (7.6%). However, the final conversion efficiency after coating increased to 11.5% for RCA cells, but to only 10.8% for OCLI cells.

(3) The conversion efficiency for OCLI cells recoated with RCA-TiO_2 exhibited a maximum efficiency of 11.4% for a film thickness of 700 Å.

(4) Although a greater effectiveness should be expected for a physically vapor-deposited AR coating, the conversion efficiency for OCLI cells with their more expensively produced SiO_x coating averaged 10.9% for the presumably optimal thickness of these films. Reduced scattering losses should result from the more uniform coverage atainable, especially in comparison to the thick-film metallized cells as used in this analytical study.

(5) The results we obtained again emphasize the relative noncriticality of the AR film thickness. For example, the cell efficiency of RCA-TiO_2 recoated OCLI cells, averaged over the entire tested film thickness range from 500 to 900 Å, is a remarkable 10.8% (without indications of drastic decreases beyond this range), as compared to 11.4% for the maximum at about 700 Å.

(6) Ellipsometric measurements of thickness and refractive index of AR coatings on microscopically nonplanar cell surfaces are not reliable due to optical disturbances. Control measurements must therefore be performed on polished silicon test wafers and correlated with cell values, as was done in our present work.

Pilot production spray processing was carried out successfully with over 2000 screen-print metallized solar cells using the RCA-TiO_2 spray mixture and the conditions we have specified. Typical cells had an AR coating thickness of 700 Å and a refractive index of 2.2. The film thickness uniformity within a cell was estimated to be within ±5% over most of the cell surface area. The interference color in white light when viewed perpendicular to the surface was blue-violet and the films were clear and brilliant. Variations in appearance from cell to cell were caused by surface irregularities in the sawed cell surface, but did not materially reduce the cell efficiency. The short-circuit current of all cells, and the electrical conversion efficiency of most cells, were measured before and after AR coating. Increases in cell conversion efficiency were typically 35 to 40%.

3.5 Relationship of AR Coating, Reflectance, and Wavelength

As described in Sec. 1.3, Eqs. [1], [2], and [3] serve as useful guides in determining the refractive index and thickness of an AR coating designed for minimum reflectance over a narrow band of wavelengths. However, with respect to the solar spectrum, whose wavelength distribution for Si photovoltaic applications varies from 0.3 to 1.1 μm, the physical situation for describing the optimum parameters of a QWAR coating becomes substantially more complex. There are at least six factors to consider which vary as a function of wavelength over this spectral region of interest:

(1) Substrate refractive index, n_{Si}

Hulthén[61] determined the refractive index of epitaxial silicon as a function of wavelength using optical transmission and photoconductivity measurements and found excellent agreement with values reported for bulk single-crystal silicon. These data, plotted in Fig. 26, show a strong nonlinear dependence of the refractive index versus wavelength; n_{Si} varies from ~3.5 to ~5.7 for $\lambda = 1.1$ μm to $\lambda = 0.4$ μm, respectively.

(2) Substrate reflection, R_{Si}

Since n_{Si} is a function of λ, then the reflectance from the silicon surface also varies as a function of wavelength according to Eq. [1], necessarily increasing with decreasing values of λ. Reflectance versus wavelength

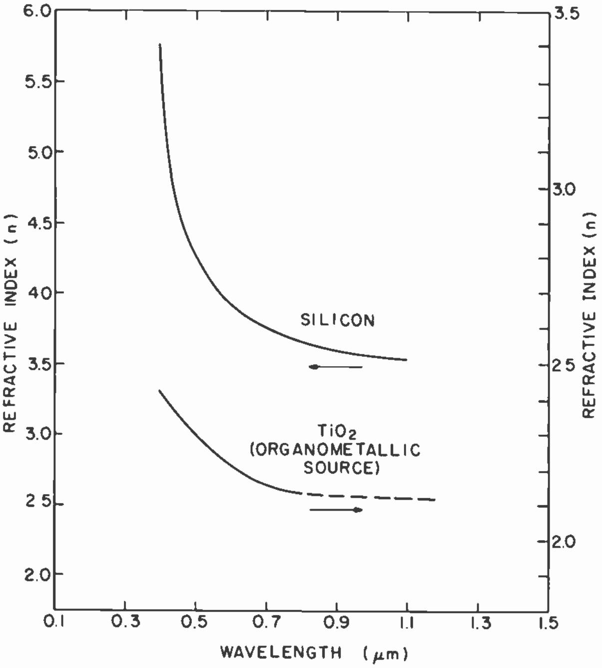

Fig. 26—The refractive index of epitaxial and bulk single-crystal silicon (upper curve) and titanium dioxide (lower curve) increase as a function of decreasing wavelength from $\lambda = 1.1\ \mu m$ to $\lambda = 0.3\ \mu m$.

for a silicon surface in air ($n_2 = 1$) and under cover ($n_2 = 1.5$) is plotted in Fig. 27.

(3) AR coating refractive index, n_{ar}

The refractive index of the AR film itself varies as a function of wavelength. Haigh[28] published relevant data for TiO_2 AR coatings from an organometallic source by ellipsometric techniques and showed n_{ar} to increase with decreasing wavelength as shown in Fig. 26 (dashed extrapolation is ours).

(4) Solar spectral energy, E_s

Solar irradiance for AM = 0 peaks in the blue region of the visible spectrum. The overall energy is reduced at all wavelengths after passing through the earth's atmosphere because of scattering, absorption of the UV by ozone, and absorption of the near IR by water vapor, CO_2, and other gases. The peaks for AM = 1 and AM = 2 shift to longer wavelengths and are much broader, as shown in Fig. 28.[62]

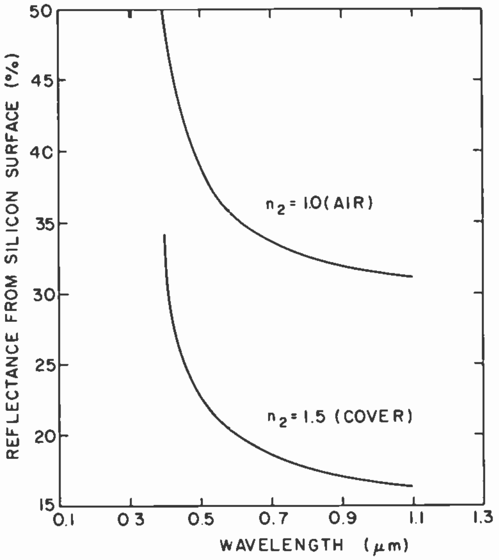

Fig. 27—The reflectance from a silicon surface in air and under cover substantially increases with decreasing wavelength over the range shown.

(5) Spectral response, S.R.

Because of the nonlinear relationship among absorption coefficient, wavelength, and the minimum ionization energy (1.1 eV for Si), the silicon solar cells' ability to collect an electron–hole pair is also a function of wavelength, and generally exhibits a broad maximum near $\lambda \sim 0.7$ μm. Infrared photons having a wavelength longer than 1.1 μm cannot release an electron–hole pair, and photons in the visible and ultraviolet parts of the spectrum have excess energy which merely generates heat resulting in a reduction of energy efficiency but not quantum efficiency. Also, wavelength determines the depth at which electron–hole pairs are generated within the cell, which in turn influences the collection efficiency. The spectral response of cells with an arsenic-diffused junction used in our investigation is presented in terms of relative quantum efficiency in Fig. 29.[63]

(6) AR coating reflection, R_{QWAR}

Application of a quarter-wave AR coating to the silicon surface produces a minimum reflectance for a narrow band of wavelengths with increasing reflectance at either side. Fig. 17 depicts absolute reflectance versus wavelength for our spray-on TiO_2 coatings.

This complex physical situation is described graphically in Fig. 30. With respect to determining the optimum parameters of an AR coating

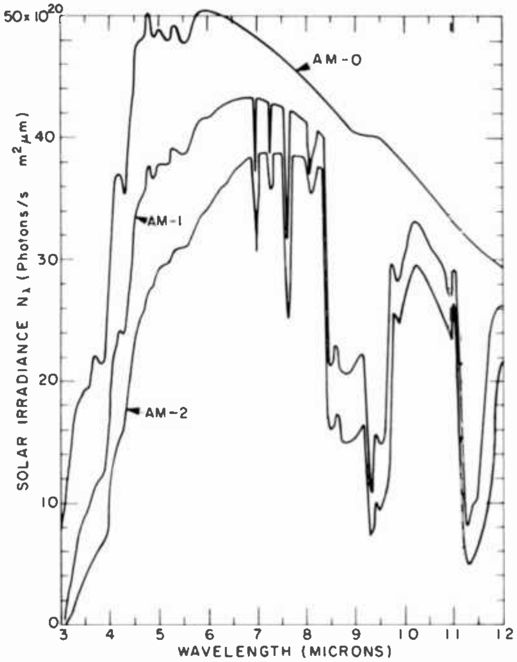

Fig. 28—Solar irradiance in terms of photon flux. Peaks for AM = 1 and AM = 2 are broader and shift to longer wavelengths.

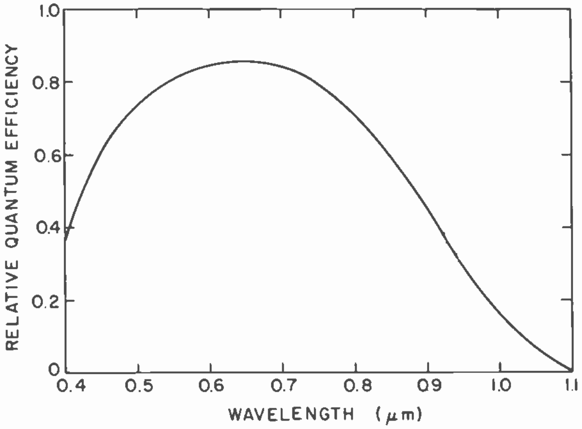

Fig. 29—The Spectral response in terms of relative quantum efficiency for an arsenic-diffused Si junction

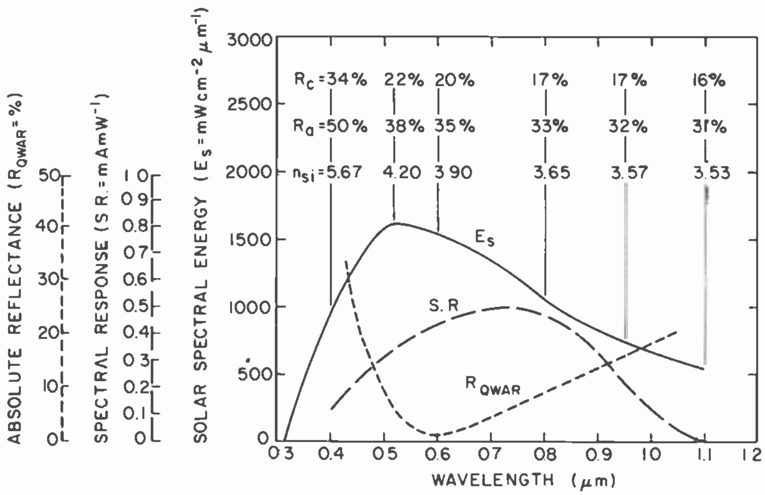

Fig. 30—Graphical analysis of n_{si}, R_{si}, E_s, S.R, and R_{QWAR} as a function of wavelength for determining the optimum parameters of an AR coating over the wavelength range $\lambda = 0.3$ to 1.1 μm. Simultaneous evaluation of these curves and the associated data indicated is necessary for determination of T_f at any particular wavelength.

on silicon, superimposed curves and associated data of these factors are plotted as a function of wavelength. The solar spectral energy values (E_s, in terms of mW cm^{-2} μm^{-1}) were obtained from the Energy Technology Handbook[64]; absorption minima have been omitted to avoid congestion. To permit comparison, the spectral response (S.R.) in terms of relative quantum efficiency of the silicon cell in Fig. 29 was recalculated in terms of mA mW^{-1}. The reflectance curve (R_{QWAR}) was determined from an experimentally optimized QWAR coating of spray-on TiO_2 of $T_f = 680$ Å and $n_{ar} = 2.2$ as determined in 6328-Å light. Above these curves of E_s, S.R. and R_{QWAR} versus wavelength, values of the refractive index of silicon (n_{si}), the reflectance (R_a) of the silicon in air, and the reflectance (R_c) of the silicon under cover ($n_2 = 1.5$) have been tabulated at different intervals along the solar spectrum.

Examination of these data in Fig. 30 will give some indication as to the degree of difficulty in determining the optimal thickness and refractive index of a QWAR coating, but some interesting conclusions can be drawn. A considerable number of high-energy photons near $\lambda = 0.45$ μm are lost due to the high reflectance (~45% in air and ~30% under cover) and the low spectral response (~0.2 mA mW^{-1}) of silicon. This loss is further compounded by a high absolute reflectance (~23%) of the QWAR coating. Basically the same argument exists at lower energies near $\lambda = 0.9$ μm, but to a lesser extent. A dual antireflection coating could extend the minimum reflectance of the QWAR coating out to higher energies, but the low spectral response coupled with the necessity of an inordinately high refractive index ($n \sim 2.8$ at $\lambda_{\min} = 6000$ Å) of the layer adjacent to Si, not to mention the added processing cost, makes this procedure questionable. An extensive theoretical treatment of AR coatings on solar cells by Gandham, et al.[50] corroborates our conclusions, which are based on experimental results. (High-efficiency concentrator-type cells are an exception; they do require a multilayer AR coating for maximum effectiveness.[65])

The ideal refractive index of an AR coating to achieve maximum effectiveness across the solar spectrum is a strong function of wavelength (similar to that of silicon in Fig. 26) and follows the relationship in Eq. [2]. Fig. 31 shows the ideal values of refractive index versus wavelength for optimum QWAR coatings on silicon in air and under cover. Assuming that silicon cells will be protected with a plate of silicate glass ($n_2 = 1.5$), in actual use, the highest possible value of n_{ar} should be attained. At $\lambda = 0.6\ \mu$m, for which most coatings are tuned to obtain minimum reflectance (R_{min}) from the silicon surface, the index requirement from Fig. 31 is $n_{ar} \sim 2.4$. Unfortunately no readily depositable films possess such a high refractive index with good transmission.

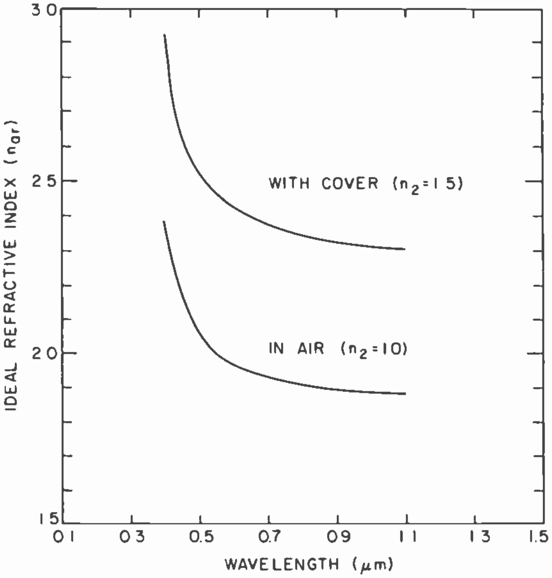

Fig. 31—Ideal values of the refractive index versus wavelength for optimum QWAR coatings in air and under cover as computed from refractive index values of silicon in Fig. 11.

The optimum thickness (T_f) for a QWAR coating on a silicon solar cell requires the simultaneous evaluation of the several previously mentioned parameters, graphically illustrated in Fig. 30. Assuming n_{ar} to be fixed for a particular coating material, any attempt to predict the thickness for maximum broadband antireflection must include an analysis of n_{Si}, R_{Si}, E_s, S.R., and R_{QWAR} as a function of wavelength. We believe the best and simplest way to obtain the optimum thickness value is experimentally, as shown in the examples in Figs. 24 and 25.

The tolerances for attaining the optimum thickness are relatively wide. For example, across the 400-Å spread of AR coating thicknesses in Fig. 24, the maximum J_{sc} at $T_f \sim 590$ Å represents only a 4 to 9% increase from those of 500 Å and 900 Å, respectively. Shah and Fuller[29] presented similar curves for arsenic-doped oxide AR coatings ($n_{ar} \sim 1.5$) on both P- and As-diffused silicon cells which have shown even less sensitivity of the J_{sc} to thickness variations. Cells with large off-optimum thicknesses (~15%) of spray-on TiO_2 can still function adequately with only a 3 to 5% decrease in J_{sc}, which represents a minor decrease (~0.5%) in the overall efficiency (η) of the cell, since most of the J_{sc} is already present before AR coating. The main point to be noted is that the ±15% off-optimum AR coated cell still produces ~95% of the electrical energy which it is capable of producing with an optimum thickness.

The wide tolerance in the AR coating thickness explains why defects normally encountered in the spray process, such as particulates and localized thickness irregularities (especially along the thick, screen-printed metallization), are not a problem. These defects are essentially cosmetic in nature and have a minimal effect on the overall efficiency of the cell. The small increase in total efficiency obtainable by AR coatings from expensive vacuum techniques is more than offset by the low-cost, high-speed spray technique which is compatible with a high degree of automation for mass production.[66]

4. Conclusions

(1) A high-speed mass production process has been developed and optimized for depositing, at low cost, a single-layer, thin-film antireflection coating on metal-patterned single-crystal silicon solar cells for terrestial applications. The process has been applied successfully to cells with either evaporated Ti/Pd/Ag metallization on a polished silicon surface or screen-printed silver metallization on a saw cut and etched silicon cell surface.

(2) Several materials and deposition methods have been examined for producing the AR coating. The film material selected was titanium

dioxide. We have prepared this compound by automated atomization spraying of titanium(IV) isopropoxide in a liquid organic solution. After drying, the film is reacted in air by a series of heat treatments to form TiO_2.

(3) Several organotitanium compounds were tested as sources for preparing the spray mixture, including titanium(IV) isopropoxide, titanium(IV) ethoxide, and titanium(V) butoxide. The commercial "Titaniumsilicafilm C" concentrate was also tested for preparing the spray solution, but was expensive and did not lead to superior cell performance. Titanium(IV) isopropoxide was found to be the preferred material, from both technical and economic considerations.

(4) The composition of the spray solution was devised and optimized to yield a uniform film of accurately controllable properties. Vapor pressure, viscosity, miscibility, chemical reactivity, and surface tension of the solution components were among the critical characteristics of the mixture components. In addition to the titanium(IV) isopropoxide as the essential reactant, *n*-butyl acetate is used as the diluent solvent to form a single-phase solution. A low-molecular weight aliphatic alochol, preferably sec-butanol, serves as a leveling agent to spread the solution uniformly between the metallization grids. A key component for rendering the solution successfully sprayable by optimizing critical physical and chemical mixture parameters is 2-ethyl-1-hexanol; it allows the attainment of a continuous and uniform liquid film.

(5) Atomization spraying of the organotitanium spray solution uses commercial automated equipment of refined design, having the capability of controlling the deposition parameters precisely. Spraying is conducted in air of controlled purity and at low relative humidity level to avoid premature reaction in the gas phase. Three machine parameters were selected from about 15 to vary and control the film thickness: (1) source solution delivery pressure, (2) atomization spray pressure, and (3) gun-to-substrate distance.

(6) A series of brief post-deposition heat treatments in room air are applied at 70°C, 200°C, and 450°C, respectively, to form the final TiO_2 AR coating. The cured films consisted essentially of amorphous TiO_2, had a refractive index in the range of 2.1 to 2.2, and were readily removable with hydrofluoric acid. A 670Å thick film on a polished silicon substrate exhibited a reflection minimum of 1.3% (absolute) at a wavelength of 0.60 μm. Films on plates of fused quartz showed no significant light absorption down to a wavelength of 0.35 μm.

(7) The uniformity of film thickness on metallized and spray-coated solar cells was better than ±5% over the major portion of the cell surface. We demonstrated that the TiO_2 film thickness in the range of 600 to 750Å is non-critical in terms of cell efficiencies.

(8) The TiO_2 AR coating adheres well and is extremely stable and corrosion resistant, as demonstrated by exposure of coated cells to boiling water and to hot diluted acids and ammonia.

(9) Application of the process to the coating of over 2000 single-crystal 7.5 cm-diameter solar cells with either screen-printed silver metallization or with vacuum-evaporated Pd/Ti/Ag metallization showed increases of over 40% in the electrical conversion efficiency.

(10) Based on an annual production rate of 55 million cells capable of yielding 30 million watts electrical power, the cost for producing the antireflection coating by this process is at present only one cent per cell, or less than 2 cents per watt. This amount is less than one-eighth of that for conventional vacuum sputtering. The outstanding advantage of the spray deposition process is its ideal suitability for continuous automated mass production of solar cells. The process has been evaluated and verified for application by Jet Propulsion Laboratory.

(11) Finally, the optics underlying AR coatings have been reviewed and consideration for optimizing AR coatings for photovoltaic cells have been discussed. It was shown that the thickness of the film is relatively noncritical over a considerable range, which agrees with our experimental results. In addition, a comprehensive literature search covering over 50 references on the subject of AR coating for solar cells has been presented.

Acknowledgments

We wish to thank W. Kurylo for his contribution to the spray coating and processing of over 2000 solar cells, R. V. D'Aiello for testing and evaluating coated cells, G. E. Nostrand for electrical characterization measurements, J. C. Toner for computer programming comparative cost analyses, and P. J. Zanzucchi for optical measurements. We also acknowledge the guidance we received from C. Brell of Zicon Corporation in regard to spray machine parameters. Thanks also to G. L. Schnable, A. H. Firester, J. P. Wittke, and R. V. D'Aiello for critically reviewing the manuscript.

References:

[1] G. Cheek, A. Genis, J. B. DuBow, and V. R. Pai Verneker, "Antireflection Properties of Indium Tin Oxide (ITO) on Silicon For Photovoltaic Applications," *Appl. Phys. Lett.*, **35**, p. 495, Oct. 1979.

[2] B. E. Yoldas and T. W. O'Keeffe, "Antireflective Coatings Applied From Metal—Organic Derived Liquid Precursors," *Applied Optics*, **18**, p. 3133, Sept. 1979.

[3] T. Feng, A. K. Ghosh, and C. Fishman, "Spray-Deposited High-Efficiency SnO_2/n-Si Solar Cells," *Appl. Phys. Lett.*, **35**, p, 266, Aug. 1979.

[4] R. B. Godfrey and M. A. Green, "655 mV Open-Circuit Voltage, 17.6% Efficient Silicon MIS Solar Cells," *Appl. Phys. Lett.*, **34**, p. 790, June 1979.

[5] W. A. Anderson and J. K. Kim, "Reliability Studies on MIS Solar Cells," *Appl. Phys.*, **17**, p. 401, Dec. 1978.

[6] J. Michel, E. Fabre, M. Mautref, and P. Mas, "Reflectivity Analysis on Silicon Solar Cells," 13th IEEE Photovoltaic Specialists Conference, p. 1244, Washington DC, June 1978.

[7] T. L. Chu, S. S. Chu, E. D. Stokes, C. L. Lin, and R. Abderrassoul, "Thin Film Polycrystalline Solar Cells," Ibid., p. 1106.

[8] Y. C. M. Yeh, F. P. Ernest, and R. J. Stim, "Progress Towards High Efficiency Polycrystalline Thin-Film GaAs AMOS Solar Cells," Ibid. p. 966.

[9] S. S. Chu, T. L. Chu, and H. T. Yang, "Large Area Thin Film Gallium Arsenide Solar Cells," Ibid., p. 956.

[10] J. C. C. Fan and C. O. Bozler, "High Efficiency GaAs Shallow-Homojunction Solar Cells," Ibid. p. 953.

[11] A. Meullenberg, Jr., "Space Environment Damage to Solar Cell Coverslide Assemblies," Ibid. p. 107.

[12] E. Bucher, "Solar Cell Materials and Their Basic Parameters," *Appl. Phys.*, **17**, p. 1, 1978.

[13] H J. Hovel, "TiO_2 Antireflection Coatings by a Low Temperature Spray Process," *J. Electrochem. Soc.*, **125**, p. 983, July 1978.

[14] S. S. Chu, T. L. Chu, and H. T. Yang, "Thin-Film Gallium Arsenide Solar Cells on Tungsten/Graphite Substrates," *Appl. Phys. Lett.*, **32**, p. 557, May 1978.

[15] D. H. Olson, "Silicon Monoxide Antireflection Coatings for InP/CdS Solar Cells," *J. Va. Sci. Technol.*, **15**, p. 130, Jan.–Feb. 1978.

[16] P. Van Halen, R. Mertens, R. Van Overstraeten, R. E. Thomas, and J. Van Meerbergen, "Improvement of the Efficiency of Silicon MIS-Inversion Layer Solar Cells," *Proc. International Conf. on Photovoltaic Solar Energy*, p. 280, Luxemburg, Sept. 1977.

[17] J. F. Gibbons and F. C. Wu, "Fabrication and Measurement of Silicon Concentrator Solar Cells," Ibid., p. 242.

[18] W. G. Townsend and D. R. Lillington, "Progress on Aluminum P-Type Silicon SBSCS," Ibid., p. 207.

[19] G. A. Swartz, L. S. Napoli, and N. Klein, "Silicon Solar Cells for Use at High Solar Concentration," *IEEE International Electron Devices Meeting*, p. 226, Wash. DC, Dec. 1977.

[20] R. J. Stim, Y. C. M. Yeh, E. Y. Wang, F. P. Ernest, and C. J. Wu, "Recent Improvements in AMOS Solar Cells," Ibid. p. 48.

[21] P. A. Iles, "Antireflection Coatings for Solar Cells," *J. Vac. Sci. Technol.*, **14**, p. 1100, 1977.

[22] K. W. Mitchell, A. L. Fahrenbruch, and R. H. Bube, "Evaluation of the CdS/CdTe Heterojunction Solar Cell," *J. Appl. Phys.*, **48**, p. 4365, 1977.

[23] S. Franz, G. Kent, and R. L. Anderson, "Heterojunction Solar Cells of SnO_2/Si," *J. Electron Mater.* **6**, p. 107, 1977.

[24] H. Matsunami, S. Matsumoto, and T. Tanaka, "MIS Solar Cells with In_2O_3 Antireflective Coating," *Jpn. J. Appl. Phys.*, **16**, p. 149, Aug. 1977.

[25] H. W. Brandhorst, Jr., "Status of Silicon Solar Cell Technology," *Jpn. J. Appl. Phys.*, **16**, Suppl. 1, p. 399, 1977.

[26] K. S. Sree Harsha, K. J. Bachman, P. H. Schmidt, E. G. Spencer, and F. A. Thiel, "n-Indium Tin Oxide/p-Indium Phosphide Solar Cells," *Appl. Phys. Lett.*, **30**, p. 645, June 1977.

[27] D. E. Carlson, C. R. Wronski, A. R. Triano, and R. E. Daniel, "Solar Cells Using Schottky Barriers on Amorphous Silicon," *12th IEEE Photovoltaic Specialists Conf.*, p. 893, Baton Rouge, LA, Nov. 1976.

[28] A. D. Haigh, "Fired Through Printed Contacts on Antireflection Coated Silicon Terrestial Solar Cells," Ibid. p. 360.

[29] P. Shah and C. R. Fuller, "High Performance, Inexpensive Solar Cell Process Capable of a High Degree of Automation," Ibid. p. 286.

[30] M. G. Coleman, W. L. Bailey, and R. A. Pryor, "Processing Ramifications of Textured Surfaces," Ibid. p. 313.

[31] W. A. Anderson, S. M. Vernon, A. E. Delahoy, J. K. Kim, and P. Mathe, "Factors Which Maximize the Efficiency of Cr-p-Si Schottky (MIS) Solar Cells," *J. Electrochem. Soc.*, **123**, p. 1514, Oct. 1976.

[32] Y. C. M. Yeh, F. P. Ernest, and R. J. Stim, "Practical Antireflection Coatings for Metal-Semiconductor Solar Cells," *J. Appl. Phys.*, **47**, p. 4107, Sept. 1976.

[33] A. G. Revesz, J. F. Allison, and J. H. Reynolds, "Tantalum Oxide and Niobium Oxide Antireflection Films in Silicon Solar Cells," *Comsat Tech. Rev.*, **6**, p. 57, 1976.

[34] A. G. Revesz, J. H. Reynolds, and J. F. Allison, "Optical Properties of Tantalum Oxide Films on Silicon," *J. Electrochem. Soc.*, **123**, p. 889, July 1976.

[35] H. W. Brandhorst, Jr., "Current Status of Silicon Solar Cell Technology," *International Electron Devices Meeting* (*Technical Digest*), p. 331, Wash., Dec. 1975.

[36] J. F. Allison, R. A. Arndt, and A. Meulenberg, "A Comparison of the COMSAT Violet and Non-reflective Cells," *10th Intersociety Energy Conversion Engineering Conf.*, p. 1038, Newark, Delaware, Aug. 1975.

[37] Y. M. Yeh and R. J. Stirn, "Improved Schottky Barrier Solar Cells," *11th IEEE Photovoltaic Specialists Conf.*, p. 391, Scottsdale, Arizona, May 1975.

[38] E. L. Ralph, "Recent Advances in Low Cost Solar Cell Processing," Ibid. p 315.

[39] A. Meulenberg, J. F. Allison, R. A. Arndt, and J. G. Haynos, "Radiation Damage to the COMSAT Non-Reflective Cell," Ibid., p. 204.

[40] G. S. Goodelle, G. R. Brooks, and J. R. Mosher, "High Vacuum U. V. Test of Improved Efficiency Solar Cells," Ibid., p. 184.

[41] T. Matsushita and T. Mamine, "A New Class of Solar Cell with Multi-Layer Structure," *International Electron Devices Meeting* (*Technical Digest*) p. 353, Wash. DC, Dec. 1975.

[42] Y. C. M. Yeh and R. J. Stirn, "Practical Anti-Reflection Coating for Metal Semiconductor Solar Cells," *Proc. Society of Photo-Optical Instrumentation Engineers*, **68**, Optics in Solar Energy Utilization, p. 172, 1975.

[43] A. G. Revesz, "Vitreous Oxide Antireflection Films in High Efficiency Solar Cells," *10th IEEE Photovoltaic Specialists Conf.*, p. 180, Paolo Alto, CA, Nov. 1973.

[44] E. Y. Wang, F. T. S. Yu, V. L. Simms, H. W. Brandhorst, Jr., and J. D. Broder, "Optimum Design of Antireflection Coating for Silicon Solar Cells," Ibid., p. 168.

[45] W. A. Anderson, A. E. Delahoy, and R. A. Milano, "An 8% Efficient Layered Schottky Barrier Solar Cell," Ibid., p. 168.

[46] W. A. Anderson and A. E. Delahoy, "Advances in Schottky Barrier Solar Cell Technology," *8th Intersociety Energy Conversion Engineering Conf. Proc.*, p. 326, Philadelphia, PA, Aug. 1973.

[47] V. Magee, H. G. Webb, A. D. Haigh, and R. Freestone, "Design and Practical Aspects of Maximum Efficiency Silicon Solar Cells for Satellite Applications," *9th IEEE Photovoltaic Specialists Conf.*, p. 6, Silver Springs, MD, May 1972.

[48] P. M. Stella and H. Somberg, "Integrally Covered Silicon Solar Cells," Ibid., p. 179.

[49] I. Chambouleyron and E. Saucedo, "Properties of Chemically Sprayed SnO_2 Antireflecting Films on Si Solar Cells," *Solar Energy Materials*, **1**, p. 299, 1979.

[50] B. Gandham, R. Hill, H. A. Macleod, and M. Bowden, "Antireflection Coatings on Solar Cells, ' *Solar Cells*, **1**, p. 3, Nov. 1979.

[51] H. Terui and M. Kobayashi, "Refractive-Index-Adjustable SiO_2-Ta_2O_5 Films for Integrated Optical Circuits," *Appl. Phys. Lett.*, **32**, (10), p. 666, May 1978.

[52] M. S. Bae and R. V. D'Aiello, "P^+/N High Efficiency Silicon Solar Cells," *Appl. Phys. Lett.*. **31** (4), p. 285, Aug. 1977.

[53] R. A. Arndt, J. F. Allison, J. G. Haynos, and A. Meulenberg, Jr., "Optical Properties of the COMSAT Non-Reflective Cell," *11th IEEE Photovoltaic Spec. Conf.*, p. 40, 1975.

[54] L. H. Hall, "Preparation and Properties of Antireflection Coatings by Chemical Vapor Deposition," *J. Appl. Phys.*, **43** (11), p. 4615, Nov. 1972.

[55] I. Mellan, *Industrial Solvents Handbook*, Sec. Ed., Noyes Data Corp., Park Ridge, NJ. 1977, p. 232 (cited from Union Carbide Corporation).

[56] See Ref. [55], p. 236 (cited from Shell Chemical Co.).

[57] H. Schroeder, "Oxide Layers Deposited from Organic Solutions," *Phys. of Thin Films*, **5**, p. 87, G. Hass and R. E. Thun, Eds., Academic Press, New York, 1969.

[58] B. E. Yoldas, "Preparation of Glasses and Ceramics from Metal-Organic Compounds," *J. Mater. Sci.*, **12**, p. 1203, 1977.

[59] B. E. Yoldas, "Monolythic Glass Formation by Chemical Polymerization," *J. Mater. Sci.*, **14**, p 1843, 1979.

[60] S. H. Leece, "Function Stress Testing in Large-Scale Optical Multifilm Manufacturing," *J. Vac. Sci. Technol.*, **16** (2), p. 356, March/April 1979.

[61] R. Hulthén, "Optical Constants by Epitaxial Silicon in the Region 1-3.3 eV," *Physica Scripta*, **12**, p. 342, 1975.

[62] B. F. Williams, *Automated Array Assembly*, Quarterly Report No. 3, ERDA/JPL Contract No. 954352-76/3, p. 7, Sept. 1976.

[63] R. V. D'Aiello, *Automated Array Assembly, Phase II*, Quarterly Report No. 3, DOE/JPL Contract No. 954868-78/3, p. 11, June 1978.

[64] H. Oman and J. W. Gelzer, in *Energy Technology Handbook*, Douglas M. Considine, Editor-in-Chief, Chapt. 6, p. 60, McGraw-Hill, Inc., New York (1977).

[65] L. S. Napoli, G. A. Swartz, S. G. Liu, N. Klein, D. Fairbanks, and D. Tamutus, "High Level Concentration of Sunlight on Silicon Solar Cells," *RCA Review*, **38**, p. 76, March 1977.

[66] W. Kern and C. E. Tracy, "Abstract: Spray-on Antireflection Coatings for Silicon Solar Cells," *J. Vac. Sci. Technol.*, **17**, p. 374, Jan./Feb. 1980.

The Measurement of Deep Centers in Float Zone Silicon by Photovoltage Spectroscopy

L. L. Jastrzebski

RCA Laboratories, Princeton, NJ 08540

J. Lagowski

Massachusetts Institute of Technology, Department of Material Science, Room 13-4130, Cambridge, MA 02139

Abstract—Derivative (wavelength modulated) photovoltage spectroscopy of MOS and MS structures has been employed for studying band structure transitions and photoionization of deep levels in float zone silicon ($p = 2 \times 10^{15}$ cm^{-3}). From low temperature ($T < 30°$K) photovoltage spectra and photovoltage transient characteristics, it has been established that deep levels of the energy 0.56 eV above the valence band are present in as-grown high quality float zone silicon and in oxidized wafers. The photovoltage measurements also revealed the presence of shallow minority carrier traps in the vicinity of the conduction band edge which is consistent with a noticeable degree of compensation present in the silicon wafers.

1. Introduction

Electrical measurements in semiconductors provide rather limited information about the origin of deep centers. Nevertheless, they have proven extremely useful in "labeling" deep levels with respect to the activation energy and the capture cross-section. Such labeling can in turn be used as a basis for establishing the source of process-introduced defects,[1] decoration mechanism of the crystallographic defects,[2,3] and the effects of defects in the as-grown material on the device performance.[3,4]

A significant practical advancement in characterization of deep levels has been brought about by the development of the Deep Level Transient Spectroscopy (DLTS).[5] DLTS relies on the analysis of the thermal emission of carriers trapped by deep levels and it provides highly sensitive means for labeling trapping centers with respect to their thermal activation energy. This technique was successfully used to characterize deep levels introduced to silicon, GaAs, and other semiconductors by radiation damage,[6] heavy metals,[7] and other impurities.[7,8] However, it should be noted that the thermal activation energy measured by DLTS provides sufficient description of the energy level only for the simple trapping centers as defined within Shockley–Read recombination model. In general, the ionization of defect centers may involve absorption (emission) of phonons, lattice relaxation, excited states and/or configurational changes which can be disclosed more easily by optical studies (due to strict momentum and energy conservation rules) than thermal emission.

The photoionization of deep levels has been utilized in conjunction with photocurrent, photocapacitance, or photovoltage measurements, often, however, with much less success than thermal emission DLTS measurements due to ambiguities in determination of photoionization cross-section.

Recently a simple approach has been proposed for the determination of deep-level photoionization characteristics from derivative wavelength modulated photovoltage[9] and/or photocapacitance spectra.[10] The wavelength modulation utilized in these derivative measurements converts broad photoionization spectra of deep levels into a well-defined peak structure providing a reliable and practical means for labeling of deep levels in the photon energy scale. The advantages of the derivative photovoltage[9,11] or photocapacitance measurements[10] have been demonstrated through the band-structure and deep-level studies in GaAs.

In the present study, Derivative Surface Photovoltage Spectroscopy (DSPS) has been applied for the measurement of deep-level and band-structure transitions in high quality float-zone p-type silicon which is utilized for solid state imagers.[12]

The photovoltage measurements showed the presence of the same deep levels in the as-grown and oxidized material, and a procedure to determine their parameters was developed. In addition to the deep centers, the DSPS method also provided information about presence of shallow centers and degree of compensation in the high quality float zone silicon.

2. Derivative Surface Photovoltage Spectroscopy

The surface photovoltage is defined as the change of the surface potential barrier under illumination. There are two mechanisms leading to the occurrence of the surface photovoltage: (a) the band-to-band excitation of excess carriers and (b) the photoionization of localized levels. The photovoltage generated in a depletion–space-charge region of p-type semiconductor is illustrated in Fig. 1. In both instances (i.e., subbandgap and intrinsic excitation) the photovoltage occurs due to the separation of electrons and holes in an electric field within the space-charge region. In case (b) only the photogenerated holes move in an electric field. The electrons remain localized in deep levels.

Accordingly, the surface photovoltage can in principle be utilized to determine the band-structure transitions and the transitions involving localized levels. The inherently low sensitivity in all standard photovoltage configuration has limited such studies to high-energy-gap semiconductors. Significant extension of the applicability of surface photovoltage has recently been achieved due to the development of DSPS.[9,11] This new approach combines the advantages of the wavelength modulation with a strikingly enhanced sensitivity through utilization of the MOS structure.

In the experimental arrangement, schematically shown in Fig. 2, the surface photovoltage is measured with respect to a transparent, refer-

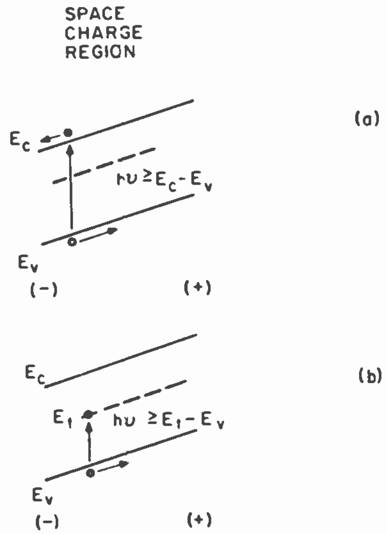

Fig. 1—Schematic representation of the mechanism of photovoltage generated (a) by intrinsic and (b) by subbandgap illumination (see text).

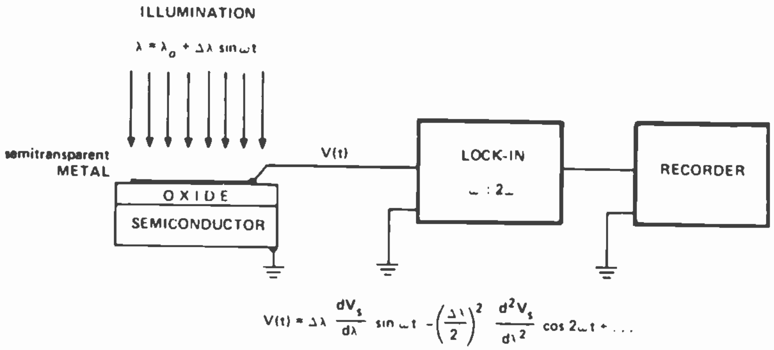

Fig. 2—Schematic representation of the experimental arrangement for derivative surface photovoltage spectroscopy.

ence, gold electrode evaporated on an oxide layer (500 to 2000 Å thick) grown on the semiconductor. With this insulating layer, a sensitivity of 50 nV can be achieved in the surface photovoltage measurements (i.e., 2 to 4 orders of magnitude higher than previously reported[9]) permitting the determination of relative changes in the surface barrier as small as about 10^{-7}. Similar measurements can be performed using a Schottky diode as a reference electrode. However, such measurements may be affected by photoinjection of carriers from metal.

In the experimental arrangement of Fig. 2 the periodic wavelength modulation of the incident light generates the photovoltage signal which is analysed directly and through the first- or the second-harmonic phase-sensitive detection. The first- and the second-harmonic detection permit the determination of the first- and second-energy (or wavelength) derivative of the surface photovoltage and thus enable a precise spectroscopic determination of the energy levels active in photo-induced transitions. The illumination intensity utilized in present measurements was on the level of 1–10 μWatt/cm^2, i.e., about seven orders of magnitude lower than in typical photoluminescence studies. The further experimental details and the example of an application of the derivative surface photovoltage spectroscopy are given in Ref. [9].

The silicon wafers used for measurements were obtained from commercial suppliers (Mansento and Wacker), and they represented the best float zone material with resistivity about 10 ohm-cm (boron doped) presently available on the market. The measurements were performed on the as-grown and oxidized wafers (oxidation done at 900°C in the steam + HCl). In the case of the oxidized wafers, a transparent layer of gold was evaporated on the oxide to serve as the reference electrode. The Schottky diodes, made by Ti evaporation, were used during measurements on the as-grown crystals. The second contact to the samples was made by silver paint and it was kept in the dark during the measurements. By applying different geometries, which change the distance that minority carriers have to diffuse to the back contact, it has been established that the back contact did not influence the measured photovoltage.

3. Results—Oxidized Wafers (MOS)

3.1 Transitions in the Vicinity of Indirect Energy Gap ($\Gamma \rightarrow X$)

To access the reliability of DSPS in determining the optically active transitions, the surface photovoltage was measured first in the vicinity of the indirect energy gap. Typical transitions detectable by DSPS in indirect-gap semiconductors (e.g., silicon) are classified in Table 1.

The first derivative surface photovoltage spectra obtained in the temperature range 300°K to 10°K are shown in Figs. 3 through 5.

Fig. 3 shows, for example, that the measured spectra are dominated by band-to-band transitions of the type 1 in Table 1. Thus, due to the phonon absorption, the maximum of 300°K occurs for $h\nu \simeq 1.05$ eV, i.e., about 55 meV (phonon energy) below the energy gap. As the temperature decreases, the second maximum develops for photon energies higher than E_g (phonon emission). At sufficiently low temperatures only the phonon emission is active. At 10°K, the spectrum is limited to the energies higher than the energy gap. The maximum corresponds to emission of optical phonons, and it occurs at $h\nu = E_g + \hbar\omega_{\mathrm{LO}}$ ($\hbar\omega_{\mathrm{LO}} \simeq 55$ meV), while the bump on the low energy side corresponds to emission of tranverse acoustic phonon (~18 meV) and it occurs at energy $h\nu = E_g + \hbar\omega_{TA}$. It is thus apparent that the total shift of the first derivative photovoltage peak between 300°K and 10°K is $\Delta E = E_g(10°\mathrm{K}) - E_g(300°\mathrm{K}) +$

Table 1—Photo-induced Transitions Observable by Derivative Surface Photovoltage Spectroscopy For Indirect Gap Semiconductors

Photo-induced Transition	Characteristic Energy		Comments
	Low Temp.	High Temp.	
1. Band-to-band transitions	$h\nu_{max} \simeq E_g + \hbar\omega_{ph}$	$h\nu_{max} \simeq E_g - \hbar\omega_{ph}$	
2. Valence-band to localized level	$h\nu_{max} \simeq E_t - E_v + n\hbar\omega_{ph}$	—	E_t must be empty
3. Localized level—to conduction band	$h\nu_{max} \simeq E_c - E_t + n\hbar\omega_{ph}$	–	$-E_t$ must be occupied
4. Localized level—to localized level	$h\nu_{max} = E_{t2} - E_{t1} + n\hbar\omega_{ph}$		E_{t1} must be occupied E_{t2} must be empty plus thermal excitation required

E_g = indirect energy gap; $n = 0.1,2, \ldots$; $\hbar\omega_{ph}$ = phonon energy.

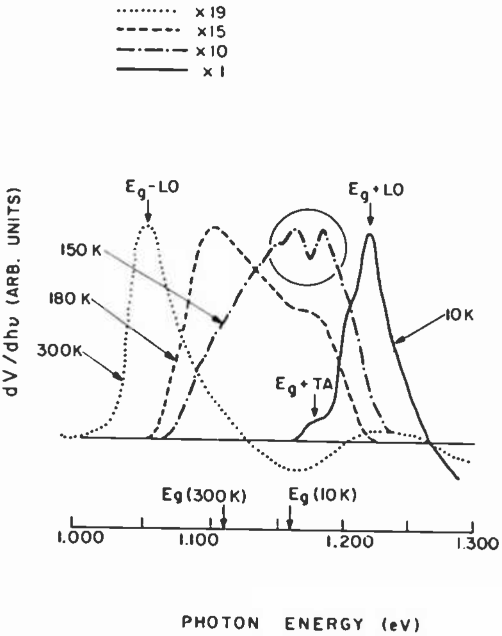

Fig. 3—First-derivative surface photovoltage spectra of sample S1 in the vicinity of indirect band-to-band transitions.

$2\hbar\omega_{LO}$, i.e., it is about three times larger than the temperature shift of the energy gap.

These findings are in excellent agreement with the existing knowledge of the band structure and the phonon spectra of Si,[13,14] and they clearly illustrate the reliability of derivative surface photovoltage spectroscopy in the determination of optically active transitions.

From the point of view of impurity related transitions, however, it is of significance to analyze the additional maximum encircled in Fig. 3, which exhibits specific characteristics. As shown in Fig. 4, this maximum is observable only at limited temperature ranges (around 160–130°K for sample S-1 and 130–70°K for sample S-2). Furthermore, it disappears under low-intensity white-light background illumination (see Fig. 5). The latter results indicate that this maximum is related to transitions involving localized levels rather than phonon-assisted band-to-band transitions. In p-type silicon, low intensity band-to-band generation can not change the occupation of hole (majority carrier) traps; however, it can noticeably increase the occupation of electron (minority carrier) traps. Thus, consistent with the results shown in Fig. 5, the maximum in question can be attributed to transitions of type 2 in Table 1, i.e., to photoionization transitions between the valence band and shallow

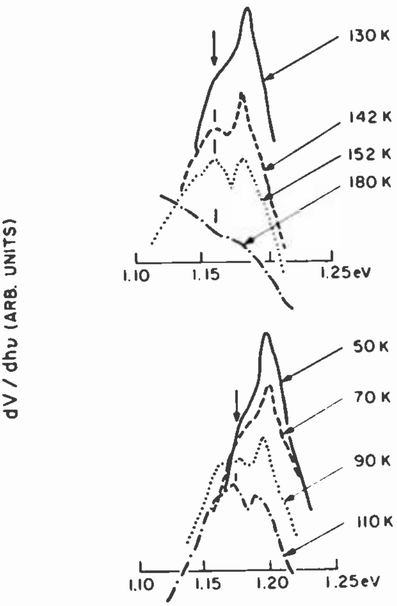

Fig. 4—Effect of temperature on transitions in the vicinity of indirect band gap.

electron traps. The fact that these transitions are observed at a limited temperature range can be explained by considering that at higher temperature, electrons that are photoionized to the localized deep level will not stay long enough at this level to make a noticeable contribution to the change of the potential barriers but will be thermally generated to the conduction band. In this case, the thermal emission will effectively quench the effect of photoionization. At sufficiently low temperature, on the other hand, the increased value of the time constant of thermal emission ($\tau > 1/\omega$) reduces the magnitude of the photovoltaic signal measured using periodical modulation with an angular frequency, ω.

The determination of the energy level E_t of electron traps involves ambiguity due to the unknown order n of phonon replica. An estimate for the value of E_t is about 0.05 eV or 0.1 eV below conduction band, taking at the maximum $n = 1$ or $n = 2$, respectively. It is of interest to note that at a given temperature, the magnitude of the peak in question was found to vary with changes in the position of the probing area within a given sample. For sample S-1, e.g., at the central part of the sample, the peak reached maximum at a T of about 150°K, while at the edges at a T of about 170°K. Demonstrated sensitivity of this peak to minority carriers (see Fig. 5) indicates that the differences within a given sample can be explained as due to local changes of the minority carrier lifetime.

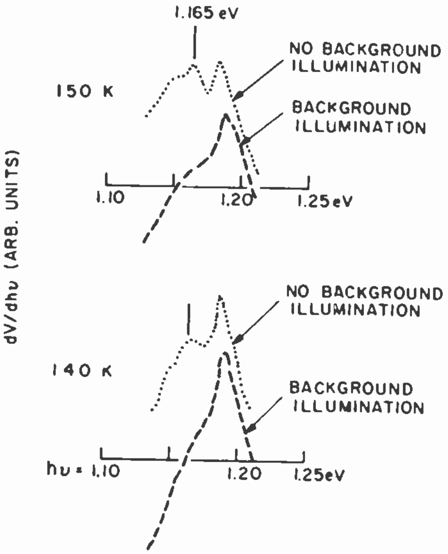

Fig. 5—Effect of white-light background illumination on transitions in the vicinity of indirect band gap.

3.2 Subbandgap Spectra—Deep Levels

For temperatures below 40°K, a pronounced subband surface photovoltage was observed that rapidly increased with decreasing temperature. A typical first-derivative spectrum of an MOS structure measured at 10°K is given in Fig. 6.

The fact that the subbandgap spectra was observed only at low temperature is consistent with photoionization transitions involving localized

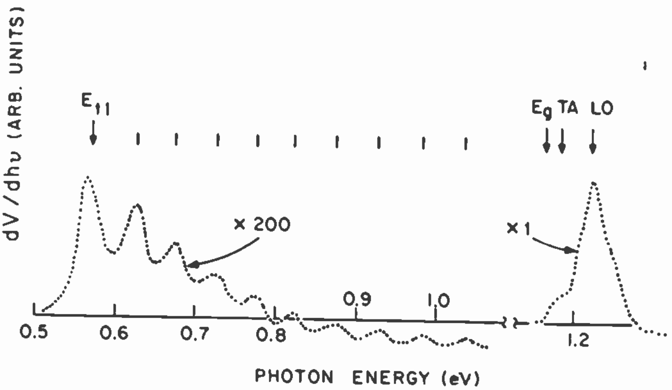

Fig. 6—Subbandgap first derivative photovoltage spectra of MOS sample at 10°K.

levels. In this case, in addition to photoionization transitions, thermal-generation transitions and recombination (trapping) transitions occur. Accordingly, photoionization transitions can lead to a measurable change in the population of localized levels (and thus to a measurable photovoltage) only if the thermal generation and the trapping are sufficiently low.

Transitions from deep levels, located around 0.55–0.58 eV, are also observed in the direct photovoltage spectra (see Fig. 7). A slowly varying (and thus, not observed in derivative spectra) photovoltage tail at lower photon energy is also seen in the spectrum of Fig. 7. It indicates additional photoionization transitions involving shallower levels ($E_{t2} < 0.5$ eV). However, the optical system employed ($h\nu \geq 0.50$ eV) did not allow for further identification of these transitions. The higher energy transitions measured by the DSPS exhibit pronounced oscillatory behavior (Fig. 6). The oscillatory behavior is analyzed in Fig. 8, where the energy at the maximum is plotted versus the consecutive number of the maximum. The slope of the straight line determines the characteristic energy $\Delta E = 54 \pm 2$ meV, which agrees very well with the longitudinal optical phonon energy at low temperatures, $\hbar\omega_{LO} = 55$ meV.[14] The interpretation of the related transitions in terms of the valence-band–localized-level transitions leads to the energy level $E_{t1} = 0.56$ eV.

From two possible transitions (i.e., 2 and 3 in Table 1), transition 2 is selected as preferable because transition 3 would require that the levels 0.56 eV below the conduction band be occupied with electrons, which is rather unlikely in p-type material with a Fermi level in the vicinity of the valence band. It should also be noted that the subbandgap transitions for sample 1 were about three times stronger than in the case of sample 2. This sensitivity to the material suggests that the deep levels are related to the bulk defects rather than to the interface states, which was con-

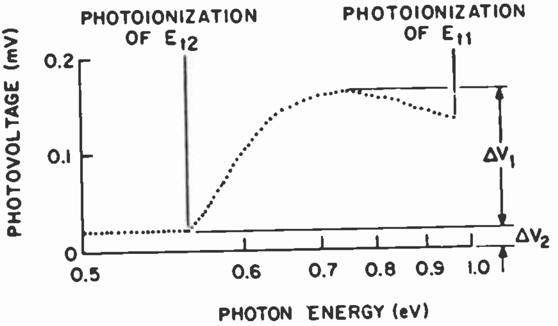

Fig. 7—Spectral dependence of steady-state subbandgap photovoltage, and the contributions of photoionization of deep levels E_{t1} and E_{t2}. Spectrum was normalized to constant photon flux.

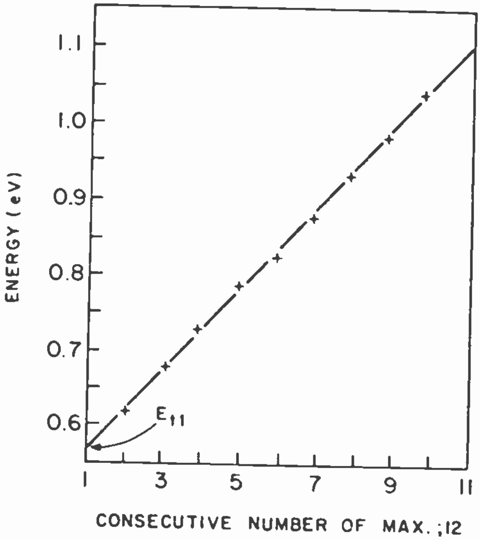

Fig. 8—Energy position of derivative photovoltage maxima versus consecutive number of maximum.

firmed by measurements performed on Schottky barriers (see next section).

4. Experimental Results—As-Grown Material

To establish unambiguously the origin of the observed deep centers (interfacial or bulk-states), the photovoltage experiments were also performed on Schottky diodes. To minimize the photoinjection from the metal to the semiconductor on the Schottky barrier, the analyzed samples were illuminated from the side of the wafer opposite to that on which the Schottky diodes were deposited.

Typical Schottky-barrier first-derivative photovoltage spectrum measured at 10°K is shown in Fig. 9a. For comparison, the spectrum obtained with thermally grown oxide is also given in Fig. 9b. It is evident that both spectra are very similar. The significance of this similarity is that it rules out the possibility of active participation of Si-oxide interface states in the observed transitions. The Schottky barrier structures were not treated at elevated temperature (unlike MOS-structures), and it is apparent that the observed transitions are due to the localized levels present in the as-grown silicon (the same levels are present in the as-grown and oxidized materials).

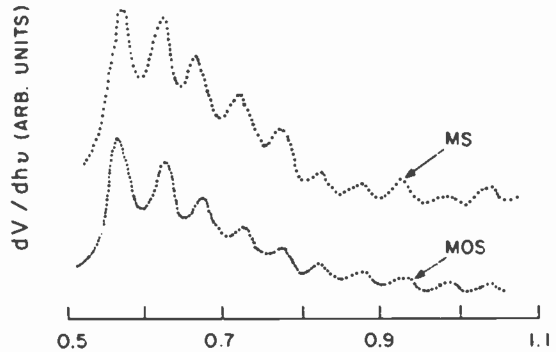

Fig. 9—First derivative surface photovoltage spectra of the as-grown sample (MS-structure) and the MOS structure (oxidized sample).

5. Procedure for Determination of the Deep Level Parameters

For small excitation level the photovoltage, ΔV, is proportional to the concentration of generated excess holes, Δp,

$$\Delta V = C\Delta p. \qquad [1]$$

For the photoionization transitions of Fig. 1b, $\Delta p = \Delta n_t$ where Δn_t is the change in concentration of electrons at levels E_t.

At low temperature, the thermal generation transitions are negligible and the rate equation for n_t is

$$\frac{dn_t}{dt} = G_I - R_{tv}, \qquad [2]$$

where G_I is the rate of photoionization transitions from valence band into the levels E_t, and R_{tv} is the rate of recombination transitions from E_t to valence band. Thus,

$$G_I = I\sigma_i N_t; \qquad R_{tv} = K_p n_t p, \qquad [3]$$

where I is the photon flux, σ_i is the photoionization cross section, N_t is the total concentration of deep levels (note that in p-type material at low temperature all deep levels are practically empty, i.e., $n_t \ll N_t$), K_p is the effective capture cross section for holes, and p is the concentration of free holes ($p = p_0 + \Delta p$ where p_0 is the hole concentration in the dark).

It follows from Eqs. [1]–[3] that

(a) the steady state photovoltage

$$V_0 = CI\sigma_i N_t \tau, \qquad [4a]$$

where

$$\tau = \frac{1}{K_p p}; \qquad [4b]$$

(b) the photovoltage transient following "illumination on" is

$$\Delta V = \Delta V_0 (1 - e^{-t/\tau}); \qquad [5]$$

(c) the photovoltage transient following "illumination off" is

$$\Delta V = \Delta V_0 e^{-t/\tau}. \qquad [6]$$

Eqs. [4]–[6] provide a simple basis for the determination of deep-level parameters from measured values of τ and ΔV_0. As discussed below, the validity of these equations has been verified by experiments performed on MOS structures.

1. It has been found that the amplitude of steady-state photovoltage ΔV_0 increases linearly with illumination intensity (see results given in Fig. 10) in agreement with Eq. [4a]. Also in agreement with expression 4, ΔV_0 was found to increase drastically with decreasing temperature (see Fig. 11). Such photovoltage enhancement at low temperature is due to a decrease of hole concentration p_0 and thus an increase of the relaxation time $\tau = 1/(K_p p)$.
2. It has been found that under low intensity subbandgap illumination ($\Delta p \ll p_0$), the photovoltage transient is exponential (Eqs. [5] and

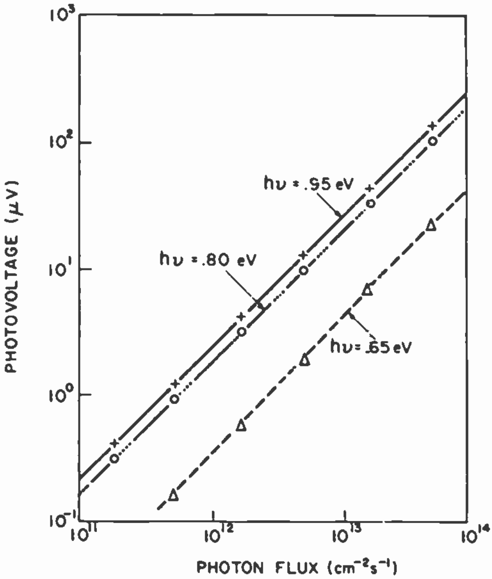

Fig. 10—The magnitude of steady-state photovoltage versus photon flux for different photon energies *hν*.

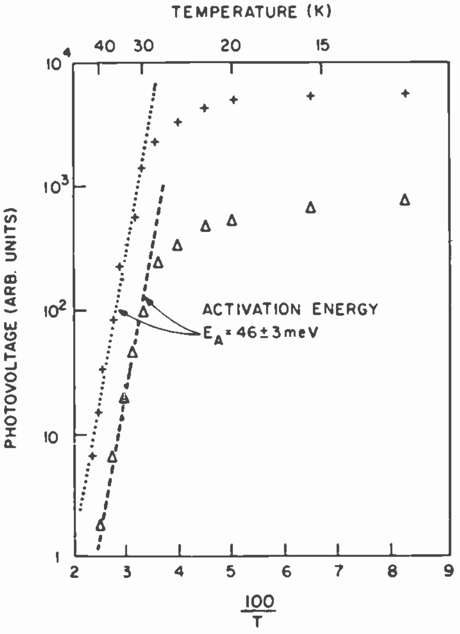

Fig. 11—Temperature dependence of steady-state photovoltage generated by photons of $h\nu = 0.75$ eV. The results for sample S1 and S2 were displaced in a vertical direction for clarity. (Identical activation energy was also obtained for incident photon energy corresponding to photoionization of the levels E_{t2}.)

[6]). The value of time constant τ increases with decreasing temperature.

3. It has also been found that at low temperatures ($T = 12°$K) and for high illumination intensity ($I > 10^{15}$ photons/cm^2 s), the time constant τ decreases with illumination intensity (i.e., Δp becomes comparable to p_0). This observation is of significance, as it enables a simple estimation of the concentration of deep levels. For example, it was observed for sample S1 at 12°K that background illumination with 2×10^{15} photons/cm^2 s of $h\nu = 0.75$ eV reduced the relaxation time by about 10%. Accordingly, Δp was estimated to be about $0.1p_0 \simeq 10^8$ cm^{-3}. From the value of Δp and the magnitude of photovoltage ΔV, the scaling factor C in Eq. [1] was evaluated, permitting the further quantitative analysis.

In the experimental determination of the relaxation time τ, the chopped light technique was employed, which enabled the use of a high-sensitivity lock-in detection of an ac signal. Thus, if subbandgap low-intensity illumination is periodically modulated with a frequency f, the measured amplitude of photovoltage is[15]

$$\Delta V_p = \Delta V_0(1 + \omega^2\tau^2)^{-1/2}, \qquad [7]$$

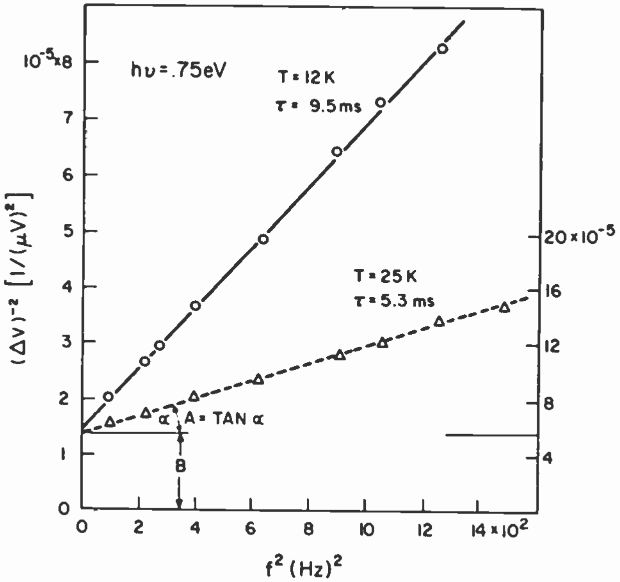

Fig. 12—Frequency dependence of photovoltage generated by periodically modulated illumination ($h\nu$ = 0.75 eV).

where $\omega = 2\pi f$.

If $(\Delta V_p)^{-2}$ is plotted versus f^2, a straight line is obtained (see Fig. 12). Using the notation of Fig. 12, the slope A and the value of B enable the determination of τ:

$$\tau = \frac{1}{2\pi} \frac{B}{A}. \qquad [8]$$

As shown in Fig. 12, τ indeed decreases with temperature, but the product $\Delta V_0/\tau$ is practically independent of temperature, in agreement with Eq. [4].

6. Quantitative Results

6.1 Compensation of the Material (Oxidized Samples)

For low illumination intensity the amplitude of steady-state photovoltage (see Eq. [4]) becomes

$$\Delta V_0 = CI\sigma_i N_t \frac{1}{K_n p_0}. \qquad [9]$$

Hole concentration p_0 is the only quantity in Eq. [9] that depends significantly on temperature. Accordingly, $\log(\Delta V_0)$ versus $1/T$ provides a simple means for determination of the freeze-out characteristics (i.e., $-\log p_0$ versus $1/T$). The results obtained for the samples S1 and S2 are given in Fig. 12. The obtained activation energy is in excellent agreement with the energy level of a shallow acceptor due to the boron $E_A = 46$ meV.[16,17]

The freeze-out characteristic in the form $e^{-E_A/kT}$ is significant,[18] as it indicates that the supplied samples exhibit noticeable compensation (note that for noncompensated material the freeze-out characteristic should be $p \sim e^{-E_A/2kT}$).[18] Thus, for the temperature range of Fig. 12, the concentration of compensating donor centers, N_D, in Si samples must satisfy the inequality $N_D \gg \frac{1}{2} N_v e^{-E_A/kT}$,[18,19] where N_v is the effective valence band density of states; i.e., N_D can realistically be estimated as much higher than 10^{13} cm^{-3}.

6.2 Parameters of Deep Levels

From the measured values of the relaxation time at photon energy corresponding to photoionization of the previously reported deep levels, the effective capture cross section has been determined at $T = 12°$K for the samples S1 and S2. For the Si samples, p_0 at 12°K was estimated to be about 10^9 cm^{-3}. Utilizing this value and the measured time constant, τ, the capture cross section for holes was estimated as $\sigma_p = (\tau p_0 v_T)^{-1}$, where $v_T = (3kT/m^*_0)$ is the thermal velocity of the holes.

The concentration of deep levels N_t was estimated from Eq. [4], and the magnitude of contribution to the photovoltage was provided by a given level (ΔV_1 and ΔV_2 for levels E_{t1} and E_{t2}, as, for example, in Fig. 7). The required values of photoionization cross sections σ_i were estimated from the quantum defect model ($\sigma_i = [2.5 \times 10^{-18}\ \text{cm}^2]/E_t{}^2$).[20]

The obtained dynamic parameters of deep levels are listed in Table 2. It should be mentioned that although the absolute values of these parameters contain uncertainty due to estimation of hole concentration, p_0 and/or the value of photoionization cross section σ_i, the relative changes of N_t between samples S1 and S2 are determined with much better accuracy (about 20%).

Table 2—Deep-Level Parameters

	E_t	τ at 12°K (ms)		σ_p		
Leveq	(eV)	Sample 1	Sample 2	(cm)	Sample 1	Sample 2
E_{t1}	0.56	11	9.5	$\sim 10^{-14}$	2×10^{13}	9×10^{12}
E_{t2}	<0.5	>45	>40	$>2 \times 10^{-15}$	$<10^{12}$	$<5 \times 10^{11}$

7. Summary

High resolution measurements of the derivative surface photovoltage spectroscopy have revealed the presence of deep and shallow energy levels in the as-grown and oxidized samples of high quality float zone Si. Thus, deep level transitions at energies $E_{t1} = 0.56$ eV and $E_{t2} < 0.5$ eV were clearly observed at temperatures below 30°K. Higher energy transitions are characterized by strong coupling with phonons, and corresponding energy levels apparently represent the recombination levels. It is also shown that these levels are due to the bulk states rather than interface states.

The transitions to the shallow level (45 meV below energy gap) have been observed for a narrow temperature range, and they have been tentatively identified as valence band–shallow electron trap transitions.

Transient characteristics of the photovoltage were employed to evaluate the concentration and the capture cross section of residual deep levels in high purity Si. It has been found that the concentration of the levels in the oxidized wafers is between 10^{11} and 10^{13} cm^{-3} and the capture cross section for holes is 10^{-14} cm^2 or less. From free hole freeze-out characteristics, it has been established that the high purity p-type Si contains shallow compensating donors at a concentration much higher than 10^{13} cm^{-3}. The concentration of deep and shallow centers has been found to exhibit noticeable variations between the analyzed samples.

References:

[1] C. T. Sah and C. T. Wang, *J. Appl. Phys.*, **46**, p. 1767 (1975).

[2] P. M. Petroff, D. V. Lang, J. L. Strudel and R. A. Logan, *Scanning Electron Microscopy* (1978), Vol. 1, p. 325, SEM Inc., AMF O'Hare.

[3] L. Jastrzebski, P. Levine, D. Cope, W. Fisher, D. Savoye, and W. Henry, 157th Electrochem. Soc. Meeting, St. Louis, May 1980 (abstract No. 150) (to be published in *J. Electrochem. Soc.*).

[4] L. Jastrzebski and J. Lagowski, 17th Electrochem. Soc. Meeting, St. Louis, May 1980 (abstract No. 152) (to be published in the *J. Electrochem. Soc.*).

[5] For review, see C. T. Sah, *Semiconductor Silicon 1977*, H. R. Duff and E. Sirtl, Editors, p. 868, The Electrochem. Soc. Softbound Symposium Series, Princeton, NJ (1977); G. L. Miller, D. V. Lang and L. C. Kimerling, *Ann. Rev. Material Sci.*, 1977, p. 377; H. G. Grimmeiss, *Ann. Rev. Material Sci.*, 1977, p. 341.

[6] H. M. DeAngelis, J. W. Diebold and L. C. Kimerling, *Radiation Damage and Defects in Semiconductors*, London Institute of Physics, 1973, p. 295.

[7] See e.g., J. A. Pals, *Solid State Electron*, **17**, p. 1139 (1974).

[8] See e.g., O. Engstrom and H. G. Grimmeiss, *J. Appl. Phys.*, **47**, p. 4030 (1976).

[9] J. Lagowski, W. Walukiewicz, M. M. G. Slusarczuk, and H. C. Gatos, *J. Appl. Phys.*, **50**, p. 5059 (1979).

[10] E. Kamienicki, J. Lagowski, and H. C. Gatos, *J. Appl. Phys.* (1980) (in press).

[11] J. Lagowski, Proc. of 3rd Univ./Industry/Government Microelectronic Symp., Lubbock, Texas, 1979, *IEEE Conf. Record*, p. 1.

[12] L. Jastrzebski, P. Levine, D. Cope, W. Kosnocky, W. Henry, and D. Battson (submitted to *IEEE Proceedings*).

[13] See, for example, *Handbook of Electronic Materials*, ed. M. Neuberger, IFI/Plenum, New York, 1971, Vol. 5.

[14] K. L. Shaklee and R. E. Nahory, *Phys. Rev. Lett.*, **28**, p. 942 (1970).

[15] S. M. Ryvkin, *Photoelectric Effects in Semiconductors*, New York Consultants Bureau, 1964, ch. III.

[16] J. P. Maitz, *Phys. Rev.*, **96**, p. 28 (1954); F. J. Morin, et al., *Phys. Rev.*, **96**, p. 833 (1954).

[17] E. Burstein, et al., *J. Phys. Chem.*, **57**, p. 849 (1953).

[18] See, for example, R. A. Smith, *Semiconductors*, Cambridge University Press (1959). Ch. 4, 3, p. 82–92.

[19] S. M. Sze, *Physics of Semiconductor Devices*, John Wiley & Sons, New York, 1969, p. 35.

[20] See, for example, P. R. Bratt in *Semiconductors and Semimetals*, ed. R. K. Willardson and A. C. Beer, Academic Press, New York, 1977, Vol. 12, Ch. 12, and references quoted therein.

[21] From the measurement of diffusion length done by surface photovoltage, e.g., *Annual Book of ASTM Standards* (ASTM, Philadelphia, 1974), p. 752.

GaAs MESFET Comparators for Gigabit-Rate Analog-to-Digital Converters

L. C. Upadhyayula

RCA Laboratories, Princeton, NJ 08540

Abstract—A novel MESFET comparator circuit has been proposed. A three-comparator circuit has been fabricated with discrete GaAs FETs and evaluated up to 250-MHz clock rates. The comparators and coding logic for a 2-bit A/D converter have also been designed. The performance of the converter has been studied using a computer simulation program. The simulations indicate that the circuit will function satisfactorily up to 1.0 GHz sampling rates. The development of a monolithic IC chip consisting of comparators and coding logic is also reported.

Introduction

Multigigabit-rate signal and data processing is required for government as well as commercial systems of the mid-to-late 1980s. Analog-to-digital converters are an essential part of such signal processing circuits. McCabe[1] and Griffiths[2] have reported that three- to four-bit A/D working at 1–2 GHz sampling rates will satisfy the needs of many future systems. The fastest silicon bipolar-technology based A/D is a 5-bit A/D operating at 400 MS/s reported by DeGraafe.[3] It is believed that, due to excessive power dissipation, this technology cannot be advanced to higher sampling rates. In the past four or five years, GaAs-based technology has emerged as a candidate for high-speed signal processing. D. C. Claxton, et al.,[4] attempted to develop a 1-bit A/D cell using a combination of GaAs transferred-electron logic devices (TELDs) and field-effect transistors. This work was plagued by the poor performance of the TELDs, their bias instabilities, and low gain in the MESFETs. New circuit approaches and/or novel applications of the state of the art devices are necessary to meet the gigabit-rate A/D requirement.

An excellent review on analog-to-digital converters (ADC) was given by Gordon, et al.[5] A parallel comparator ADC, which represents the architecture with the highest speed and a reasonable accuracy, is schematically shown in Fig. 1. The critical components in an ADC are (1) sample and hold circuits, (2) amplifiers, (3) threshold comparators, and (4) latches and decoder logic circuits. The speed of an ADC is determined by the speeds of the individual components. Operating at room temperature ambient, GaAs MESFETs demonstrated 32–60 ps propagation delays[6,7] and power amplification up to 37 GHz.[8] These properties have been utilized in developing high-speed sample and hold circuits,[9] amplifiers,[10] and digital logic circuits.[11,12]

GaAs MESFET comparators operating at 1–2 GHz rates were first proposed by the author recently[13] and are the subject of this paper. We concern ourselves with the design, fabrication, and evaluation of these comparators. A novel FET comparator circuit is described. Experimental results on an MIC three-comparator circuit with discrete GaAs FETs are reported. The design of a monolithic comparator for a 2-bit A/D is discussed and the results of a computer simulation of its performance are presented. The development of a monolithic integrated circuit chip consisting of comparators and coding logic are also reported.

Principles of Operation of MESFET Comparators

A comparator circuit is one that is used to mark the instant when an input signal with an arbitrary waveform attains some reference or threshold level, at which point the comparator output changes abruptly from its quiescent value. A block diagram of the comparator and its output waveform are shown Fig. 2. The output remains at quiescent value for input signal levels below the reference or threshold level. The

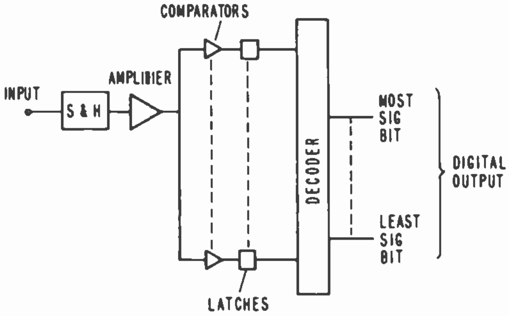

Fig. 1—Schematic of a parallel comparator analog-to-digital converter.

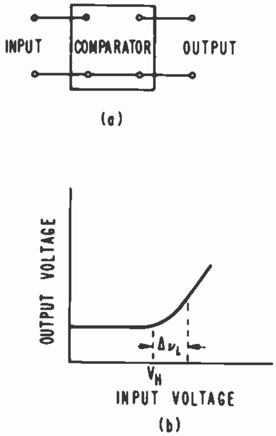

Fig. 2—A block diagram of a comparator and its transfer characteristics.

threshold voltage (V_{th}) can be varied by varying the circuit parameters or operating point. The slope of the output is determined by the gain in the comparator circuit. The device to which the comparator output is applied will respond when the comparator output rises to some level. As a consequence, there is variability ΔV_i in the precise moment at which the device responds and an uncertainty Δt in time corresponding to this. ΔV_i should be small compared to the threshold voltage (V_{th}).

An FET comparator circuit is shown in Fig. 3. This circuit looks similar to a single-input inverter used in digital circuits, but the similarity ends right there. The device and material requirements are totally different from that for the digital circuits. The comparator circuit consists of a

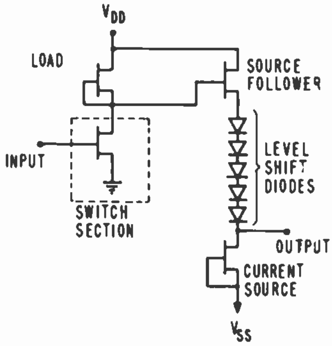

Fig. 3—FET Comparator.

switch transistor (T_S), a load transistor (T_L), and a level shifting circuit that makes the output pulses compatible with the input requirements of the following digital circuit. The drain saturation current for the switching transistor is higher than that for the load transistor. A negative-going input pulse at the switch transistor gate electrode makes it less conducting, allowing the internal node voltage to rise. As the input pulse varies from 0 volts to about −1.2 volts, the node voltage rises from +0.5 volts to +4.0 volts. The level shifting circuit translates this to an output whose amplitude and dc level are compatible with the input pulse required for driving digital logic circuits.

The response (rise) time and the threshold level of the comparator are determined as follows. The critical node in this comparator circuit is the drain of the switch transistor. The rise and fall times of the output pulse are determined by the charging and discharging of the load capacitance present at this node. The switch and load transistors along with the capacitive load is shown in Fig. 4a. The current voltage characteristic of the switch transistor with the load line superimposed is shown in Fig. 4b. When the input to the gate of the switch transistor is 0.0 V, the output stays at V_L which is of the order of 0.5 V. Application of a negative signal at the gate of T_S decreases its drain current and changes the point of intersection for the load line. However, the voltage at the output node does not change appreciably until the drain current of the switching transistor is equal to that of the load transistor. When the input voltage becomes more negative, the operating point shifts to V_H. The capacitance load presented at the drain must be charged before this voltage transition occurs. The rate at which the drain voltage changes is given by

$$\frac{\Delta V}{\Delta t} = \frac{\Delta I}{C}, \qquad [1]$$

where ΔI is the current available for charging, C is the load capacitance,

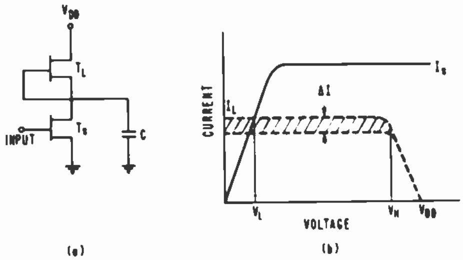

Fig. 4—Current-voltage characteristic of the threshold circuit for comparator operation.

ΔV is the voltage transition and Δt is the switching (rise) time. For a typical circuit, $C \simeq 0.02$ pF and $\Delta V \simeq 3.0$ V. Hence, a 0.6-mA current change will be required to make the transition in 100 ps. The rise time is thus dependent upon the current drive capability.

The switching transition takes place when the drain current of the switch transistor (T_S) is equal to that of the load transistor (T_L). This is achieved by the application of an input signal V_G at the gate of T_S. The condition for the drain currents of T_S and T_L to be equal is given by:

$$1 = \frac{I_{DS}}{I_{DL}} = K\left[\frac{(1 - \eta^{1/2})}{(1 - \eta_s{}^{1/2})}\right] \qquad [2]$$

where

$\eta_S = V_B/V_P, \quad \eta = (V_G + V_B)/V_P,$

$V_B \doteq$ built-in Schottky barrier voltage;

$V_P =$ channel pinch-off voltage;

$K =$ width of the switch transistor/width of the load transistor.

For Schottky barriers on GaAs, V_B is of the order of 0.4 to 0.6 V. For a given channel pinch-off voltage and desired threshold voltage ($V_G = V_{th}$), the design parameter K is evaluated from Eq. [2]. The design of a three-comparator circuit for a 2-bit A/D will be discussed later.

Experimental Results on an MIC Comparator with Discrete MESFETs

The principle of FET comparators is demonstrated using the three-

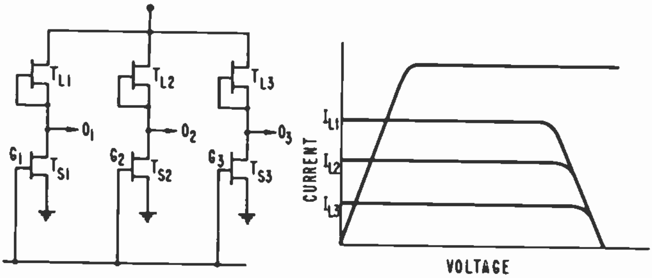

(a) (b)

Fig. 5—A three-comparator circuit.

comparator circuit shown in Fig. 5. This circuit was fabricated in MIC form using discrete GaAs power FETs. Each of the FETs has four gate stripes and each stripe is 150 μm wide. The four gates of each switch transistor (T_{S1}, T_{S2}, and T_{S3}) are connected in parallel resulting in a total gate width for each of 600 μm. For the load transistors T_{L1}, T_{L2}, and T_{L3}, we have used three, two, and one gate stripes, respectively. These transistors were mounted in an MIC circuit to provide 50 ohm connections for the input and output signals. The input pulse was provided from an HP 214 or 8091 pulser.

The output was measured on a sampling oscilloscope with and without high impedance probes. The high impedance probe was used to minimize the capacitive loading. The performance of the comparators for dc or low frequency input signals is shown in Fig. 6. Note the three distinct threshold levels for the three comparators. The performance on the comparator circuit for a 250 MHz input signal is shown in Fig. 7. The operation of this circuit was very satisfactory. In our experiments, the output was measured at the comparators with a sampling oscilloscope fitted with high impedance probes. No output driver or source follower stages were used. In general, the output driver greatly enhances the circuit's ability to drive a bigger (capacitive) load of other circuits with a minimal increase in propagation delay.

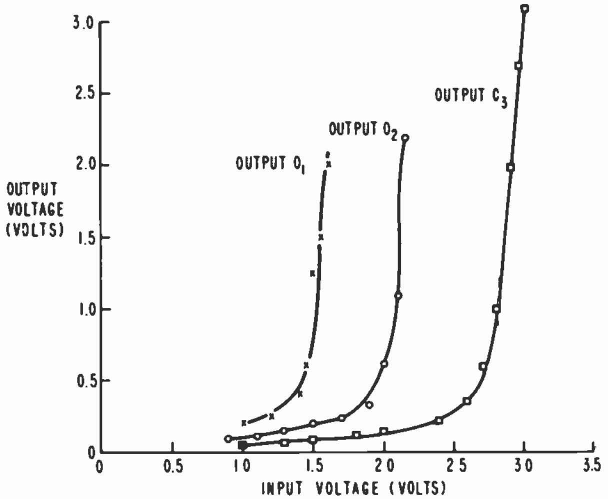

Fig. 6—Performance of a GaAs three comparator circuit; discrete FETs were used in an MIC circuit.

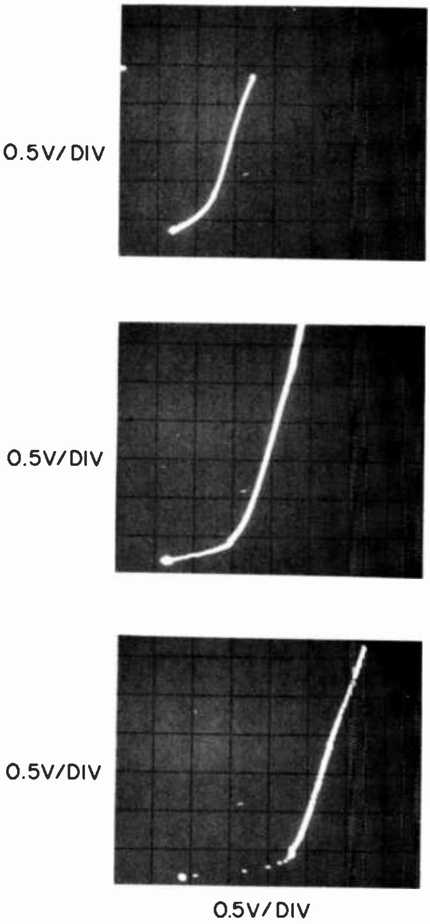

Fig. 7—Response of the three-comparator circuit to 250 MHz input signal.

Monolithic A/D Design

A two-bit A/D is shown schematically in Fig. 8. It has three comparators and binary coding logic. The comparators are the FET comparators discussed earlier and the logic gates are the standard depletion mode NAND/NOR gates. A circuit diagram of the two-bit A/D including the comparators and coding logic is shown in Fig. 9. The comparator threshold voltages have been set to 0.4, 0.8, and 1.2 V. The parameter $1/K$ (i.e., ratio of the widths of the load and switch transistors) has been calculated for these three threshold voltages from Eq. [2] and the results are presented in Table 1. A channel pinch-off voltage $V_P = 5$ V is as-

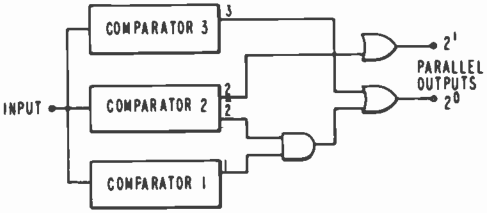

Fig. 8—Block diagram of a parallel threshold A/D converter.

sumed and a Schottky barrier built-in potential of 0.4 and 0.6 V is used. From Table 1 it is clear that the parameter $1/K$ is not very sensitive to the variation of Schottky barrier potential. Furthermore, photolithographic techniques allow geometry control to within a micrometer. Therefore, these comparators are realizable in practice. This design procedure gives us the ratio of the widths of the load and switch FETs only. The actual widths have to be determined from the overdrive voltage required to make the transition at the threshold level.

The overdrive voltage (ΔV_g) required for FET comparators is determined as follows. The comparator outputs have to drive the logic gates used for binary coded conversion. These logic gates will respond as soon as the comparator voltage has reached a certain level. At the threshold value, the transition from LOW to HIGH or HIGH to LOW takes place with a small change in input gate voltage (ΔV_g). This value of the gate voltage should be very small compared to the least significant bit (LSB) for A/D. As discussed before, the load and the switching transistors of the comparator provide the charging or discharging currents, respectively, for the capacitive load. The load on the comparator is the input capacitance of the source follower and is of the order of 0.02 pF. Therefore, the current required for charging or discharging is

$$\Delta I = C\frac{\Delta V}{\Delta t}. \qquad [3]$$

Table 1—Comparator Design Parameters for 2-Bit A/D.

Comparator Threshold	Built-In Voltage	Width of the Load FET/Width of the Switch FET	
		$V_p = 5$ V	$V_p = 6$ V
0.4 V	0.6 V	0.845	0.865
0.8		0.720	0.756
1.2		0.612	0.661
0.4	0.4 V	0.837	0.856
0.8		0.711	0.745
1.2		0.606	0.652

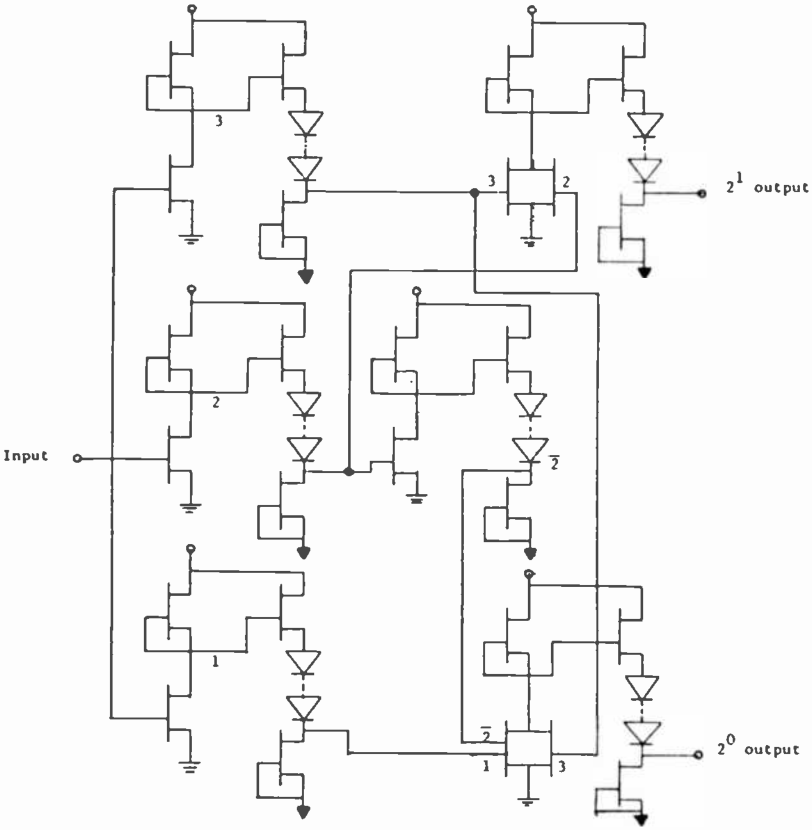

Fig. 9—Circuit diagram of the two-bit A/D.

The voltage change at the comparator output is of the order of 3 V. For the switching transition to occur in 100 ps, a current change of 0.6 mA is needed. The change in FET current is caused by a voltage change (ΔV_g) at the gate and is given by:

$$\Delta I = g_m \Delta V_g, \qquad [4]$$

where g_m is the transconductance. An FET with 6-mS transconductance will bring the 0.6-mA current change for $\Delta V_g = 0.1$ V.

The minimum size of the FET was determined from the graphical design procedures described by R. B. Fair.[14] The optimum doping density for FETs is $8 - 10 \times 10^{16}\text{cm}^{-3}$. The minimum gate length possible with optical lithography and contact printing is 1.0 μm. The drain saturation current (I_{DSS}) and transconductance as computed from Figs. 4 and 6 of Fair[14] are $I_{DSS} = 17.5 - 20$ mA and $g_m = 7.0 - 7.5$ mS for a 100 μm wide device with 5–6 V channel pinch-off voltage. The widths of the load transistors are then obtained from the $1/K$ values given in Table 1. The driver/level shifting circuits and the NAND/NOR gates were designed using standard techniques.

Fig. 10 shows the layout of the 2-bit A/D. The total power dissipation for the proposed all-parallel 2-bit A/D converter using GaAs FETs is about 400 mW. This corresponds to about 200 mW per bit, which is substantially lower than that for silicon bipolar-based A/D circuits.

Sensitivity of the circuit to process variations can be a problem. The device parameters that vary during processing and that we generally come across in GaAs MESFETs are (a) Schottky barrier built-in voltage (V_B) and (b) the pinch-off voltage (V_p). The variation in V_p occurs due to changes in doping density and channel thickness. It was pointed out earlier that variations in V_B do not effect the step size (see Table 1) and,

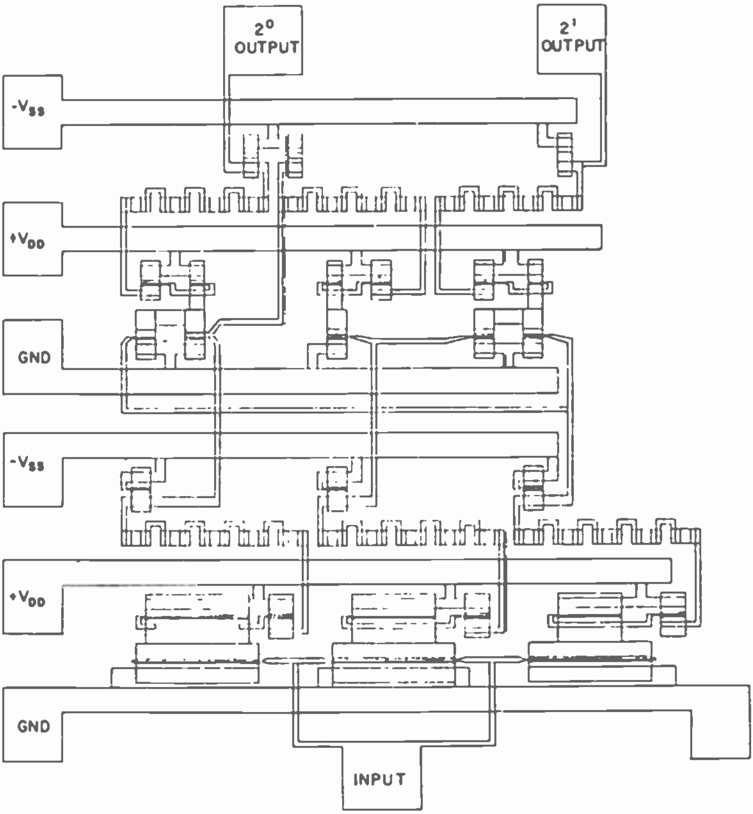

Fig. 10—Layout of the 2-bit A/D.

Table 2—Effect of Pinch-off Voltage on Comparator Threshold Voltage.

	Threshold Voltage (V_{th})(Volts)		
$1/K$	$V_P = 6.0$ V	$V_P = 5.0$ V	$V_P = 4.0$ V
0.845	0.470	0.40	0.32
0.720	0.946	0.80	0.649
0.612	1.429	1.20	0.963

therefore, the comparator performance. The step size does vary with changes in pinch-off voltage, however. The variation of step size for a ±20% variation in pinch-off voltage is shown in Table 2.

A pinch-off voltage of 5 V, a step size of 0.4 V, and Schottky built-in voltage of 0.6 V were used in these calculations. From the table, it is clear that the linearity is maintained even though the step size is changed. Because the change in the step size is linear, it can easily be accounted for by adjusting the gain of the amplifier in front of the comparators (see Fig. 1).

Computer Simulation of the 2-Bit A/D

Before fabricating the IC chip, the performance of the comparator and level shifting circuits was studied using a computer program with a user-defined model for the GaAs FET. This user-defined model requires measured device parameters, and the *I-V* characteristics of the discrete power FETs were used to obtain these parameters. The output of the three comparators and level shifting circuits was monitored as a function of input signal voltage. Threshold characteristics and response time are the two important parameters of interest. A slowly varying input signal was used to determine the threshold characteristics. The comparator response as a function of input voltage is shown in Fig. 11 for threshold voltages of 0.4, 0.8, and 1.2 V. The comparator output changes from LOW to HIGH for an input voltage change of 0.1 V around the threshold values. These results are in good agreement with the design goals. The actual output levels are 1.0 V for LOW and 5.0 V for HIGH. These voltage levels have to be brought back to logic levels using level shifting circuits. The level shifted output of the comparators is shown in Fig. 12. In the absence of an input signal, the level shifted outputs are −2.5 to −3.0 V and correspond to logic "0". When the input signal reaches the threshold value, the level shifted outputs reach 0 to +0.5 V corresponding to logic "1". It appears that the transition from LOW to HIGH of the level shifted outputs is much sharper than the comparator outputs themselves.

In the final application, a sample-and-hold signal will feed the comparators. The level shifted comparator outputs are therefore studied with sample-and-hold type input signals. A sample time of 100 ps and a hold

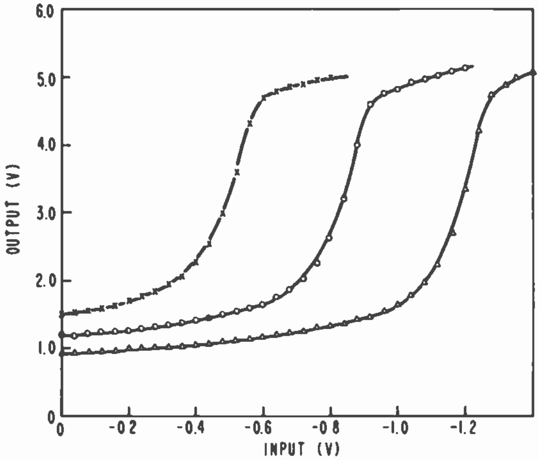

Fig. 11—Computer simulation of the comparator response for 2-bit A/D.

time of 400 ps were used for these simulations. The response of one of the comparators is plotted in Fig. 13. From this plot, the comparator response time seems to be about 300–400 ps.

These computer simulations indicate that the comparator and level shifting circuits work very satisfactorily at above 1.0 GHz sampling rates.

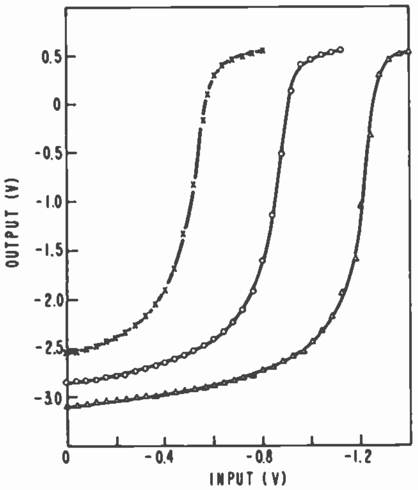

Fig. 12—Computer simulation of the comparator and level shifting circuits for 2-bit A/D.

Fabrication of Monolithic A/D Circuits

A tentative process schedule was developed for the IC fabrication. Eight masking steps are necessary to complete the IC. Au:Ge/Ni alloyed ohmic contacts are used for source and drain. Ti/Pd/Au metal system is used for Schottky barrier gates and interconnections. The IC fabrication has been completed. Fig. 14 shows a photomicrograph of a fabricated chip. Test circuits are being evaluated now and the IC will be evaluated soon.

Conclusions

A novel GaAs MESFET circuit has been proposed for high-speed comparator applications. The operation of such comparators has been successfully demonstrated experimentally up to 250 MHz clock frequencies using a hybrid MIC circuit with discrete MESFETs. Comparators and binary coded logic circuits have been designed for a 2-bit A/D. Computer simulations of this circuit indicate that it will function satisfactorily above one GHz sampling rate. A GaAs monolithic IC chip consisting of the comparators and coding logic is being developed. The availability of these comparators will make it possible to develop a single chip GaAs MESFET A/D working at a gigabit sampling rate.

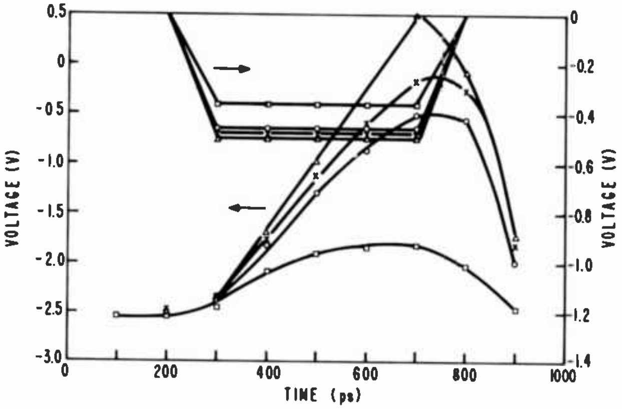

Fig. 13—Computer simulation of the response of LSB comparator for sample-and-hold input.

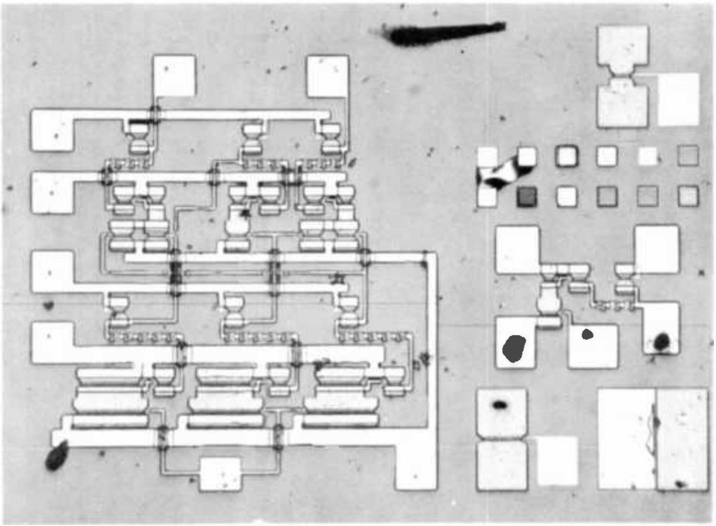

Fig. 14—Photomicrograph of a 2-bit A/D chip fabricated.

Acknowledgment

The author would like to thank Dr. W. R. Curtice for providing the model of the GaAs FET used in the computer simulations. The author is also indebted to Dr. S. Y. Narayan and Dr. F. Sterzer for many stimulating discussions.

References:

[1] Robert McCabe, Panel discussion at Workshop on High-Speed A/D Conversion, Portland, OR, Oct. 1978.

[2] Lloyd J. Griffiths, "Hybrid Adaptive Array Processing Using A/D Converters," Digest of papers, First Specialty Conference on Gigabit Logic for Microwave Systems, Orlando, FL, pp. 51–52, May 1979.

[3] K. DeGraafe, "A Silicon 400 MS/s 5-Bit A/D Converter," Workshop on High-Speed A/D Conversion, Portland, OR, Oct. 1978.

[4] D. L. Claxton, et al., "TED IC Technique Evaluation and A/D Cell Development," *ONR Final Rept.*, Contract No. N00014-76-C-0743, TRW Defense and Space Systems Group, Redondo Beach, CA, February 1978.

[5] B. M. Gordon, "Linear Electronic Analog/Digital Conversion Architectures, Their Origins, Parameters, Limitations and Applications," *IEEE Trans. Circuits and Systems*, p. 391, July 1978.

[6] R. L. VanTuyl and C. A. Leichti, "High-Speed Integrated Logic with GaAs MESFETs," *ISSCC Digest of Tech. Papers*, p. 20 Feb. 1974.

[7] P. T. Greiling, C. F. Krum, F. S. Ozdemir, L. H. Hacket, and R. F. Lohr, Jr., "Electron-Beam Fabricated GaAs FET Inverter," 36th Annual Device Research Conf., June 1978, Univ. of Cal, Santa Barbara, CA.

[8] J. M. Schellenberg, et al., "RF Characteristics of Ku-Band FETs," Seventh Biennial Conf. on Active Microwave Semiconductor Devices and Circuits, Aug. 1979, Cornell Univ., Ithaca, NY.

[9] P. H. Saul, "A GaAs MESFET Sample and Hold Switch," to be presented at the 1979 European Solid State Circuits Conf., 1979.

[10] R. L. VanTuyl, "A Monolithic Integrated 4 GHz Amplifier," *ISSCC Digest of Tech. Papers*, p. 72, Feb. 1978.

[11] R. L. VanTuyl and C. A. Leichti, "High-Speed GaAs MSI," *ISSCC Digest of Technical Papers*, p. 20, Feb. 1976.

[12] R. C. Eden, et al., "Low Power GaAs Digital ICs Using Schottky Diode FET Logic," *ISSCC Digest of Technical Papers*, p. 68 Feb. 1978.

[13] L. C. Upadhyayula," GaAs FET Comparators for high-speed Analog-to-Digital Conversion," *Digest of Technical Papers, GaAs IC Symposium*, Lake Tahoe, Nevada, Sept. 1979.

[14] R. B. Fair, "Graphical Design and Iterative Analysis of the DC Parameters of GaAs FETs," *IEEE Trans. Electron Dev.*, **Ed-21**(6), 357, June 1974.

Comparison of Phase-Only and Conventional Monopulse in Thermal Noise

Carmen N. Campopiano

RCA Missile and Surface Radar Div., Moorestown, NJ 08057

Raymond S. Berkowitz

Moore School of Electrical Engineering, University of Pennsylvania,
Philadelphia, PA

Abstract—This paper compares the noise immunity of two monopulse algorithms—a form of conventional monopulse and a phase-only algorithm. Specifically, we treat pulse compression systems with pseudorandom coding in additive thermal noise. It is shown that, in the absence of limiting, the two algorithms have essentially identical performance, provided the ratio of energy over noise power density (E/N_0) is at least 14 dB, and that the target offset from the null is small. With hard i-f limiting, the conventional monopulse algorithm treated here cannot operate, while the phase-only algorithm suffers a loss relative to linear operation of 2 dB or less.

1. Introduction

In this paper, we compare the angle estimation performance of a form of conventional monopulse with a phase-only algorithm in thermal noise. The phase-only algorithm is useful in that it can still perform well with amplitude limiting. On the other hand, it is important to compare the phase-only system with conventional monopulse in order to determine how much one gives up for this compatibility with limiting. This comparison is made here. Both analytic and Monte Carlo results are given. To be concrete, we use both algorithms in a system with pseudorandom coded waveforms and pulse compression.

The presentation is organized as follows. The two monopulse algorithms are defined in Sec. 2. Models for the performance of these algorithms in thermal noise are given in Sec. 3, and the models are analyzed in Sec. 4. Both Monte Carlo and approximate analytical results are presented in Sec. 5. Conclusions appear in Sec. 6.

2. Definition of the Monopulse Algorithms

Before developing a model of the signal processing and thermal noise effects (see Sec. 3), we define the two monopulse algorithms under discussion. We suppose that an antenna, e.g., an array, supplies the receiver/signal processor with two phasor inputs

$$\begin{aligned} \textstyle\sum_i (t) &= e_m P(t) g(\theta) e^{j\phi} = \text{sum beam phasor} \\ \Delta_i(t) &= e_m P(t) h(\theta) e^{j\phi} = \text{difference beam phasor,} \end{aligned} \qquad [1]$$

where

$g(\theta)$ = sum beam pattern

$h(\theta)$ = difference beam pattern

θ = target offset from monopulse null
(normally one of two angle coordinates)

ϕ = phase of received waveform relative to local reference

$P(t) = \pm 1$ = pseudorandum modulating waveform

e_m = received peak signal amplitude.

For simplicity we treat only one angle coordinate.

In the absence of noise and instrumentation errors we would have

$$\frac{\Delta_i}{\sum_i} = \frac{h(\theta)}{g(\theta)} = \rho = f(\theta) \qquad [2]$$

where ρ is the monopulse error ratio. The relation $\rho = f(\theta)$ is determined by the antenna. The function of a monopulse algorithm is to estimate ρ.

Let us define the monopulse algorithms to be considered here. Let Σ and Δ represent the sum and difference signals that result after Σ_i and Δ_i are contaminated by additive noise and the resulting noisy waveforms are subjected to pulse compression. By *conventional monopulse*, we mean a process that estimates ρ by evaluating

$$\text{Re}\left\{\frac{\Delta}{\sum}\right\} = \text{Im}\left(\frac{j\Delta}{\sum}\right).$$

By the *phase-only* algorithm we mean a procedure that obtains $\rho(\theta)$ by computing

$$\tan\{\arg(\Sigma + j\Delta) - \arg(\Sigma)\}$$

(see Fig. 1). In the next Section we present specific implementations for these two procedures.

The monopulse ratio ρ in Eq. [2] is generally a nonlinear function of θ, say $\rho = f(\theta)$. For small values of θ for which $f(\theta)$ is approximately linear, one may write

$$\rho = k\theta, \qquad [3]$$

where k is the monopulse error slope at the monopulse null.

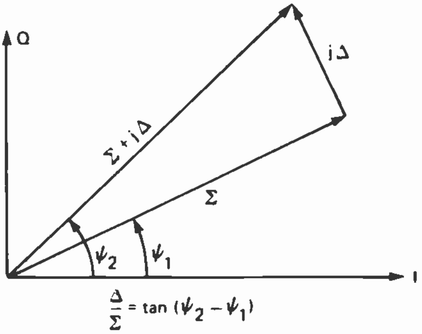

Fig. 1—Geometric interpretation of the phase-only algorithm.

3. Models for the Two Monopulse Angle Estimators

Let us construct a model, including thermal noise, for each of the two monopulse algorithms. In order to make a fair comparison of the two estimators, we supply each with essentially the same kind of signal processing.

3.1 Model for the Phase-Only Algorithm

For the phase-only algorithm consider Fig. 2. The input signals $\Sigma_i(t)$ and $\Delta_i(t)$ are given by Eqs. [1]. The additive noise terms are

$$\begin{aligned} n_\Sigma(t) &= n_1(t) + jn_2(t) \\ n_\Delta(t) &= n_3(t) + jn_4(t) \end{aligned} \qquad [4]$$

where $n_1(t), \ldots, n_4(t)$ are the in-phase and guadrature-phase components of the noise in the two channels, which are assumed to be zero-mean, independent gaussian random processes with a flat spectrum over

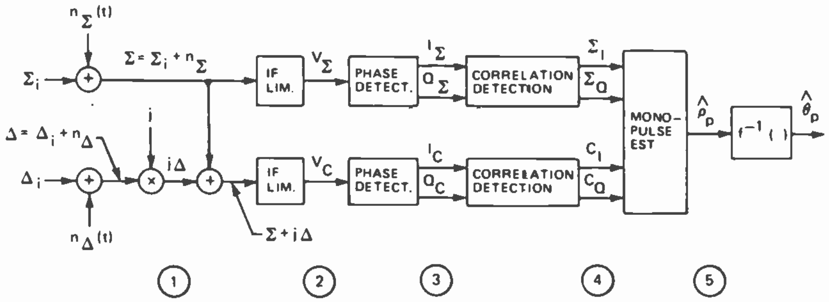

Fig. 2—Model for phase-only algorithm.

the signal band and with rms value σ_n.* The input signals Σ_i and Δ_i are modified by additive noise to give signals

$$\begin{aligned} \Sigma &= \Sigma_i + n_\Sigma = e_m P(t) g(\theta) e^{j\phi} + n_1(t) + jn_2(t) \\ \Delta &= \Delta_i + n_\Delta = e_m P(t) h(\theta) e^{j\phi} + n_3(t) + jn_4(t). \end{aligned} \qquad [5]$$

Then the signals at point 1 of Fig. 2 are Σ and $\Sigma + j\Delta$ where Σ and Δ are defined by Eqs. [5].

In the present analysis, we suppose that the signals are within the linear portion of the limiters (see Sec. 5.3) so that

$$\begin{aligned} v_\Sigma &= \Sigma \\ v_c &= \Sigma + j\Delta. \end{aligned} \qquad [6]$$

At point 3 of Fig. 2, we have

$$\begin{aligned} I_\Sigma &= \mathrm{Re}(v_\Sigma);\ Q_\Sigma = I_m(v_\Sigma) \\ I_c &= \mathrm{Re}(v_c);\ Q_c = I_m(v_c). \end{aligned} \qquad [7]$$

The correlation detector outputs at point 4 are then

$$\begin{aligned} \Sigma_I &= \int_0^T P(t) I_\Sigma(t) dt \cong \tau \sum_{i=1}^N P_i I_{\Sigma i} \\ \Sigma_Q &= \int_0^T P(t) Q_\Sigma(t) dt \cong \tau \sum_{i=1}^N P_i Q_{\Sigma i} \\ C_I &= \int_0^T P(t) I_c(t) dt \cong \tau \sum_{i=1}^N P_i I_{ci} \\ C_Q &= \int_0^T P(t) Q_c(t) dt \cong \tau \sum_{i=1}^N P_i Q_{ci},\ N = T/\tau. \end{aligned} \qquad [8]$$

Here T is the expanded pulse duration, τ is the compressed subpulse

---

* We denote the standard deviation of x by σ_x.

duration, and N is the code length. We assume that range has been accurately estimated so that the $P(t)$ in Eqs. [8] is in synchronism with the $P(t)$ in Eqs. [1].

Finally, the monopulse ratio $\rho = f(\theta)$ is estimated by $\hat{\rho}_p$,

$$\hat{\rho}_p = \tan\left[\tan^{-1}\left(\frac{C_Q}{C_I}\right) - \tan^{-1}\left(\frac{\sum_Q}{\sum_I}\right)\right]$$
$$= \frac{C_Q \sum_I - C_I \sum_Q}{C_I \sum_I + C_Q \sum_Q}. \qquad [9]$$

Here subscript p denotes the phase-only algorithm.

3.2 Model for the Conventional Monopulse Algorithm

For the conventional monopulse algorithm consider Fig. 3.* The inputs are given by Eqs. [1] while the noise terms are given by Eqs. [4]. The noise-corrupted inputs (signals at point 2 of Fig. 3) are given by Eqs. [5]. At point 3 of the figure, I_Σ, Q_Σ are as in Eqs. [7], while

$$I_\Delta = \mathrm{Re}(\Delta),\ Q_\Delta = I_m(\Delta). \qquad [10]$$

The outputs of the correlation detectors, point 4, are

$$\textstyle\sum_I = \int_0^T P(t) I_\Sigma(t)dt \cong \tau \sum_{i=1}^{N} P_i I_{\Sigma i}$$
$$\textstyle\sum_Q = \int_0^T P(t) Q_\Sigma(t)dt \cong \tau \sum_{i=1}^{N} P_i Q_{\Sigma i}$$
$$\Delta_I = \int_0^T P(t) I_\Delta(t)dt \cong \tau \sum_{i=1}^{N} P_i I_{\Delta i}$$
$$\Delta_Q = \int_0^T P(t) Q_\Delta(t)dt \cong \tau \sum_{i=1}^{N} P_i Q_{\Delta i} \qquad [11]$$

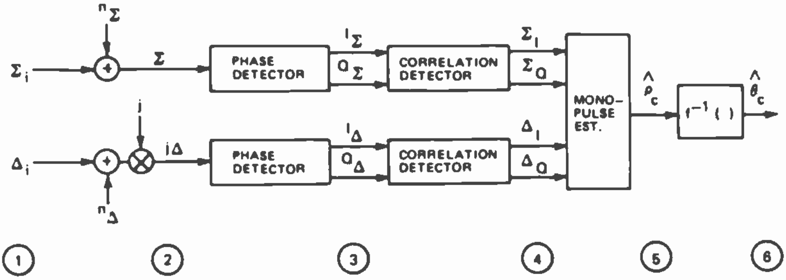

Fig. 3—Model for conventional monopulse.

---

* For notational consistency Δ is rotated 90° in Fig. 3.

where we use the same notations and assumptions as in Sec. 3.1.

The conventional monopulse estimator $\hat{\rho}_c$ of the monopulse ratio ρ is then

$$\hat{\rho}_c = \mathrm{Im}\left\{\frac{\Delta_I + j\Delta_Q}{\Sigma_I + j\,\Sigma_Q}\right\} = \frac{\Delta_Q\,\Sigma_I - \Delta_I\,\Sigma_Q}{\Sigma_I^2 + \Sigma_Q^2}. \qquad [12]$$

4. Analysis of Angle Estimation Errors

I this section, we derive convenient expressions for $\hat{\rho}_p$ and $\hat{\rho}_c$, the angle estimators for phase-only and conventional monopulse algorithms, respectively.

4.1 Analysis of $\hat{\rho}_p$

We define,

$$\begin{aligned} g_e &= e_m g(\theta) \\ h_e &= e_m h(\theta) = \rho g_e. \end{aligned} \qquad [13]$$

Then from Eqs. [4] through [7],

$$\begin{aligned} I_{\Sigma I} &= P_i g_e \cos\phi + n_{1i} \\ Q_{\Sigma i} &= P_i g_e \sin\phi + n_{2i} \\ I_{Ci} &= P_i(g_e \cos\phi - h_e \sin\phi) + n_{1i} - n_{4i} \\ Q_{Ci} &= P_i(g_e \sin\phi + h_e \cos\phi) + n_{2i} + n_{3i}. \end{aligned} \qquad [14]$$

Substituting Eqs. [14] into Eqs. [8] we obtain

$$\begin{aligned} \Sigma_I/\tau &= N g_e \cos\phi + Z_1 \\ \Sigma_Q/\tau &= N g_e \sin\phi + Z_2 \\ C_I/\tau &= N(g_e \cos\phi - h_e \sin\phi) + Z_5 \\ C_Q/\tau &= \mathrm{N}(\mathrm{g}_e \sin\phi + h_e \cos\phi) + Z_6. \end{aligned} \qquad [15]$$

Since the n_i's are independent, zero-mean, normally distributed random variables with variance σ_n^2, the Z_i in Eqs. [15] are also normally distributed with zero mean. In fact, we have

$$Z_1 = \sum_{i=1}^{N} P_i n_{1i}$$

$$Z_2 = \sum_{i=1}^{N} P_i n_{2i}$$

$$Z_5 = \sum_{i=1}^{N} P_i(n_{1i} - n_{4i})$$

$$Z_6 = \sum_{i=1}^{N} P_i(n_{2i} + n_{3i}),$$

from which it readily follows that

$$\begin{aligned}
&\mathrm{Var}(Z_1) = \mathrm{Var}(Z_2) = N\sigma_n^2 \\
&\mathrm{Var}(Z_5) = \mathrm{Var}(Z_6) = 2N\sigma_n^2 \\
&\mathrm{Cov}(Z_1, Z_2) = \mathrm{Cov}(Z_5, Z_6) = \mathrm{Cov}(Z_1, Z_6) = \mathrm{Cov}(Z_2, Z_5) = 0 \\
&\qquad \mathrm{Cov}(Z_1, Z_5) = \mathrm{Cov}(Z_2, Z_6) = N\sigma_n^2.
\end{aligned} \tag{16}$$

For convenience we introduce the random variables

$$\begin{aligned}
w_1 &= Z_1 \cos\phi + Z_2 \sin\phi \\
w_2 &= -Z_1 \sin\phi + Z_2 \cos\phi \\
w_5 &= Z_5 \cos\phi + Z_6 \sin\phi \\
w_6 &= -Z_5 \sin\phi + Z_6 \cos\phi,
\end{aligned} \tag{17}$$

so that

$$\begin{aligned}
Z_1 &= w_1 \cos\phi - w_2 \sin\phi \\
Z_2 &= w_1 \sin\phi + w_2 \cos\phi \\
Z_5 &= w_5 \cos\phi - w_6 \sin\phi \\
Z_6 &= w_5 \sin\phi + w_6 \cos\phi.
\end{aligned} \tag{18}$$

Then the w's are zero-mean gaussian random variables satisfying

$$\begin{aligned}
&\mathrm{Var}(w_1) = \mathrm{Var}(w_2) = N\sigma_n^2; \mathrm{Var}(w_5) = \mathrm{Var}(w_6) = 2N\sigma_n^2 \\
&\mathrm{Cov}(w_1, w_2) = \mathrm{Cov}(w_5, w_6) = 0 \\
&\mathrm{Cov}(w_1, w_5) = \mathrm{Cov}(w_2, w_6) = N\sigma_n^2 \\
&\mathrm{Cov}(w_1, w_6) = \mathrm{Cov}(w_2, w_5) = 0.
\end{aligned} \tag{19}$$

Combining Eqs. [19], [15] and [18], we get

$$\hat{\rho}_p = \frac{N^2 g_e h_e + N g_e(w_6 - w_2) + N h_e w_1 + w_1 w_6 - w_2 w_5}{N^2 g_e^2 + N g_e(w_1 + w_5) + N h_e w_2 + w_1 w_5 + w_2 w_6}. \tag{20}$$

Eq. [20], with minor modifications (see Eq. [26]) supplies the basis for a Monte Carlo analysis of error in $\hat{\rho}_p$. For an analytical approximation to the error in $\hat{\rho}_p$ we proceed as follows. We assume that

$$\sigma_n^2 \ll N^2 g_e^2, \tag{21}$$

which implies that

$$|w_1|, |w_2|, |w_5|, |w_6| \ll Ng_e. \qquad [22]$$

Then, dividing numerator and denominator of Eq. [20] by $N^2g_e^2$ and linearizing the result, we obtain

$$\hat{\rho}_p \cong \rho + \frac{1}{Ng_e}[w_6 - w_2 - \rho w_5 - \rho^2 w_2]. \qquad [23]$$

It follows that for Eqs. [21], [22] we have

$$\mathcal{E}(\hat{\rho}_p) \cong \rho$$

$$\mathrm{Var}(\hat{\rho}_p) \cong \frac{(1+\rho^2)^2}{\dfrac{2E}{N_0}} \qquad [24]$$

where $\mathcal{E}(X)$ denotes the expected value of X and

$$E = \frac{Ng_e^2\tau}{2} = \text{received energy}$$

$$N_0 = \sigma_n^2\tau = \text{one-sided noise power density}. \qquad [25]$$

Note that for the purposes of a Monte Carlo analysis, it is useful to rewrite Eq. [20] as

$$\hat{\rho}_p = \frac{2R\rho + \sqrt{2R}(X_6 - X_2) + \sqrt{2R}\rho X_1 + X_1X_6 - X_2X_5}{2R + \sqrt{2R}(X_1 + X_5) + \sqrt{2R}\rho X_2 + X_1X_5 + X_2X_6} \qquad [26]$$

where $X_i = w_i/(\sqrt{N}\sigma_n)$ $(i = 1, 2, 3, 4)$, $R = E/N_0$, and

$$\mathrm{Var}(X_1) = \mathrm{Var}(X_2) = 1$$

$$\mathrm{Var}(X_5) = \mathrm{Var}(X_6) = 2$$

$$\mathrm{Cov}(X_1, X_5) = \mathrm{Cov}(X_2, X_6) = 1$$

$$\mathrm{Cov}(X_1, X_2) = \mathrm{Cov}(X_1, X_6) = \mathrm{Cov}(X_2, X_5) = 0.$$

4.2 Analysis of $\hat{\rho}_c$

We present an abbreviated discussion, since the development parallels Sec. 4.1. From Eqs. [1], [4], and [10] we obtain $I_{\Sigma i}$ and $Q_{\Sigma i}$ as in Eqs. [14], as well as

$$I_{\Delta i} = -e_m h(\theta)P_i \sin\phi - n_{4i}$$

$$Q_{\Delta i} = e_m h(\theta)P_i \cos\phi + n_{3i}.$$

These equations imply (using Eqs. [11])

$$\textstyle\sum_I/\tau = Ng_e \cos\phi + Z_1$$

$$\sum_Q/\tau = Ng_e \sin\phi + Z_2$$
$$\Delta_I/\tau = -Nh_e \sin\phi - Z_4$$
$$\Delta_Q/\tau = Nh_e \cos\phi + Z_3,$$

where

$$Z_j = \sum_{i=1}^{N} P_i n_{ji},\ j = 1, 2, 3, 4.$$

Then the Z_j are independent, zero-mean, normally distributed with

$$\text{Var}(Z_j) = N\sigma_n^2,\ j = 1, 2, 3, 4.$$

Using the transformations in Eqs. [17] and [18], with the replacements

$$Z_5 \leftrightarrow Z_3$$
$$Z_6 \leftrightarrow Z_4,$$

we get

$$\hat{\rho}_c = \frac{N^2 h_e g_e + Nh_e w_1 + Ng_e w_3 + w_1 w_3 + w_2 w_4}{N^2 g_e^2 + 2Ng_e w_1 + w_1^2 + w_2^2}. \qquad [27]$$

In Eq. [27], w_1, w_2, w_3, w_4 are independent, zero-mean, normal random variables with variances

$$\text{Var}(w_i) = N\sigma_n^2,\ i = 1, 2, 3, 4. \qquad [28]$$

Eq. [27] may be put into the form

$$\hat{\rho}_c = \frac{2R\rho + \sqrt{2R}\rho X_1 + \sqrt{2R}X_3 + X_1 X_3 + X_2 X_4}{2R + 2\sqrt{2R}X_1 + X_1^2 + X_2^2}, \qquad [29]$$

where $R = E/N_0$ and $X_i = w_i/(\sqrt{N}\sigma_n)$ $(i = 1, 2, 3, 4)$, as before. The X_i are independent, zero-mean, normal random variables with unity variance. Eq. [29] is in a useful form for Monte Carlo.

For high signal-to-noise ratio, i.e., for $|X_i| \ll \sqrt{2R}$, we may linearize Eq. [29] to get

$$\hat{\rho}_c \cong \rho + \rho\frac{X_1}{\sqrt{2R}} + \frac{X_3}{\sqrt{2R}} - \frac{2\rho X_1}{\sqrt{2R}}. \qquad [30]$$

Hence, we have for this case,

$$\mathcal{E}(\hat{\rho}_c) \cong \rho$$
$$\text{Var}(\hat{\rho}_c) \cong \frac{(1 + \rho^2)}{2R}. \qquad [31]$$

Note that from Eqs. [31] and [24] we have

$$\frac{\text{Var}(\hat{\rho}_c)}{\text{Var}(\hat{\rho}_p)} = \frac{1}{1 + \rho^2} \leq 1 \left(\frac{E}{N_0} \gg 1\right). \qquad [32]$$

In particular, for high E/N_0 and for $\rho = 0$, we have $\mathrm{Var}(\hat{\rho}_p) = \mathrm{Var}(\hat{\rho}_c)$.

5. Numerical Results

Some numerical results that are independent of monopulse slope are given in Table 1. In addition, in this section, we present data in terms of angle errors for a typical narrow beam antenna. The results of Sections 5.1 and 5.2 assume no i-f limiting. Sec. 5.3 gives a brief discussion of the effects of hard limiting on $\hat{\rho}_p$.

In order to justify the values of ρ treated below, let us consider Fig. 4. This gives a specific example of sum and difference patterns together with a corresponding monopulse curve (ρ versus θ) in terms of the ratio θ/θ_0 where θ_0 is one-half the 3-dB beamwidth. Note that ρ can assume values larger than 1. For a target in track, the values of ρ will generally be small ($|\rho| \ll 1$). On the other hand, in the acquisition of a designated target, the values of ρ may be greater than 1. The instrumented values of ρ in a radar will depend on the application.

Table 1—Comparison of Monte Carlo and Analytic Results for σ_{ρ_p} with $\rho_{max} = 2.0$.

E/N_0 (dB)	σ_{ρ_p} (Monte Carlo)/σ_{ρ_p} (Linearized)		
	$\rho = 0$	$\rho = 0.4$	$\rho = 0.8$
10	1.20	1.24	1.24
12	1.11	1.23	1.22
14	1.06	1.14	1.21
16	1.04	1.10	1.13
18	1.03	1.07	1.09
20	1.02	1.06	1.07
22	1.02	1.05	1.05
24	1.02	1.04	1.04
26	1.02	1.04	1.04
28	1.01	1.04	1.03
30	1.01	1.04	1.03

5.1 Approximate Analytical Results

The approximations to $\mathrm{Var}(\hat{\rho}_p)$ and $\mathrm{Var}(\hat{\rho}_c)$ (Relations [24] and [31]) are very simple and lead directly to the antenna-independent data shown in Fig. 5. All of the data are for high or moderate signal-to-noise ratio (E/N_0) for which Eqs. [24] and [31] are approximately valid (see Sec. 5.2).

From Fig. 5, one sees that the loss of the phase-only algorithm relative to conventional monopulse varies from 0 dB for $\rho = 0$ to 3.0 dB for $\rho = 1.0$. This is made more precise in Fig. 6 which gives this loss as a function of ρ. For tracking, $|\rho| \ll 1$ so that the loss is small. For acquisition of a

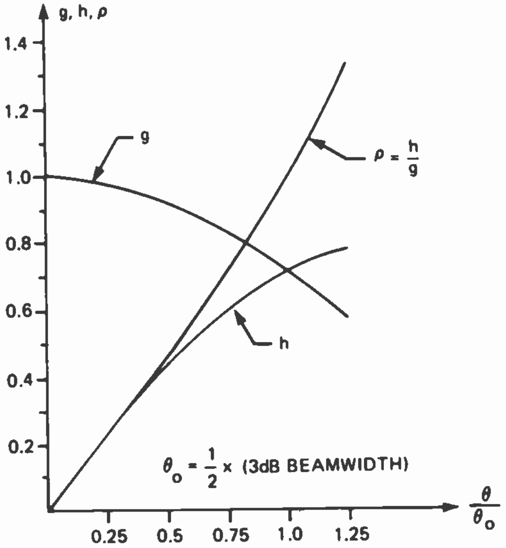

Fig. 4—Example of sum (g) and difference (h) voltage patterns and monopulse curve (ρ).

target whose position is only approximately known, $|\rho|$ can be near 1 with a corresponding loss of $\hat{\rho}_p$ relative to $\hat{\rho}_c$ of about 3 dB.

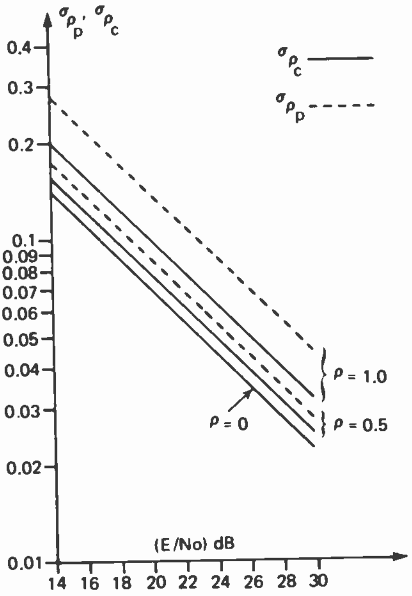

Fig. 5—Values of σ_{ρ_c} and σ_{ρ_p} from linearized analysis.

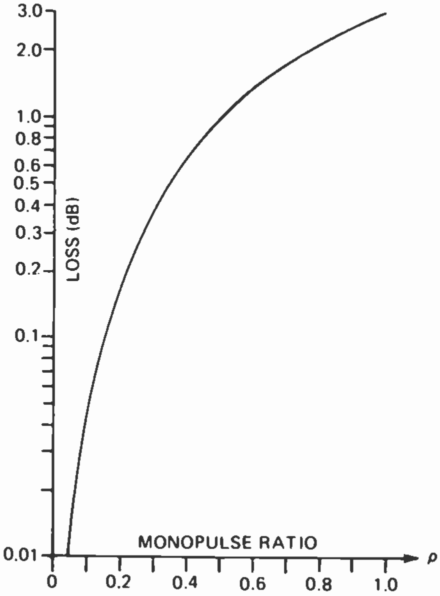

Fig. 6—Loss of $\hat{\rho}_p$ relative to $\hat{\rho}_c$ (in dB) for $E/N_0 \geq 14$ dB.

5.2 Monte Carlo Results

A Monte Carlo analysis is useful in two respects. It determines the region of validity of the approximate, linearized analysis of Sec. 4. In addition, for low values of E/N_0, which may occur in the event of fading, the results of Sec. 4 are no longer valid and indeed tend to be optimistic.

Monte Carlo results on angle estimation error can be based upon Eqs. [26] and [29], provided some modifications are made. The problem is that in Eqs. [26] and [29], we have the quotient of two random variables with the denominator assuming arbitrary small values and the quotient assuming arbitrarily large values. The situation is very similar to that of the quotient of two normal random variables. It is well known[1] that the quotient of two gaussian random variables has neither mean nor variance. Similarly, if we apply Monte Carlo to Eqs. [26] or [29] to find moments of the errors, we do not get convergence. We must, therefore, take note of the fact that, in practice, our estimates $\hat{\rho}_p$, $\hat{\rho}_c$ must be limited, e.g., by the finite size of storage registers. As a result, we must apply Monte Carlo not to the $\hat{\rho}_p$, $\hat{\rho}_c$ given above, but to limited values $\hat{\rho}_{pL}$, $\hat{\rho}_{cL}$ defined as:

$$\begin{aligned} \hat{\rho}_{pL} &= \hat{\rho}_p, \text{ if } |\hat{\rho}_p| \leq \rho_{max}, \\ &= \rho_{max} \cdot \operatorname{sgn}(\hat{\rho}_p) \text{ otherwise;} \end{aligned} \qquad [33]$$

$$\hat{\rho}_{cL} = \hat{\rho}_c, \text{ if } |\hat{\rho}_c| \leq \rho_{max}, \\ = \rho_{max} \cdot \text{sgn}(\hat{\rho}_c) \text{ otherwise.} \qquad [34]$$

Here ρ_{max} is the largest magnitude of $\hat{\rho}_p$ or $\hat{\rho}_c$ that is computed or stored.

The introduction of Eqs. [33] and [34] makes our results moderately dependent upon the magnitude of ρ_{max}.

In Table 1, we compare Monte Carlo data with the analytic expressions given for σ_{ρ_p}. The Monte Carlo results are based on the value $\rho_{max} = 2.0$. Note that for $E/N_0 \geq 14$ dB, the analytical approximation is quite good. Observe also that the linear approximation consistently underestimates σ_{ρ_p}. Analogous results have been obtained for σ_{ρ_c}.

5.3 The Effects of Limiting on the Phase-Only Algorithm

A complete examination of the effects of limiting is tedious. However, we have evaluated the special case of hard limiting at i-f for the monopulse curve treated in Sec. 5.2. The results are given in Table 2 as a function of the signal to noise ratio (S/N) at i-f.

Table 2—Loss of Hard IF Limiting Relative to No Limiting.

S/N (dB) at IF	Loss in dB
−20	2
−10	2
0	2
10	0.8
20	0.0

5.4 An Alternative Procedure for Estimating σ_ρ

In the above, we have obtained estimates of σ_ρ (1) by linearizing the expressions for $\hat{\rho}_p$ and $\hat{\rho}_c$ and (2) by using the Monte Carlo technique. An alternative procedure is to start from the expressions for $\hat{\rho} = U/V$, obtain the probability density functions of numerator (U) and denominator (V) of $\hat{\rho}$, and then apply the methods outlined by C. C. Craig[1] to obtain the probability density function of the quotient (U/V). It is then an easy matter to get the probability density functions of $\hat{\rho}_{pL}$, $\hat{\rho}_{cL}$ defined by Eqs. [33] and [34], respectively. Evaluation of σ_{ρ_p}, σ_{ρ_c} is then made by numerical integration. Conceptually, and numerically, the Monte Carlo method is simpler.

6. Conclusions

It has been shown that in the absence of limiting, the phase-only and the conventional monopulse algorithms give essentially identical results for $E/N_0 \geq 14$ dB. With hard i-f limiting, however, the conventional monopulse cannot operate, while the phase-only algorithm suffers a loss relative to linear operation of 2 dB or less.

References:

[1] C. C. Craig, "On Frequency Distributions of the Quotient and of the Product of Two Statistical Variables," *Amer. Math. Monthly*, **49**, pp. 24–32 (1942).

Ion Implantation of Sulfur and Silicon in GaAs*

S. G. Liu, E. C. Douglas, C. P. Wu, C. W. Magee, S. Y. Narayan, S. T. Jolly, F. Kolondra, and S. Jain

RCA Laboratories, Princeton, NJ 08540

Abstract—This paper describes implantation of ^{28}Si and ^{32}S into semi-insulating GaAs to generate high mobility n layers. Implantation of ^{28}Si over an energy range of 40 keV to 1.2 MeV and fluence ranging from 10^{12} to 10^{16} cm^{-2} was studied. Implanted layers were characterized by secondary ion mass spectrometry (SIMS), differential Van der Pauw measurements, and differential CV measurements. A capless thermal annealing technique under arsenic overpressure that results in high activation efficiency and excellent surface morphology was developed. Implanted n-layers as deep as 1 μm have been realized.

The activation efficiency varies between 40 and 90% in the dose range between 3×10^{12} and 5×10^{13} cm^{-2} (implant energy 200 keV) and decreases toward the high-dose level. A threshold fluence was observed below which the implanted layer was no longer activated. This "cut off" dose depends on the substrate characteristics and is typically 2×10^{12} cm^{-2} for 200 keV implant. Typical mobilities at an electron density of $1\text{–}2 \times 10^{17}$ cm^{-3} were 3500–4000 cm^2/V-s. High dose ($\gtrsim 1 \times 10^{14}$ cm^{-2}) Si-implanted semi-insulating GaAs after irradiation with either a *Q*-switched ruby laser or a Nd:Glass laser show higher sheet electron concentration but lower mobility than thermally annealed samples.

The measured depth distribution of electron concentration is broader for S-implanted than for Si-implanted GaAs as a result of thermal diffusion during annealing. The diffusion coefficients at 825°C for S and Si in GaAs were deduced from electron density profiles to be $2\text{–}5 \times 10^{-14}$ and $\leq 10^{-15}$ cm^2/s, respectively. The redistribution of the implanted Si following thermal or laser annealing was studied using SIMS. Preliminary results on redistribution of Cr in the semi-insulating GaAs due to implantation and annealing are also presented.

---

* This program was supported in part by the Office of Naval Research under Contract No. N00014-78-C-0367 and Defense Advanced Research Project Agency under Contract No. 00014-77-C-0542.

1. Introduction

This paper describes the implantation of ^{28}Si and ^{32}S into semi-insulating (SI) GaAs substrates to generate uniformly-doped high-mobility n-layers. The activation of implanted donor atoms by thermal and pulsed laser annealing is also described. The characterization of the implanted layers by secondary ion mass spectrometry (SIMS), differential Van der Pauw measurements, and differential *CV* measurements is also discussed. The significant achievements of this research are the first reported realization of implanted layers of 1 μm thickness by using implant energies as high as 1.2 MeV and the development of a capless thermal annealing process under arsenic over-pressure that results in high activation efficiency with excellent surface morphology.

Preliminary results show that laser annealing is more efficient than thermal annealing for high dose ($>10^{14}$ cm^{-2}) implanted samples. The low sheet resistance layers obtained by laser annealing are particularly suitable for ohmic contact regions in discrete microwave devices like GaAs power field-effect transistors (FETs) and multigigabit-rate GaAs integrated circuits. It was observed, furthermore, that the redistribution of Cr from the Cr-doped semi-insulating (SI) GaAs substrate is substantially lower for laser annealed than for thermally-annealed, high-dose implanted samples.

2. Substrates

Chromium-doped SI (100)-oriented GaAs substrates were used in our ion-implantation experiments. Studies were also made of implantation into vapor-phase grown, high-resistivity epitaxial layers. Semi-insulating substrates obtained from various sources were evaluated. Ion-implantation results depend strongly on the quality of the substrate material. Some SI GaAs substrates convert to either p-type or n-type following high-temperature annealing even in the absence of implanted ions. Substrate qualification is therefore mandatory prior to implantation. Our normal qualification test consists of implanting the sample with argon or krypton, then annealing at, typically, 800 to 950°C for 15 to 30 minutes. A qualified semi-insulating substrate does not convert after annealing.

Before ion implantation the SI substrates are carefully cleaned and etched to produce a damage-free surface. The wafers are cleaned in organic solvents followed by DI-water rinsing and a 5- to 10-min etch in a solution of H_2SO_4:H_2O_2:H_2O in the ratio of 4:1:1. The wafers are then rinsed in DI-water ($\geq$14 MΩ) and spun dry. Etching is done in a tilted rotating beaker to obtain a uniformly etched surface. The layer removed is approximately 3–6 μm. When implantation through a dielectric layer is required, the wafer surface is coated with either a chemical-vapor-deposited SiO_2 layer or a reactively sputtered Si_3N_4 layer. This layer thickness is typically 500–700Å.

3. Ion Implantation of $^{28}Si^+$ and $^{32}S^+$ Into GaAs

Low-energy (<300 keV) ion-implantation experiments were performed in the 300-keV machine at RCA Laboratories. Silane (SiH_4) was used as the source gas in the rf ion source for Si implantation, while solid sulfur or H_2S was used for S implantation. The beam current during Si implantation is typically 0.1 μA for low-dose ($10^{12}-10^{13}$ cm^{-2}) and up to 10 μA for high-dose (10^{15} cm^{-2}) implants. A typical implantation at 200 keV with a dose of 1×10^{14} cm^{-2} and a beam current of 10 μA takes about 1 min. The maximum beam current level attainable for S implantation at 200 keV is about 5 μA. Implantation was studied at room temperature with fluences between 1×10^{12} and 5×10^{15} cm^{-2}, and energies between 40 and 280 keV.

High-energy (>500 keV) implantations were performed using a 3-MeV Van de Graaff machine.* Silane (SiH_4) was used as the source gas in the ion source for Si implantation. The implantation energy ranged from 500 to 1200 keV. During implants the normal to the wafer was inclined at an angle of 7° to the incident beam. High energy implant experiments were done only with ^{28}Si.

4. Thermal Annealing

One of the major problems of ion implantation into GaAs is that the material begins to dissociate at the commonly used anneal temperatures (800–1000°C). To prevent problems caused by dissociation, it is common practice to use an encapsulant such as SiO_2,[1] Si_3N_4,[2] Al_2O_3,[3] AlN,[4] the combination of SiO_2 and Si_3N_4,[5] or aluminum.[6] We have developed an operationally simple capless annealing process that results in high activation efficiency with good surface morphology even for implants up to 1 MeV.

Capless anneal is done at a temperature between 800 and 900°C under arsenic overpressure in an open quartz tube. The arsenic overpressure at 850°C is maintained by using a flow of 75 ml of 7.5% AsH_3 in 2 liters of H_2. Under this condition the arsenic overpressure at 850°C is over two orders of magnitude higher than the equilibrium partial pressure.[7] The arsenic overpressure prevents decomposition of GaAs and results in

---

* Located at Fusion Energy Corp., Princeton, NJ.

excellent surface morphology. A higher AsH_3 flow is used at 900°C to obtain the same overpressure.

Anneal experiments were also performed on wafers encapsulated with a Si_3N_4 layer. A typical Si_3N_4 thickness was 2000–3000 Å, and annealing was done in a N_2 atmosphere. Both plasma-deposited Si_3N_4 layers and reactive-sputtered Si_3N_4 layers were tested. The plasma Si_3N_4 encapsulated samples showed blisters following an 850°C 30-min anneal; samples encapsulated with high quality sputtered Si_3N_4 showed no blistering up to 1000°C, and implanted layers were activated with good surface morphology.

5. Laser Annealing

We also studied annealing of Si-implanted GaAs using high-power pulsed Nd:Glass ($\lambda = 1.06$ μm sub-bandgap energy) and ruby ($\lambda = 0.694$ μm-higher-than-bandgap energy) lasers. The laser system used was the Korad Model K-1500 gigawatt laser system.* This consists of an oscillator, amplifier, and a Pockel cell for Q-switching the oscillator output. Maximum output power is 1 GW/pulse at 2 pulse/min. The output pulse width was measured with a photodiode and a fast response oscilloscope. The optimum pulse shape recorded has a Gaussian distribution with a FWHM of 25 ns. The same laser system was modified for Nd:Glass laser experiments by replacing the laser rods and associated optics. The laser output pulse energy density was measured with a calibrated (±5%) ballistic thermopile. The laser output energy per pulse is adjusted by varying the high voltage on the xenon lamps around the amplifier stage and/or the oscillator stage.

6. Results

6.1 Thermally Annealed-Low Energy (<300 keV) Implanted Layers

Following implantation and annealing, the electrically active layer was characterized by Van der Pauw measurements[8] to determine the Hall mobility, sheet carrier concentration, conductivity, and activation efficiency and by C-V measurements to determine the depth profile of the electrically activated donors. Characteristics of the low-energy (<300 keV) Si- and S-implanted GaAs wafers are described below.

(a) Mobility, Carrier Concentration, and Activation Efficiency

The Hall mobility and sheet carrier concentration of the electrically activated ion-implanted layer were measured by the Van der Pauw

---

* Hadron, Inc., Korad Div. Santa Monica, CA.

method.[8] A square or a clover-shaped mesa sample with four ohmic contacts at the corners was used. Typical sample dimensions were 7 × 7 to 10 ×10 mm. The Hall mobility is given by

$$\mu_H = \frac{R_S}{\rho_s} \qquad [1]$$

where R_S is the Hall coefficient and ρ_s is the sheet resistance. The Hall coefficient is given by

$$R_S = 10^8 \frac{\Delta V_{24}}{BI_{13}} \qquad [2]$$

where I_{13} is the current, B is the magnetic flux density applied perpendicular to the surface of the sample, and ΔV_{24} is the voltage change with and without the magnetic field. The subscripts correspond to the four ohmic contacts, which are numbered in sequence. The sheet resistance ρ_s is given by

$$\rho_s = \frac{\pi}{2 \ln 2}\left(\frac{V_{34}}{I_{12}} + \frac{V_{23}}{I_{41}}\right) \cdot F, \qquad [3]$$

where F is a geometrical correction factor. A relation between F and the ratio (V_{34}/I_{12}) to (V_{23}/I_{41}) is given in Ref. [8]. From Eq. [1], the sheet carrier concentration N_S is

$$N_S = \frac{1}{qR_S}, \qquad [4]$$

where q is the electronic charge (1.6×10^{-19}C).

The activation efficiency for an implanted and annealed sample is given by

$$\eta = \frac{N_S}{N'_S} \qquad [5]$$

where N'_S is the fluence used.

Table 1 shows results on ^{32}S implantation into SI GaAs substrates and into substrates with a high resistivity buffer layer grown by vapor phase epitaxy. The implantations listed are for an energy of 200 keV and fluences between 4×10^{12} and 5×10^{14} cm^{-2}. Table 2 lists results on Si-implanted samples. All samples were annealed at 825°C for 20 min using the capless process. Mobility values are in the 3000 to 4300 cm^2/V-s range, and activation efficiencies are in the 50 to 90% range for implants with fluences between 3×10^{12} and 2×10^{13} cm^{-2}.

The lower activation occurring in high-dose implanted samples is believed to be due to the solid solubility limit at the annealing temperature. *The mobilities are generally higher (≳4000 cm^2/V-s) for im-*

Table I—S Implantation in GaAs.

Sample Number	Substrate	Energy (keV)	Dose (cm^{-2})	Mobility (cm^2/V-s)	Approx. Carrier Conc. (cm^{-3})	Activation Eff. (%)
62B	SI (MMG103)	200	4.0×10^{12}	3320	8.4×10^{16}	41.8
63B	Cr-n$^-$/SI* (A-141)	200	5.0×10^{12}	4050	1.8×10^{17}	72.4
10A	SI (LD)	200	5.0×10^{12}	3220	1.8×10^{17}	73.6
10D	(5-μm)n$^-$/SI*	200	5.0×10^{12}	4010	1.7×10^{17}	67.2
45A	(3-μm)n$^-$/SI* (C265)	250	7.0×10^{12}	4360	1.4×10^{17}	40.9
45E	SI (MX)	250	7.0×10^{12}	4070	1.5×10^{17}	46.9
45F	(10-μm)Cr-n$^-$/SI* (A90)	250	7.0×10^{12}	4330	1.2×10^{17}	37.1
19X	SI (LD)	200	7.0×10^{13}	3220	3.7×10^{17}	73.0
14C	SI (LD)	200	1.5×10^{13}	3230	2.5×10^{17}	32.8
64A	SI (MMG102)	200	2.0×10^{13}	2900	5.8×10^{17}	58.3
57	SI (XS3761)	200	1.0×10^{14}	3200	1.5×10^{18}	30.6
50A	SI (XS3761F)	200	5.0×10^{14}	2890	1.7×10^{18}	6.7

* Vapor-phase high-resistivity epitaxial layer grown on SI substrate.

plantation into a high-quality, high-resistivity epitaxial buffer layer grown on a SI GaAs substrate, as shown in Tables 1 and 2. A direct implant into some substrates (e.g., sample A26) also results in electron mobility of higher than 4000 cm^2/V-s at 1–2 × 10^{17} cm^{-3} doping density.

The carrier concentration values in Tables 1 and 2 were approximately determined using

$$N_m = \frac{N_S}{\sqrt{2\pi}\,\Delta R_P}. \qquad [6]$$

This expression is an approximation to the Gaussian distribution

$$N_S = \int_0^\infty N(x,E)dx = \sqrt{\frac{\pi}{2}}\,N_m\,\Delta R_P \times \left[1 + \left(\operatorname{erf}\frac{R_P}{\sqrt{2}\Delta R_P}\right)\right], \qquad [7]$$

where R_P and ΔR_P are the projected range and standard deviation, respectively. The measured sheet electron concentration values were used for N_S in Eq. [6], and the ΔR_P was taken as 0.08 μm at the 200-keV energy level. This value of ΔR_P is close to that measured by SIMS. Table 3 lists computed data using the electronic stopping powers compiled by

Table 2—Si Implantation in GaAs.

Sample Number	Substrate	Energy (keV)	Dose (cm^{-2})	Mobility (cm^2/V-s)	Approx. Carrier Conc. (cm^{-3})	Activation Eff. (%)
A24A	6-μm n$^-$/SI* (D95)	200	3.0×10^{12}	4290	8.2×10^{16}	54.9
A35A	SI (XS3761)	200 70	3.0×10^{12} 1.5×10^{12}	3370	1.9×10^{17}	82.6
A35C	SI (XS3765F)	200 70	3.0×10^{12} 1.5×10^{12}	3630	1.7×10^{17}	76.8
A35D	5-μm n$^-$/SI* (D143)	200 70	3.0×10^{12} 1.5×10^{12}	4000	1.9×10^{17}	85.1
A28N	SI (XS3761F)	200	3.5×10^{12}	3740	1.6×10^{17}	90.3
A23A	Cr-n$^-$/SI* (A156)	200	4.0×10^{12}	3930	1.2×10^{17}	60.5
A3A	SI (MMG102)	200	4.0×10^{12}	3570	1.2×10^{17}	62.0
A26	SI (XS3765)	200 50	4.0×10^{12} 2.0×10^{12}	4000	1.5×10^{17}	60.5
A4B	SI (XS3761)	200	6.0×10^{12}	3220	1.9×10^{17}	64.7
A31	SI (XS3761)	200	2.0×10^{13}	2930	7.0×10^{17}	70.1
A6	SI (MMG102)	200	5.0×10^{13}	2050	1.1×10^{18}	37.0
A34	SI (XS3761F)	200	1.0×10^{14}	2200	1.1×10^{18}	21.5
A44	SI (XS3761F)	70	1.0×10^{15}	1770	1.6×10^{18}	3.2

* Vapor-phase high-resistivity epitaxial layer grown on SI substrate.

Northcliffe and Schilling[9] instead of values predicted by LSS theory.[10]

The mobility versus carrier concentration data for S- and Si-implanted samples are shown in Figs. 1 and 2, respectively. Theoretical curves of drift mobility with compensation ratio as parameter are also included.[11] Most of the experimental points are located between a compensation ratio of 1 and 2, indicating acceptable material quality.

Experimental carrier concentration data (electrically activated) as function of implantation dose are shown in Figs. 3(a) and 3(b) for S and Si implantation, respectively, into GaAs. The samples were capless-annealed at a temperature of 825°C for 20 min. The implantation energy was 200 keV for all data points. Data-point scattering for different substrates is apparent. Both the Si- and S-implantation data indicate that (1) the carrier concentration varies almost linearly with fluence for fluences between 5×10^{12} and 3×10^{13} cm^{-2} for S implant and between 2.5×10^{12} and 2×10^{13} cm^{-2} for Si implant and (2) free carrier concentration increases at a much slower rate at high fluence. *We will show later that higher activation at high doses can be obtained by laser annealing.* Similar saturation effects for Se and S implantation have been reported by Donnelly.[12] The data also show that no electrical activation was

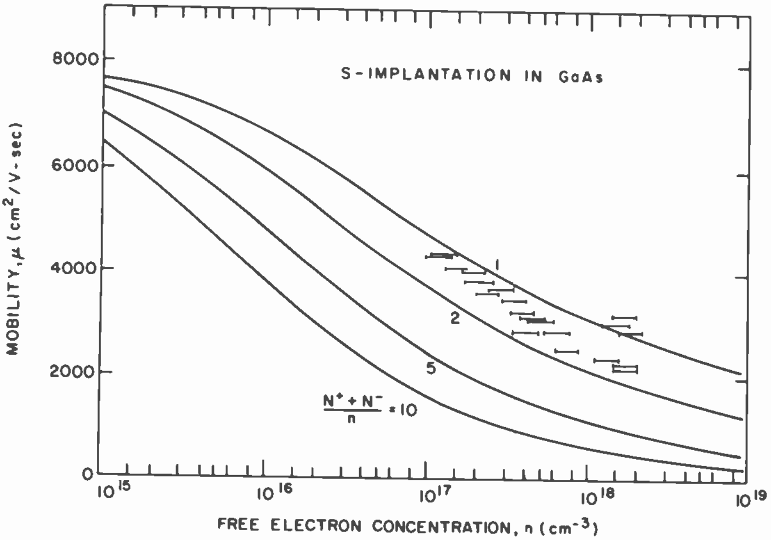

Fig. 1—Mobility versus carrier concentration for S implanted in GaAs.

achieved at fluences lower than about 10^{12} cm^{-2} (200 keV). This "cut-off" threshold varies with substrate quality. This cut-off behavior is not fully understood.

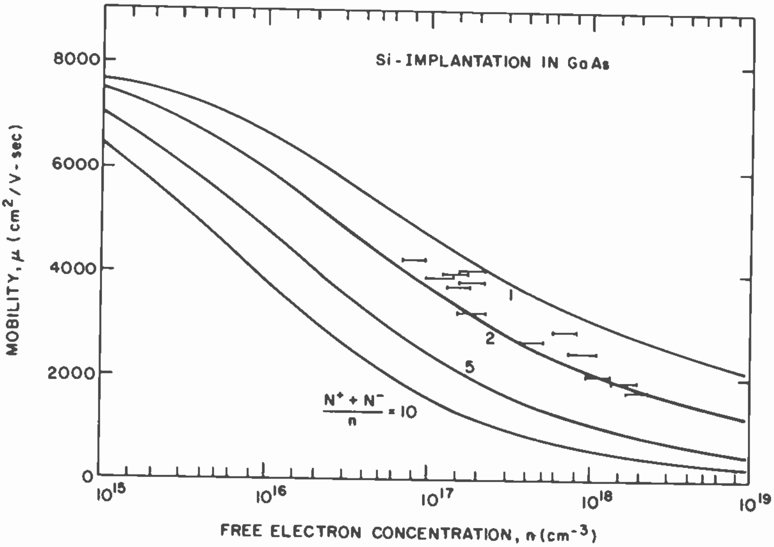

Fig. 2—Mobility versus carrier concentration for Si implanted in GaAs.

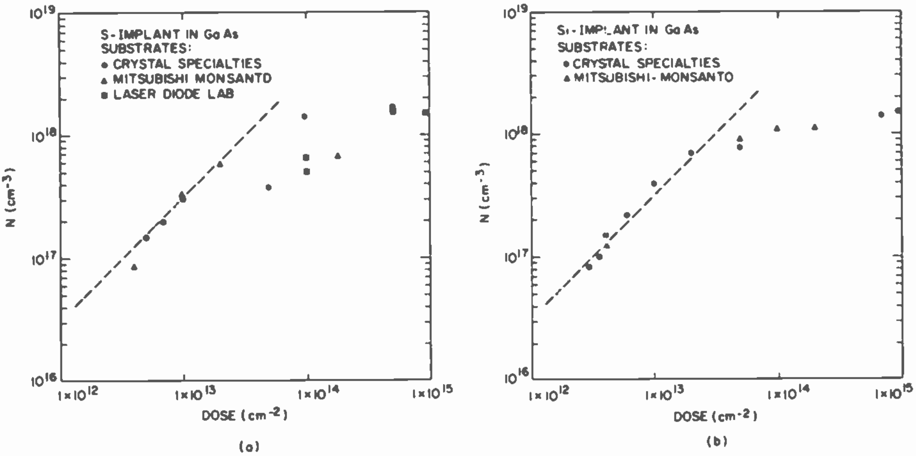

Fig. 3—Carrier concentration as a function of implantation dose (a) for S implantation and (b) for Si implantation into GaAs.

(b) Electrical Conductivity of Ion-Implantation Created Disordered Layer

The surface of an as-implanted SI GaAs substrate shows electrical conduction due to lattice disorder. The sheet conductivity is a function of implantation dose. This phenomenon has been discussed by Y. Kato, et al.[13] The sheet resistance of as-implanted GaAs was measured by a four-point probe. Ohmic characteristics were obtained with probes on as-implanted GaAs surfaces. Figs. 4(a) and (b) show the variation of sheet

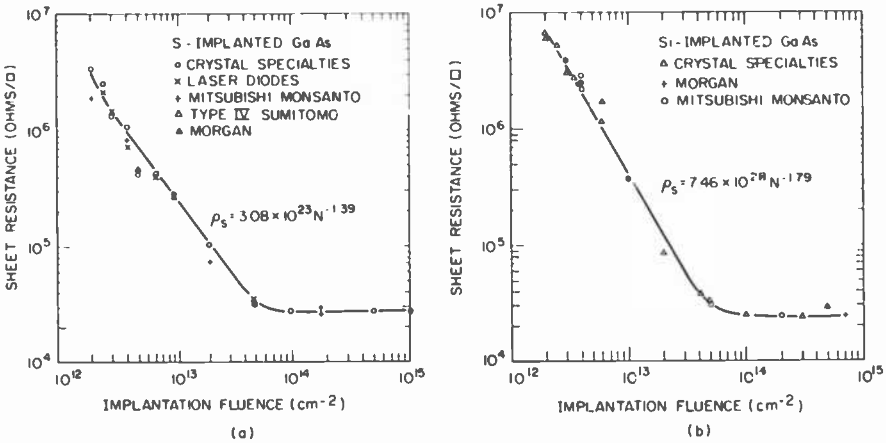

Fig. 4—Sheet resistance versus implant dose measured (a) on S implanted and (b) on Si implanted unannealed GaAs.

resistance with dose for S and Si implants into a number of SI GaAs substrates. In the dose range of 2×10^{12} to 3×10^{13} cm^{-2}, the sheet resistance decreases with increasing dose approximately as

$$\rho_S = 3.08 \times 10^{23} \times N^{-1.39} \quad [8]$$

for S implantation, and

$$\rho_S = 7.46 \times 10^{28} N^{-1.79} \quad [9]$$

for Si implantation.

Above 5×10^{13} cm^{-2} fluence, electrical conductivity begins to saturate. A reduction in conductivity is observed as the dose increases beyond 10^{15} cm^{-2}. These features are in general agreement with Kato, but the exponent dependence of ρ_S on N given by Eqs. [8] and [9] is considerably less steep (-1.39 and -1.79 versus -3).

Note the qualitative correlations between the electrical conductivity of disordered layer following implantation as shown in Figs. 4(a) and (b), the electrically active sheet carrier concentration following annealing, as shown in Figs. 3(a) and (b). Both sets of figures show a knee at a dose of about 5×10^{13} cm^{-2} and an exponentially related region between about 2×10^{12} and 3×10^{13} cm^{-2}. The conductivity of as-implanted layers can be used to conveniently monitor implantation before annealing.

(c) Depth Distribution of Electron Concentration

The electron concentration was measured by the well known technique of making *CV* measurements on a Schottky diode defined on the implanted layer.[14] The accuracy of the *CV* technique is inherently limited in reproducing a shallow electron density profile with a steep doping

Table 3—Range and Straggle Statistics for ^{32}S and ^{28}Si Ions Implanted Into GaAs.

	S in GaAs			Si in GaAs	
Energy (keV)	R_P (μm)	ΔR_P (μm)	Energy (keV)	R_P (μm)	ΔR_P (μm)
10	0.0102	0.0078	10	0.0111	0.0105
50	0.0395	0.0194	50	0.0441	0.0221
70	0.0537	0.0252	70	0.0605	0.0288
100	0.0758	0.0337	100	0.0861	0.0383
120	0.0908	0.0390	120	0.1033	0.0442
150	0.1135	0.0465	150	0.1291	0.0523
200	0.1515	0.0578	200	0.1723	0.0646
260	0.1973	0.0702	260	0.2242	0.0778
300	0.2279	0.0778	300	0.2582	0.0855
400	0.3029	0.0942	400	0.3421	0.1024
600	0.4506	0.1213	600	0.5053	0.1296
800	0.5919	0.1423	800	0.6549	0.1488
1000	0.7219	0.1580	1000	0.7941	0.1638

density variation.[15] The inaccuracy occurs particularly close to the surface and toward the tail end. For most implantations performed, the ratio of $R_P/\Delta R_P$ is about 2 (Table 3), which means a less steep variation in doping densities than for implantations into silicon. The CV technique thus provides information around the peak of the depth distribution.

Fig. 5(a) shows the carrier concentration density profile of a Si-implanted sample. The implantation dose and energy level are 3.5×10^{12} cm^{-2} and 200 keV, respectively. Fig. 5(b) shows the carrier-concentration density profile of a multiple Si-implanted sample. The dose and energy levels are 3×10^{12} cm^{-2} at 200 keV, and 1×10^{12} cm^{-2} at 70 keV. These values were chosen to yield a nearly constant doping distribution. Fig. 5(b) demonstrates that the doping profile can be controlled by multiple implants.

The measured electron distribution of S-implanted GaAs was found to be broader than for similar Si-implanted samples and deviates from a Gaussian distribution. This is attributed to significant diffusion during anneal. Fig. 6 shows a measured curve with circles indicating the computed LSS distribution, including thermal diffusion, normalized to match the measured peak. The diffusion coefficient, D, corresponding

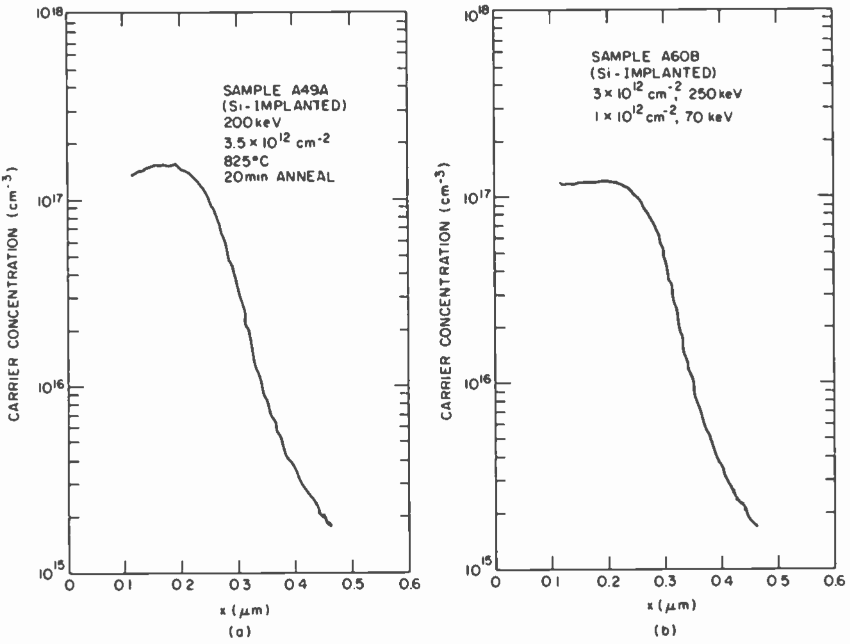

Fig. 5—Carrier concentration profile (a) for single-energy Si implant and (b) for dual Si implant.

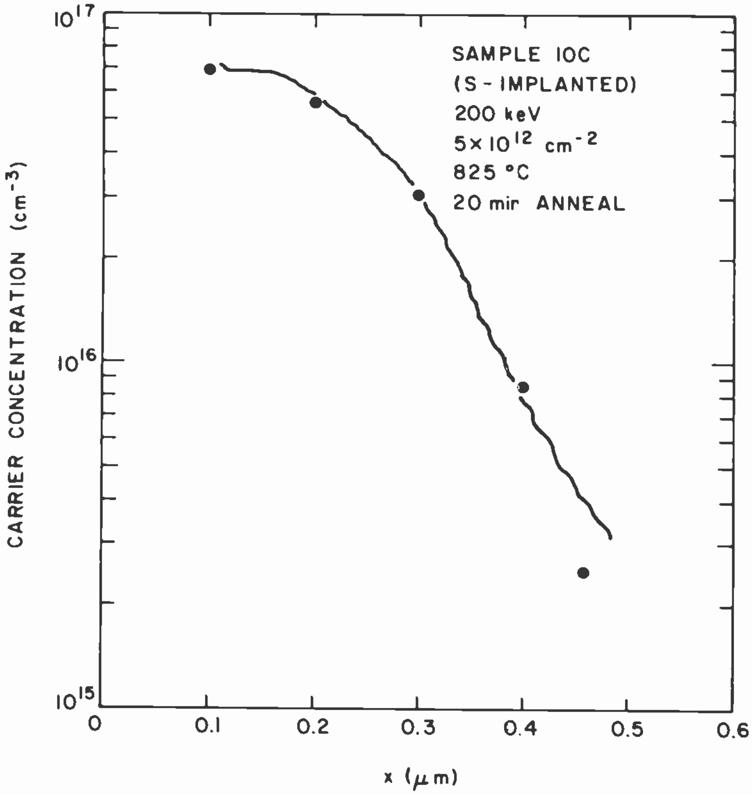

Fig. 6—Measured electron density distribution of S implanted GaAs.

to the 825°C anneal temperature was deduced to be 5×10^{-14} cm^2/s. Similar measurements on a number of samples show values of D between 2×10^{-14} and 5×10^{-14} cm^2/s at 825°C. This compares favorably with that measured by Young and Pearson[16] and by Asai and Kodera[17] but is almost an order of magnitude lower than Kendall's result.[18] A similar match to LSS distribution was made for the measured profile on Si-implanted GaAs samples and the diffusion coefficient was found to be $\leq 10^{-15}$ cm^2/s.

(d) Electron Concentration and Hall Mobility Profile

The depth distribution of carrier concentration and mobility on some samples were determined by Van der Pauw measurements in conjunction with controlled layer removal.

The mobility, μ, and carrier concentration density, n, corresponding to the ith chemically removed GaAs layer are given respectively by[19,20]

$$\mu_i = \frac{(R_S/\rho_s^2)_{i-1} - (R_S/\rho_s^2)_i}{(1/\rho_s)_{i-1} - (1/\rho_s)_i} \qquad [10]$$

$$n_i = \frac{(1/\rho_s)_{i-1} - (1/\rho_s)_i}{q h_i \mu_i} \qquad [11]$$

where ρ_s is the sheet resistivity, R_S is the sheet Hall coefficient, h the thickness of the chemically removed layer, q the electrical charge, and the lower case index i and $i - 1$ refer to the successive order of removed layers. The sheet resistivity ρ_s and Hall coefficient R_S are given, respectively, by Eqs. [3] and [2].

Fig. 7 shows the carrier concentration and mobility profile of a S-implanted sample (49B). This sample was implanted with a dose of 10^{13} cm^{-2} at 200 keV. Post-implant annealing was done at 825°C for 20 min under arsenic overpressure. The profile shows a maximum carrier concentration of 2.4×10^{17} cm^{-3} which agrees with that obtained by CV measurement. The mobility profile varies from 3000 cm^2/V-s at the surface to over 4000 cm^2/V-s toward the SI substrate, which agrees with the measured average mobility of 3520 cm^2/V-s for the entire layer. The profile deduced from CV measurement after normalization in carrier

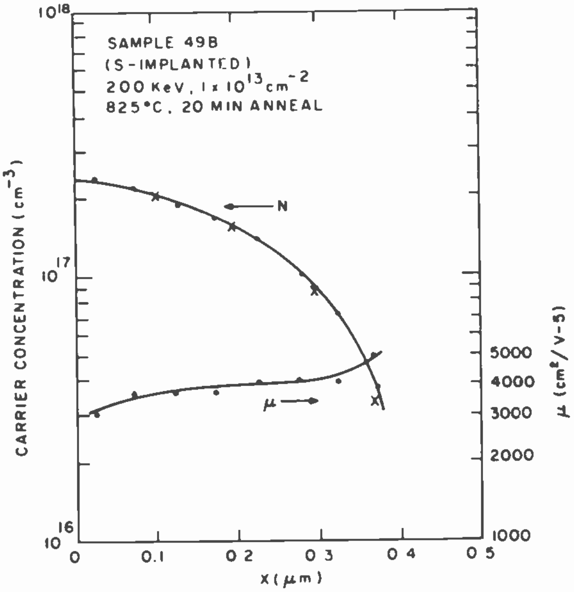

Fig. 7—Carrier concentration and mobility profile of a S implanted sample.

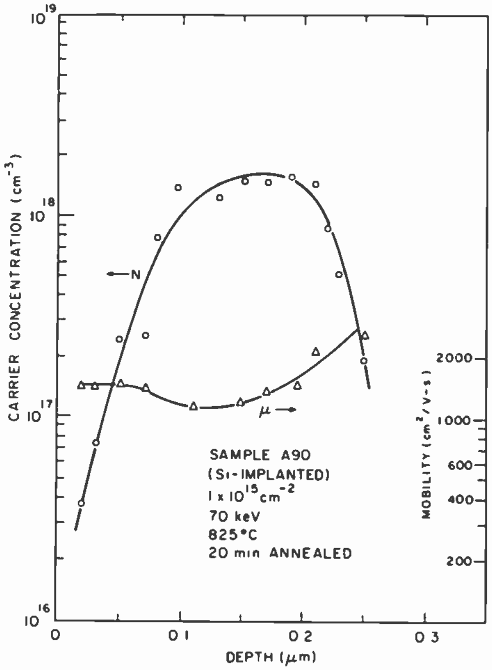

Fig. 8—Carrier concentration and mobility profile of a Si implanted wafer, 70 keV.

concentration matches well with the profile measured by differential Van der Pauw measurement. The normalized points are indicated by crosses in Fig. 7. Both cases are for S implantation at 200 keV with different implant doses. The carrier concentration and mobility profiles of a high-dose Si-implanted GaAs wafer is shown in Fig. 8. The average mobility and sheet carrier concentration of the wafer are 1800 cm^2/V-s and 2.14×10^{13} cm^{-2}, respectively.

(e) Electron Concentration and Drift Mobility Profile

Pucel and Krumm[21] have shown that the depth distribution of the drift mobility of a semiconductor layer on an SI substrate can be measured by a long-gate FET fabricated thereon. This technique measures the transconductance g_m and the capacitance C_g under various gate-bias voltage. At a given gate bias voltage, the drift mobility μ_d is given by

$$\mu_d = \frac{g_m}{C_g} \frac{L^2}{V_{dd}}, \qquad [12]$$

where L is the gate length and V_{dd} the dc voltage between the source and drain.

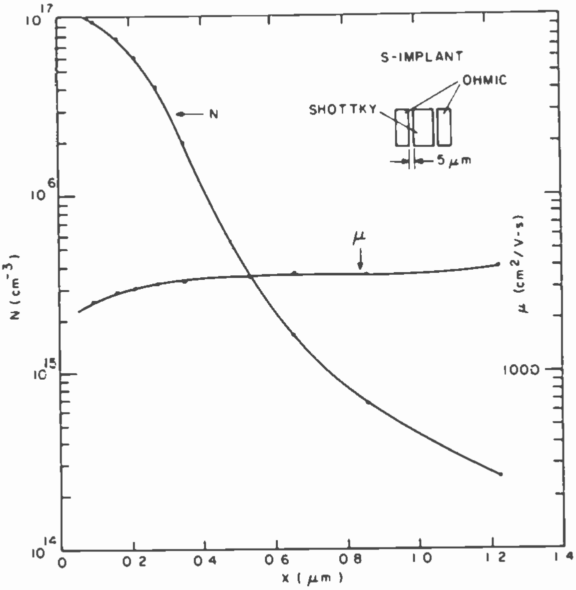

Fig. 9—Drift mobility and electron density profile of a S implanted GaAs wafer.

The depth x_o corresponding to this mobility value is

$$x_o = \frac{\epsilon WL}{C_g}, \qquad [13]$$

where ϵ is the dielectric constant and W, L, are the width and length of the gate, respectively. Using the capacitance versus gate bias data, the carrier concentration profile can be simultaneously determined.

Fig. 9 shows an example of drift mobility and electron density profile of a S-implanted sample. The drift mobility varies between 2500 cm^2/V-s toward the surface and 3800 cm^2/V-s toward the substrate. The effective Hall mobility for the sample was 3250 cm^2/V-s. The ratio of Hall to drift mobility is thus close to unity. The sample was S-implanted at 200 keV with a fluence of 1×10^{13} cm^{-2} and annealed at 825°C for 20 minutes.

(f) Impurity Atom Concentration Profile

The measurements described so far give information on the depth distribution of charge carriers associated with electrically active centers and not necessarily the true range distribution of the implanted atoms. The true impurity atom distribution was measured by secondary ion mass spectrometry (SIMS). Figs. 10 and 11 show, respectively, SIMS

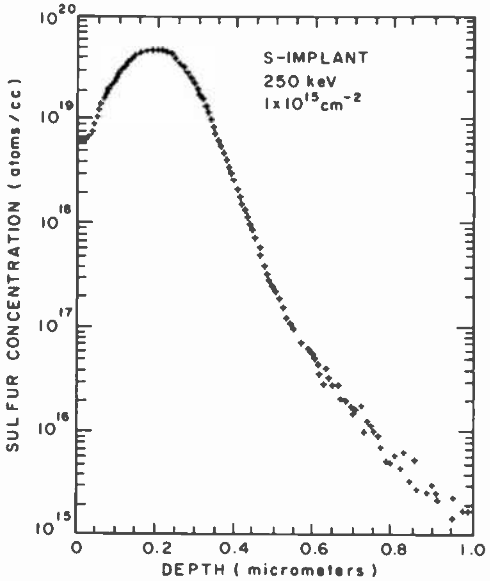

Fig. 10—SIMS profile of S implant made at energy of 250 keV with fluence of 1×10^{15} cm^{-2}.

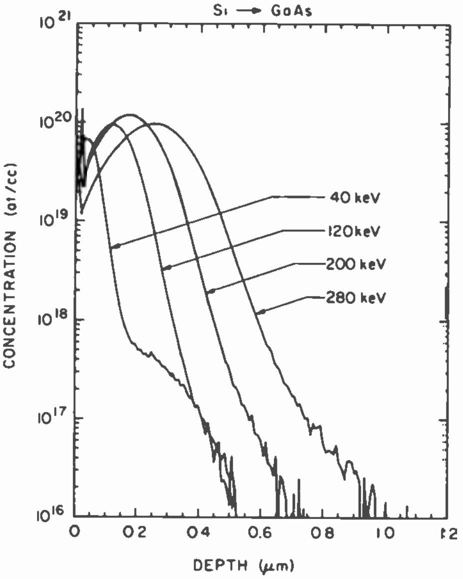

Fig. 11—SIMS profiles of Si implants made at energies of 40, 120, 200, and 280 keV.

profiles of a S-implanted and a number of Si-implanted samples. The distribution is approximately Gaussian except with a broad tail. The projected range and straggle values for Si implantation in GaAs deduced from SIMS are discussed later.

6.2 High Energy (1.2 MeV) ^{28}Si Implantation—Thermal Annealing

The profiles and range statistics of ^{28}Si implants in GaAs up to 1.2 MeV have been analyzed using SIMS. Based on the information obtained, uniformly-doped ^{28}Si profiles $\sim$ 1-μm deep have been produced in GaAs using multiple implants. This section discusses the implanted profiles, dopant activation analyses, and mobility measurements on implanted (single or multiple) and annealed GaAs wafers.

(a) Atomic Profiles—Range Statistics

Fig. 12 shows the SIMS profiles of a series of single-energy implants made over a range of 0.7 to 1.2 MeV. Note that the profiles are not Gaussian in shape but are noticeably skewed. A theory developed by Karl Pearson[22,23] and applied to ^{11}B implants into Si at energies up to 800 keV by Hofker[24] makes use of the first four experimental moments to produce fits to the observed profiles. From these calculations, the range R_P and straggle ΔR_P, can be obtained for skewed data.

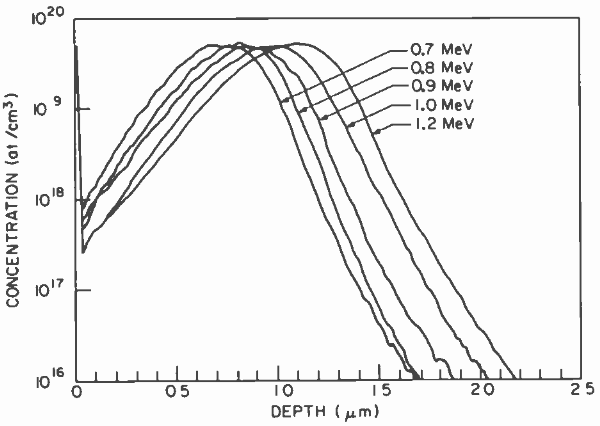

Fig. 12—SIMS profiles of implants made at energies of 0.7, 0.8, 0.9, 1.0, and 1.2 MeV.

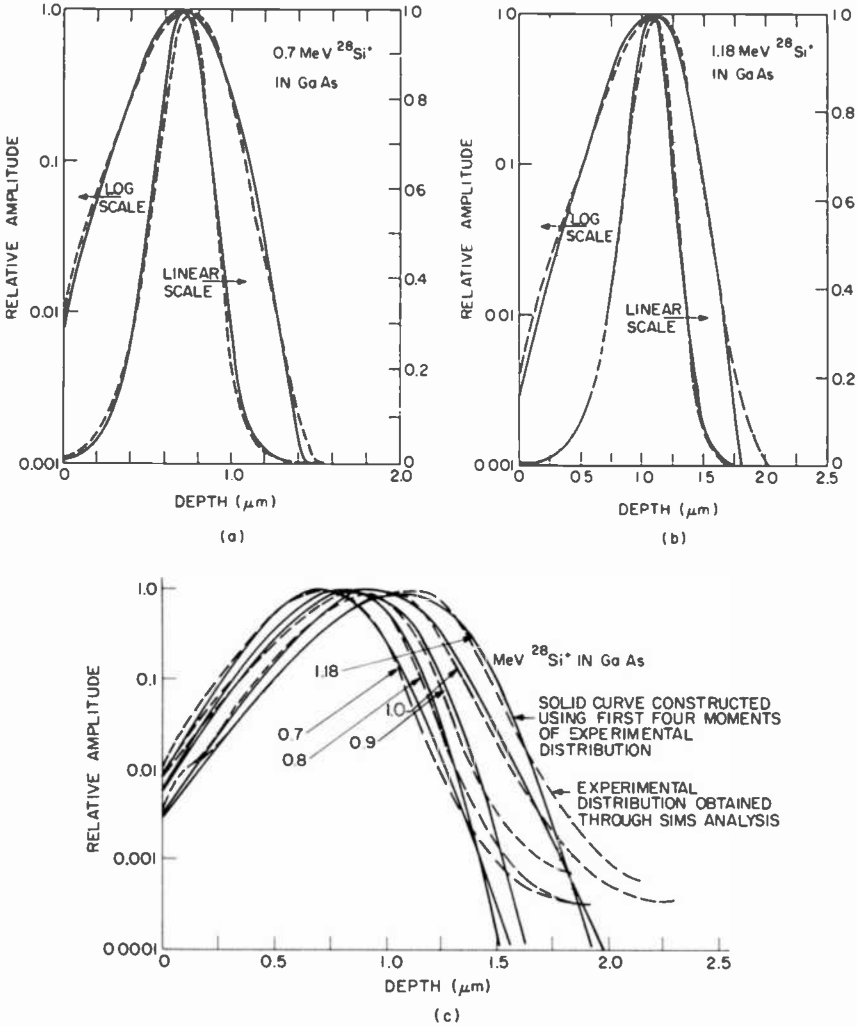

Fig. 13—Curve-fitting to experimental data: (a) 0.7-MeV $^{28}Si^+$ into GaAs and (b) 1.18-MeV $^{28}Si^+$ into GaAs. Curves in (c) shows composite plots of curves corresponding to data given in Fig. 12.

The results of curve fitting to the experimental SIMS data based on the first four experimental moments are shown in Figs. 13(a)–(c). Figs. 13(a) and (b) show both a log and a linear plot of the experimental and calculated data using the formula described by Elderton.[23] Fig. 13(c) shows a composite plot of the curves corresponding to the experimental data given in Fig. 12. Fig. 14 shows a reduction of the data to R_p and ΔR_p

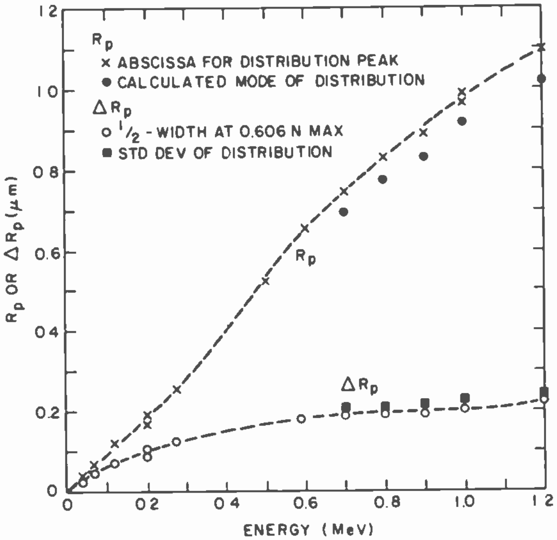

Fig. 14—Reduction of data to R_P and ΔR_P values.

values corresponding to LSS Gaussian reduction techniques and first-four-moment Pearson techniques. Note that the crossovers of the computed curves in Fig. 13(c) and the poor fit of the computed curves to the extended tails at both the shallow and deep portions of the curve indicate that care must be taken to ensure that excessive channeling is not present.

(b) Generation of 1-μm Flat Profile n-layers

Implant conditions were determined for forming ~1-μm-deep layers of Si in GaAs with nearly constant doping. Five implants ranging from 40 to 900 keV are used to construct the layer. Table 4 shows the calculated implant conditions for achieving flat profiles at three different impurity concentration levels: 1×10^{20} cm^{-3} for sample H23, 2.5×10^{19} cm^{-3} for sample H24, and 1×10^{19} cm^{-3} for sample H25.

Table 4—Calculated Multiple Implant Parameters.

H23		H24		H25	
Energy (keV)	Dose (cm^{-2})	Energy (keV)	Dose (cm^{-2})	Energy (keV)	Dose (cm^{-2})
40	4.7×10^{14}	40	1.4×10^{14}	40	4.7×10^{13}
120	1.4×10^{15}	120	4.0×10^{14}	120	1.4×10^{13}
280	1.9×10^{15}	280	5.7×10^{14}	280	1.9×10^{14}
500	2.7×10^{15}	500	8.2×10^{14}	500	2.7×10^{14}
900	4.3×10^{15}	900	1.3×10^{15}	900	4.3×10^{14}

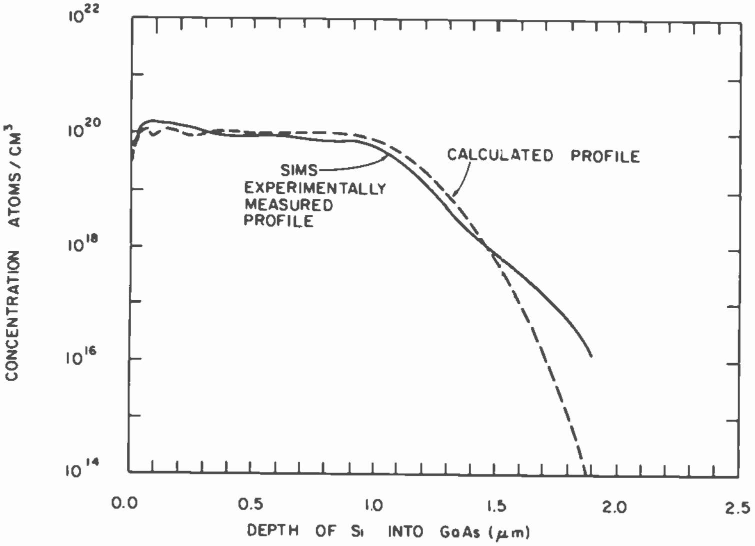

Fig. 15—Comparison of calculated and actual SIMS profiles.

Table 5—Implant Conditions for Flat Profile of Si in GaAs.

Parameter	Energy (keV)				
	40	120	280	500	900
N_{dose} (cm^{-2})	4.70×10^{14}	1.35×10^{15}	1.90×10^{15}	2.73×10^{15}	4.33×10^{15}
Dose No.	303.6	872.0	1227.0	550.2	872.6
Scale	6×10^{-6}	6×10^{-6}	6×10^{-6}	6×10^{-6}	6×10^{-6}
	Area = 24.19 cm^2 (Labs machine)			Area = 7.56 cm^2 (FEC machine)	

A comparison of the calculated plot* and the measured SIMS profile is given in Fig. 15. Implantation data are shown in Table 5.

(c) Mobility, Carrier Concentration, and Activation Efficiency

Following thermal annealing, the electrical characteristics of the high-energy implanted n-layers were evaluated by Van der Pauw measurements.[8] Table 6 shows the measured sheet carrier concentration N_s, sheet resistance ρ_s, Hall mobility μ, and the activation efficiency η, for 1-MeV Si-implanted GaAs. The implanted Si doses varied between 1.5×10^{13} and 5×10^{15} cm^{-2}. The mobilities and activation efficiencies

---

* The calculated data were made using conventional LSS R_P and ΔR_P values because at the time of calculation, the Pearson four-moment-curve fits had not yet been investigated.

Table 6—1-MeV Si Implantation in GaAs.

Sample No.	Dose (cm^{-2})	N_s (cm^{-2})	ρ_s ($\Omega/\square$)	μ ($cm^2/V\text{-}s$)	η (%)
H15	5.0×10^{15}	3.7×10^{13}	85	2000	0.7
H16	1.5×10^{15}	5.7×10^{13}	65	1690	3.8
H17	5.0×10^{14}	7.3×10^{13}	49	1760	14.7
H18	1.5×10^{14}	4.6×10^{13}	52	2620	30.8
H19	5.0×10^{13}	2.7×10^{13}	70	3310	54.2
H20	1.5×10^{13}	1.1×10^{13}	142	3980	73.5

obtained are either comparable to or better than those obtained with low-energy implantation at comparable dose levels (Table 2). The mobilities are in the range of 1690 cm^2/V-s for high-dose implanted samples to 3980 cm^2/V-s for low-dose implanted samples; the activation efficiencies are in the range of below 1% for high-dose implanted samples to over 73% for low-dose implanted samples. All data shown in Table 6 are for samples capless-annealed at 825°C for 20 min.

The activation efficiency of heavily implanted samples increased at a higher annealing temperature. This result is shown in Table 7 where Si-implanted wafers were annealed at two different temperatures, 825 and 970°C. The two samples annealed at 970°C give rise to a higher activation efficiency. The annealing was done in a N_2 atmosphere with samples encapsulated with 2000-Å-thick reactively sputtered Si_3N_4.

Fig. 16 shows the measured sheet carrier concentration as a function of dose for samples implanted at 200 keV and 1 MeV and annealed thermally at 825°C for 20 min. The 1 MeV implanted samples showed a substantially higher sheet carrier concentration in the dose range of 5×10^{13} to 2×10^{15} cm^{-2}. This is because, at a given dose level, the 1 MeV implant results in a lower impurity concentration distribution than that of the 200 keV implantation, because of its higher straggle. The drop in the sheet carrier concentration at high-doses is not fully understood.

Table 7—Results of Si-Implanted Wafers at 825 and 970°C.

Parameters	Sample No.			
	H10		H11	
Energy (keV)	900		1000	
Dose (cm^{-2})	3.0×10^{15}		3.1×10^{15}	
Anneal Temp. (°C)	825	970	825	970
N_s (cm^{-2})	4.2×10^{13}	2.1×10^{14}	3.7×10^{13}	1.5×10^{14}
ρ_s ($\Omega/\square$)	84	22	93	27
μ ($cm^2/V\text{-}s$)	1800	1320	1810	1550
η (%)	1.4	7.1	1.2	4.7

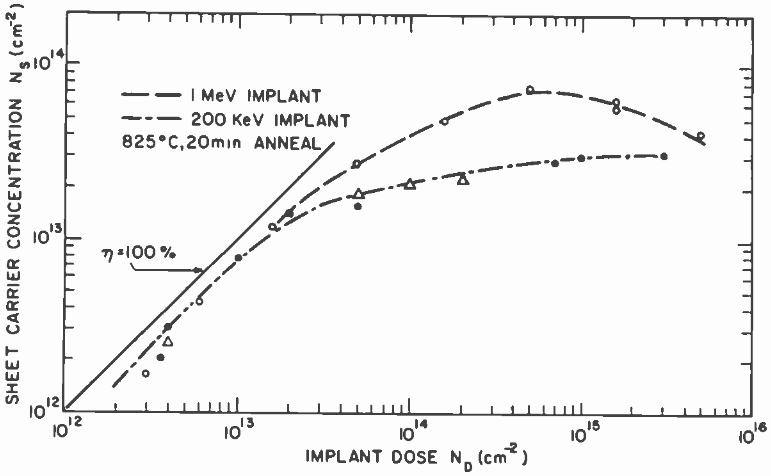

Fig. 16—Measured sheet carrier concentration as a function of dose in Si implanted samples at 200 keV and 1 MeV.

(d) Carrier Concentration Distribution

The electron density profiles of high-energy-implanted thermally-annealed samples were evaluated using differential *CV* measurements in conjunction with controlled layer removal. Figs. 17 and 18 show typical electron concentration distributions. Fig. 17 is for samples implanted at an energy level of 1 MeV, with fluences of 5 × 10^{13} (H19) and 1.5 × 10^{13} cm^{-2} (H20). A SIMS profile of a high dose (5 × 10^{14} cm^{-2}), 1 MeV implanted unannealed sample is also shown in Fig. 17 to provide a reference. Fig. 18 shows the profile of a multiple-implanted sample designed

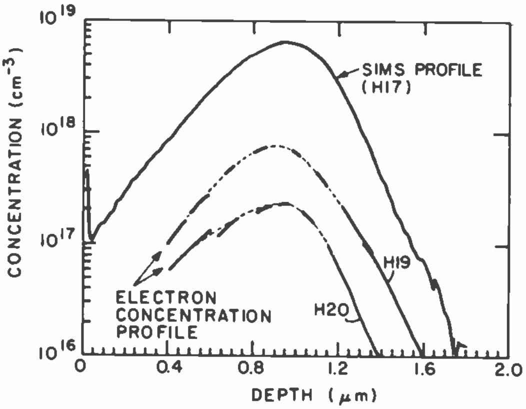

Fig. 17—Profiles of 1 MeV Si implanted GaAs.

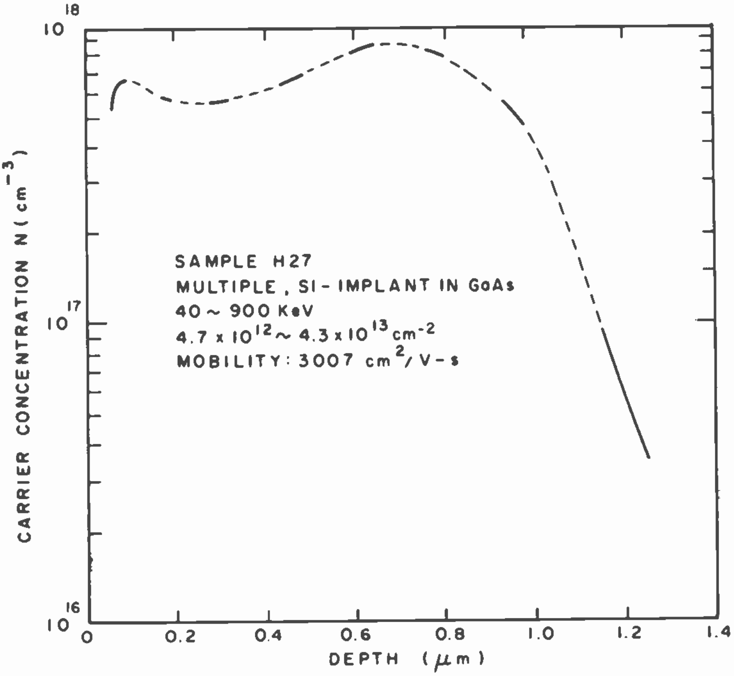

Fig. 18—Carrier concentration of a multiple-implanted sample.

to produce a 1-μm flat profile with a maximum impurity concentration of 1×10^{18} cm^{-3}. The implant parameters are the same as those shown in Table 5, only the fluences are two orders of magnitude lower. These were samples capless-annealed at 825°C for 20 min. under arsenic over-pressure.

The shape of the profiles show reasonable agreement with the SIMS measurements made on high-dose implanted unannealed samples. The differences in range and standard deviation are approximately within 10% on the 1-MeV single energy implanted samples. The deviations between the multiple-implanted profiles determined by the SIMS (Fig. 15) and the *CV* measurement (Fig. 18) are greater. This is expected because the *CV* measurement determines the electrically active carrier concentration distribution and the activation efficiency varies with dose and energy. A better match can be obtained by including the dose-and-energy-dependent activation efficiency in flat-profile design.

6.3 Pulsed Nd:Glass Laser Annealing

Semi-insulating (100) GaAs substrates were implanted with $^{28}Si^+$ at energies between 70 and 200 keV and fluence between 3×10^{12} and $3 \times$

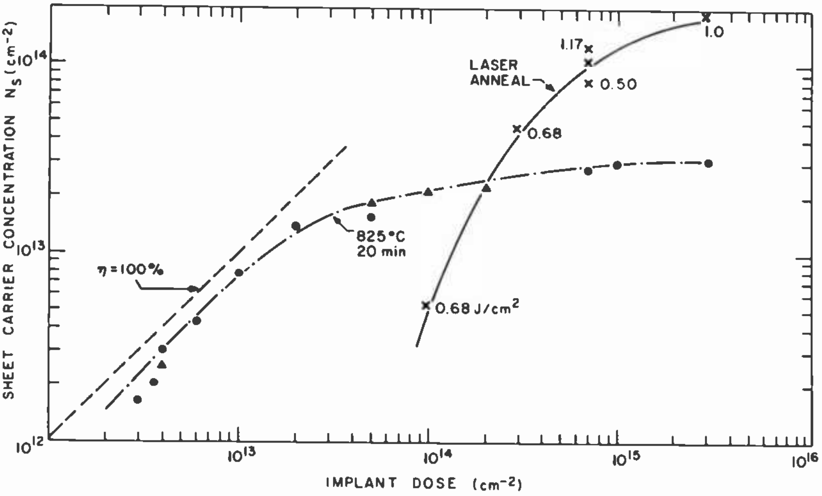

Fig. 19—Comparison of thermal and laser annealing; a 1.06-μm, 25-ns single pulse (Nd: Glass) laser was used.

10^{15} cm^{-2}. Some substrates were polished on both sides to facilitate optical absorption studies. Following implantation, the 0.04 cm-thick wafer was cleaved to samples between 0.5 and 2.0 cm^2 for laser-annealing experiments.

The Nd:Glass laser was operated at an output energy density of between 0.2 and 2.5 J/cm^2 per pulse. The corresponding power density lies between 8 and 200 MW/cm^2. The laser diameter is 2 cm. Thermally annealed samples used as control were annealed at 825°C for 20 min. under arsenic overpressure.

Fig. 19 shows comparative results of sheet carrier concentration density for Nd:Glass laser and thermally annealed samples for implanted ^{28}Si doses between 3×10^{12} and 3×10^{15} cm^{-2}. The energy density of each laser pulse used is indicated by crosses and varies between 0.5 and 1.17 J/cm^2. All experiments used single pulses. At low laser energy density the implanted layers were only partially activated.

Table 8 lists comparative results on mobility, sheet carrier concentration, and activation efficiency for Si-implanted GaAs annealed using Nd:Glass laser and thermally. The fluences are greater than 3×10^{14} cm^{-2}. The laser-annealed samples showed higher activation efficiencies and lower mobility than thermally annealed samples.

The optical absorption in the sample was measured by spectrophotometry. The transmission through the sample and the reflection from the sample were measured on a Cary spectrometer in the 7000- to

Table 8—Comparison of Thermal and Nd:Glass Laser Annealing Data.

Si Implantation					
Dose (cm^{-2})	3.0×10^{15}	3.0×10^{15}	1.0×10^{15}	$5/2 \times 10^{14}$	3.0×10^{14}
Energy (keV)	70	200	70	200/70	200
Nd:Glass Laser Annealing					
Energy (J/cm^2)	1.00	2.25	0.34	1.17	0.68
N_s (cm^{-2})	1.91×10^{14}	1.45×10^{14}	6.55×10^{13}	1.25×10^{14}	4.60×10^{13}
μ (cm^2/V-s)	250	1020	250	530	520
η (%)	6.4	4.8	6.6	17.9	15.3
Thermal Annealing					
N_s (cm^{-2})	5.1×10^{13}	3.3×10^{13}	3.2×10^{13}	2.8×10^{13}	3.0×10^{13}
μ (cm^2/V-s)	1390	1910	1770	1880	1540
η (%)	1.7	1.1	3.2	4.0	10.0

12000-Å wavelength range. The absorption at a given wavelength (e.g., 1.06 μm) is calculated by the expression:

$$A = 1 - T - R$$

where A, T, and R are respectively, absorption, transmission, and reflection which are all absolute values and are expressed in percentages. The enhanced absorption due to implantation damage is equal to $A - A_0$, where A_0 is the absorption through the unimplanted sample. At 1.06-μm wavelength, the measured value of A_0 was typically 0.1. The reflectance was measured with reference to an aluminum mirror and the absolute value obtained through calibration.

Fig. 20 shows the reflectance measured on an as-implanted wafer and

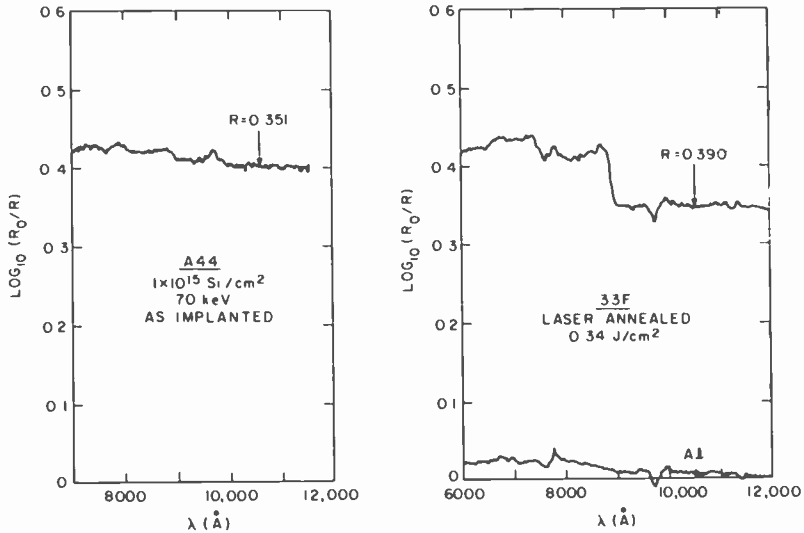

(a) (b)

Fig. 20—Reflectance measured (a) on an as-implanted wafer and (b) after laser annealing.

on the same wafer irradiated with a Nd:Glass laser pulse at an energy density of 0.34 J/cm^2. Because of the enhanced absorption in the high-dose implanted layer, the reflection is affected only by the front (implanted) surface. Consequently, the reflectance forms a continuous line as it passes through the absorption edge as shown in Fig. 20(a). For the annealed samples, restored lattice order reduces the enhanced absorption in the implanted layer. The reflectance spectrum thus forms a step, as shown in Fig. 20(b), as the wavelength passes through the band edge of GaAs, because the reflection is enhanced in the long wavelength range due to multiple reflection from the polished sample back surface. The multiple reflection dominates over the change in surface reflectivity which occurs as a result of implantation.

The transmittance through an ion-implanted sample before and after annealing is shown in Fig. 21. The gradual increase in absorption from the long-wavelength side toward the absorption edge in the as-implanted sample is a band-tailing effect produced by impurities.[25] The transmittance at 1.06-μm wavelength changes from 0.170 for the as-implanted sample to 0.457 after laser annealing at 0.68 J/cm^2. The enhanced ab-

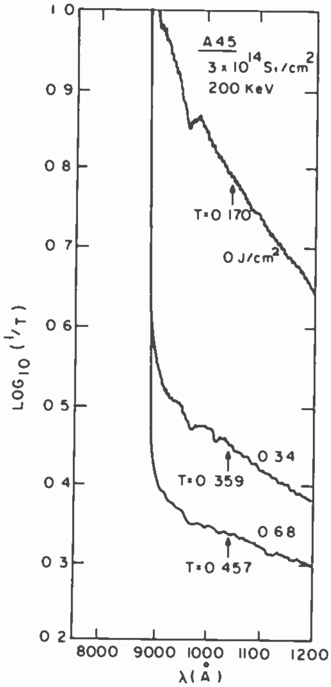

Fig. 21—Optical transmission from Si-implanted GaAs sample annealed at different laser energy densities.

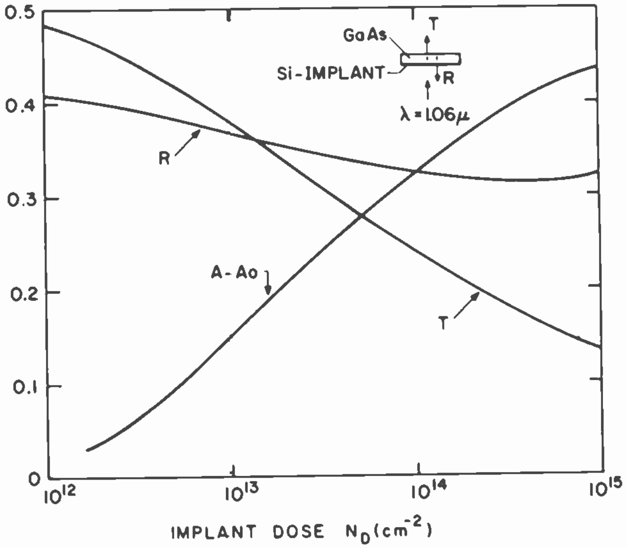

Fig. 22—Measured values of transmittance (*T*), reflectance (*R*), and enhanced absorption ($A - A_o$) for different dose levels.

sorption ($A - A_o$) can be evaluated from the expression given in the previous section. Fig. 22 shows the measured values of transmittance, reflectance, and enhanced absorption for as-implanted samples at different dose levels.

Optical absorption measurements show that the implantation-enhanced absorption at a given wavelength (e.g., 1.06 μm) below the band edge increases with implant dose. This enhanced absorption is greatly reduced following annealing as a result of lattice re-ordering. Such optical measurement may thus be used as a diagnostic technique for optimizing the required laser energy while maintaining good surface morphology.

6.4 Pulsed Ruby-Laser Annealing

Laser-annealing experiments were also carried out using a ruby laser on Si-implanted samples. The substrates were implanted at 70, 100, and 200 keV, with doses ranging between 1×10^{14} and 1×10^{16} cm^{-2}. The Q-switched ruby laser was operated with an output density of between 0.5 and 2.3 J/cm^2 per 25 ns pulse.

Fig. 23 shows the sheet carrier concentration as a function of the implantation dose for samples annealed by a high-power pulsed ruby laser and control samples annealed thermally. The thermal annealing was done under arsenic overpressure at 825° and 900°C for 20 min. The

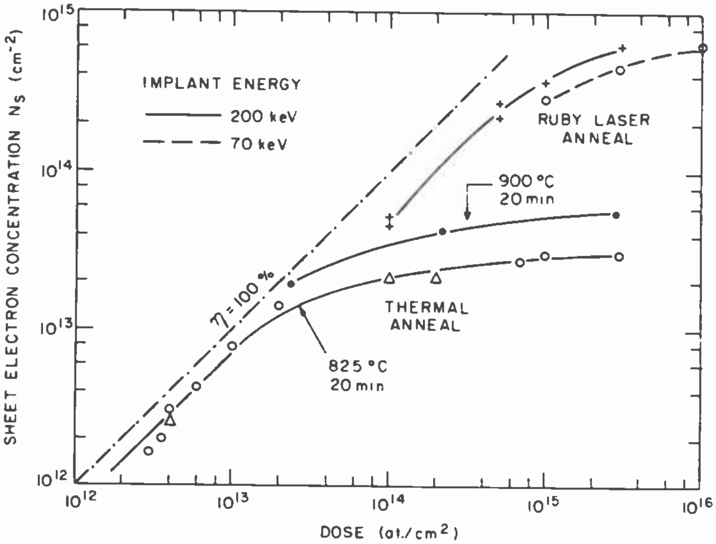

Fig. 23—Sheet electron concentration as a function of dose for ruby-laser and thermal-annealed samples.

implantation energy was 200 keV. The AsH_3 flow rate was adjusted so that the arsenic overpressure remained constant at 825 and 900°C.[7] The laser energy densities used were 1.7 and 2.3 J/cm^2, which are higher than that shown in Fig. 19. Note that high dose samples implanted at 200 keV show higher activation efficiencies than those implanted at 70 keV. This may be because the impurity density in the implanted layer is higher in the 70 keV implanted sample than in the 200 keV implanted sample because of smaller straggle. A sheet carrier concentration density of up to 6.25×10^{14} cm^{-2} with 20.8% activation efficiency was measured on high-dose implanted samples. *These results show an order of magnitude higher activation efficiency than that for similar samples annealed thermally.*

The electrical characteristics of laser-annealed samples depend on the implantation energy and fluence, and the energy density of the laser irradiation. Fig. 24 shows a plot of the mobility μ, the activation efficiency η, and the sheet resistance ρ_s, for 200 keV Si-implanted GaAs wafers implanted with three different fluences and ruby-laser annealed at 2.3 J/cm^2. Activation efficiencies of 45 to 56% and mobilities of 930 to 1350 cm^2/V-s were measured in wafers implanted at a dose level ranging from 1×10^{14} to 5×10^{14} cm^{-2}. The sheet resistances at the high-dose region shown in Fig. 24 are typically 4 to 5 times lower than for similar wafers thermally annealed. Fig. 25 shows the mobility, sheet resistance, and activation efficiency of Si-implanted GaAs wafers irradiated by a ruby

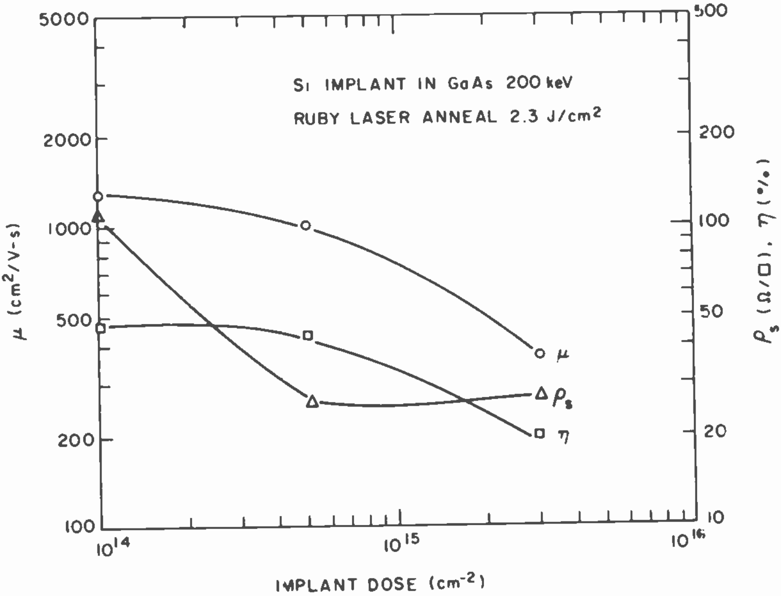

Fig. 24—Mobility (μ), activation efficiency (η), and sheet resistance (ρ_s) as a function of dose.

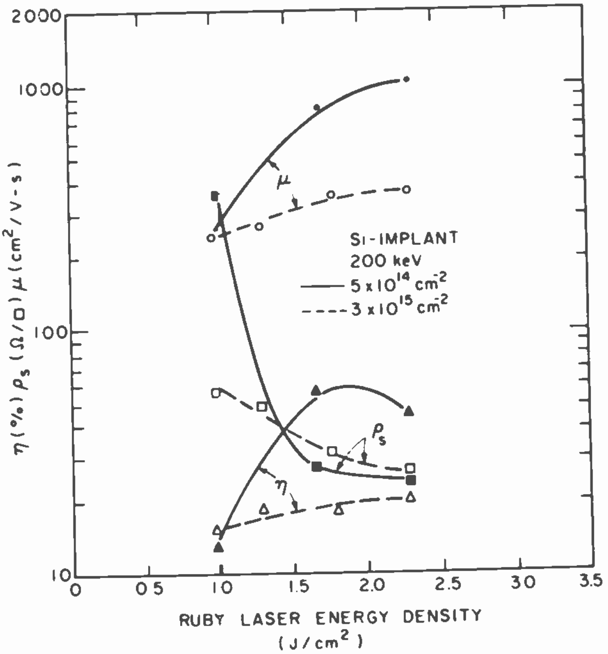

Fig. 25—Mobility (μ), activation efficiency (η), and sheet resistance (ρ_s) as a function of laser energy density.

laser operated at different energy densities. The wafers were implanted at 200 keV with fluences of 5×10^{14} and 3×10^{15} cm^{-2} respectively. The data points indicate that mobility and activation efficiency are much higher for samples irradiated at a higher energy density (1.7 to 2.3 J/cm^2) than they are for lower energy density (1.0 J/cm^2). However, the activation efficiency of the ~1 J/cm^2 irradiated samples is still much higher (>2 for 5×10^{14} cm^{-2} implants, and >10 for 3×10^{15} cm^{-2} implants) than that of similar samples thermally annealed at 825°C.

6.5 Impurity Redistribution

Impurity redistribution caused by annealing was studied using SIMS. Fig. 26 shows the SIMS profile of a 200 keV, 5×10^{14} cm^{-2} Si-implanted GaAs sample before and after thermal annealing (825°C, 20 min.). The peak impurity concentration was 2.3×10^{19} cm^{-3}. No impurity redistribution were observed after thermal annealing. Fig. 27 shows the SIMS profile of a Si-implanted GaAs before thermal annealing and the SIMS profile and electron density profile after thermal annealing at 825°C for 20 min. The electron density profile was measured by differential Van der Pauw measurement. This sample was implanted at 70 keV with a dose of 3×10^{15} cm^{-2}. The peak impurity concentration was 3.2×10^{20}

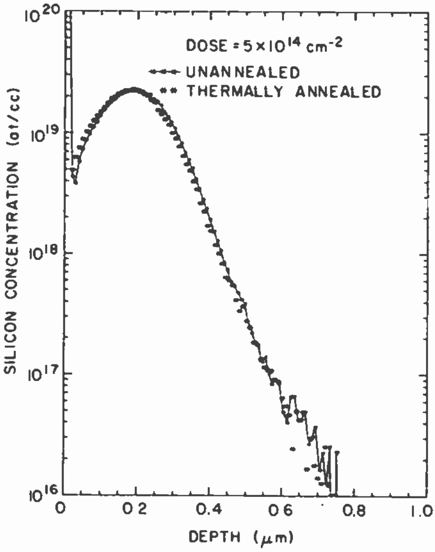

Fig. 26—SIMS profile of a Si implanted GaAs sample before and after thermal annealing (200 keV, 5×10^{14} cm^{-2}).

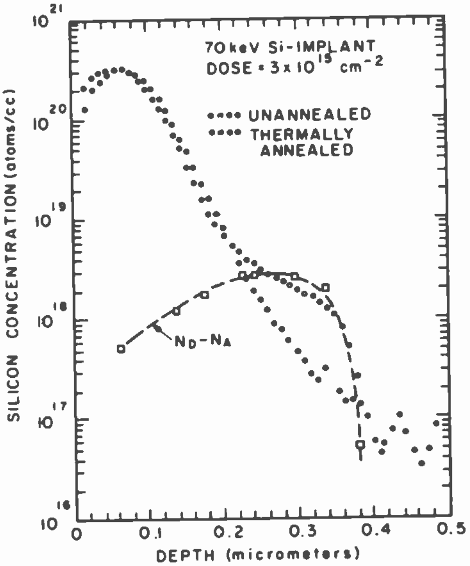

Fig. 27—SIMS profile of a Si-implanted GaAs sample before and after thermal annealing (70 keV, 3 X 10^{15} cm^{-2}). Carrier concentration profile is also shown.

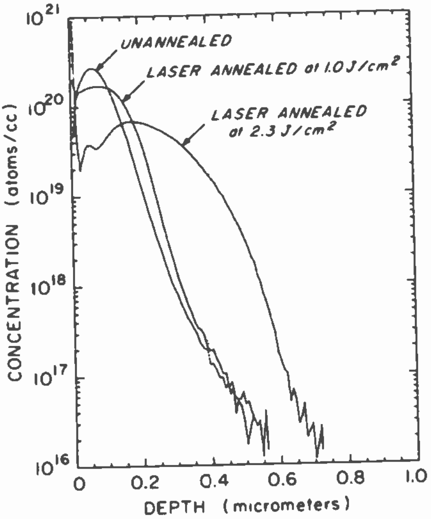

Fig. 28—SIMS profiles for unannealed GaAs wafer laser-annealed at 1 J/cm^2 and laser-annealed at 2.3 J/cm^2.

cm^{-3}. A shoulder broadening effect occurs at an impurity concentration of about 3×10^{18} cm^{-3}, which approximately coincides with the peak of the electrically active electron density profile. This is believed to be caused by damage-enhanced diffusion of unprecipitated silicon similar to that reported for Se-implanted GaAs.[26]

Fig. 28 shows three SIMS profiles: one for an as-implanted GaAs wafer at 70 keV with a dose of 3×10^{15} cm^{-2}, the other two are for samples from the same wafer after irradiation with a single ruby-laser pulse at energy densities of 1.0 and 2.3 J/cm^2. A redistribution in impurity density was observed for the laser-irradiated samples. The impurity profile broadening associated with the short-duration (30 ns), high-energy, laser pulse irradiation suggests that surface melting occurs, and the substantial broadening in impurity distribution is a result of diffusion in liquid GaAs similar to that reported previously in silicon.[27,28]

6.6 Cr-Redistribution

Preliminary studies on the redistribution of Cr from the SI GaAs substrate due to the implantation and annealing operations were carried out. Indications are that the redistribution of Cr is a strong function of implant dose and the annealing method. Fig. 29 shows the atomic Cr profile for a 1 MeV, 1×10^{13} cm^{-2} ^{28}Si implanted sample after capless

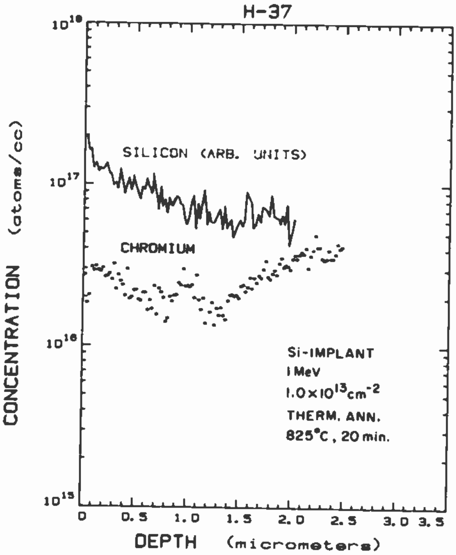

Fig. 29—SIMS profiles of ^{52}Cr and ^{28}Si in low-dose Si-implanted thermally annealed GaAs sample.

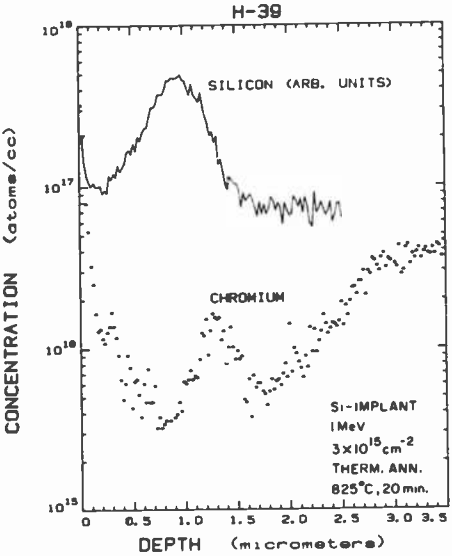

Fig. 30—Chromium concentration profile of 1 MeV Si-implanted thermally-annealed GaAs; Si profile in arbitrary units is also shown.

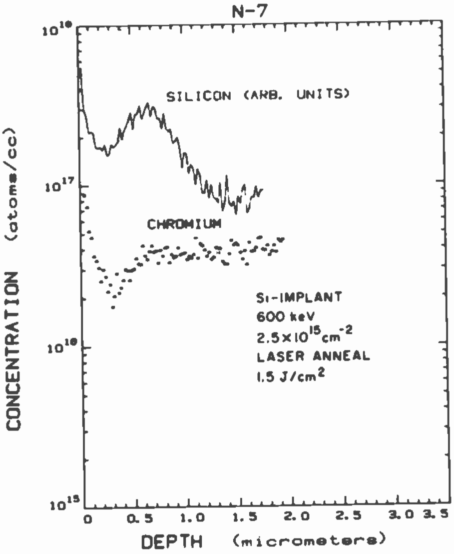

Fig. 31—Chromium concentration profile of 600 keV Si-implanted laser annealed GaAs; Si profile in arbitrary units is also shown.

thermal anneal (825°C for 20 min). Note the depletion of ^{52}Cr in the implanted region relative to the concentration in the substrate (approximately 5×10^{16} cm^{-3}). The ^{28}Si profile is also shown in arbitrary units. (The low Si detection efficiency is a result of using an O^+ primary beam instead of Cs^+.) Very little Cr redistribution is seen for implant doses of $2–4 \times 10^{12}$ cm^{-2} which are typically used to obtain 10^{17} cm^{-3} carrier concentrations for the active layers of microwave FETs. Fig. 30 shows the Cr redistribution for an 1 MeV, 3×10^{15} cm^{-2} implanted capless-annealed sample. Note the dramatic increase in Cr redistribution at this higher implant dose. Fig. 31 shows similar Cr and Si profiles for a 600 keV, 2.5×10^{15} cm^{-2} implanted Nd:Glass laser-annealed sample. Note the substantially smaller Cr redistribution compared to Fig. 30. These phenomena are still under investigation.

7. Summary

Ion implantation of Si and S into SI GaAs and the characteristics of the implanted layers after thermal or laser annealing were investigated. Implantation of ^{28}Si was studied over an energy range from 40 keV to 1.2 MeV and fluence range of 10^{12} to 10^{16} cm^{-2}. A capless thermal annealing technique under arsenic overpressure was developed; the technique prevents dissociation of GaAs and results in good surface morphology. Uniformly doped ~1 μm deep n-layers were realized in GaAs using multiple implants.

The activation efficiency varies between 40 and 90% in the dose range between 3×10^{12} and 5×10^{13} cm^{-2} (implant energy 200 keV) and decreases toward the high-dose level. A threshold fluence was observed below which the implanted layer was no longer activated. This "cut off" dose depends on the substrate characteristics and is typically $\sim 2 \times 10^{12}$ cm^{-2}. The sheet electrical conductivities of as-implanted SI GaAs show similar qualitative dose-level dependence to that of the electron density in thermally annealed samples. The electron density of the n-layer is limited to $\sim 5 \times 10^{16}$ cm^{-3} at the lower end and to $\sim 3 \times 10^{18}$ cm^{-3} at the higher end following thermal annealing. Typical mobilities at an electron density of $1–2 \times 10^{17}$ cm^{-3} were 3500–4000 cm^2/V-s. High dose ($\gtrsim 1 \times 10^{14}$ cm^{-2}) Si-implanted SI GaAs after irradiation with either a Q-switched ruby laser or Nd:Glass laser show higher sheet electron concentration but lower mobility than that of thermally annealed samples.

The measured depth distribution of electron concentration are broader for S-implanted than for Si-implanted GaAs. The broader electron density profile is a result of thermal diffusion during annealing. The diffusion coefficient at 825°C for S and Si in GaAs was deduced from the electron density profiles to be 2–5 × 10^{-14} and $\leq 10^{-15}$ cm^2/s, respectively.

Optical absorption studies on Si-implanted Nd:Glass laser irradiated GaAs show that the implant-enhanced absorption at a given infrared wavelength increases with implant dose. The enhanced absorption is greatly reduced following annealing as a result of lattice reordering.

The redistribution of implanted Si following thermal or laser annealing was studied using SIMS. Preliminary results on redistribution of Cr in SI GaAs due to implantation and annealing were also measured. The redistribution of implanted Si after annealing depends on the amount of implant damage and also on the energy density of the laser pulse.

Acknowledgments

We are indebted to J. Nering at Fusion Energy Corporation for his assistance and cooperation in high energy implantation, to P. J. Zanzucchi for helpful discussions on optical measurements, to E. Beck for assistance in annealing, and to F. Sterzer and M. Yoder (Office of Naval Research) for their constant encouragement and support.

References:

[1] A. G. Foyt, J. P. Donnelly, and W. T. Lindley, "Efficient Doping of GaAs By Se$^+$ Ion Implantation," *Appl. Phys. Lett.* **14**, p. 372, 1969.

[2] J. S. Harris, F. H. Eisen, B. M. Welch, J. D. Haskell, R. D. Pashly, and J. Mayer, "Influence of Implantation Temperature and Surface Protection on Tellurium Implantation in GaAs," *Appl. Phys. Lett.*, **21**, p. 601 (1972).

[3] W. K. Chu, et al., *Proc. 3rd Int. Conf. on Ion Imp.*, Plenum Press, New York (1973).

[4] R. D. Pashley and B. M. Welch, "Tellurium-Implanted N$^+$ Layers in GaAs," *Solid State Electronics*, **18**, p. 977, 1975.

[5] A. Lidow and J. F. Gibbons, "A Double-Layered Encapsulant for Annealing Ion-Implanted GaAs Up to 1100°C," *Appl. Phys. Lett.*, **31**, p. 158, 1977.

[6] B. J. Sealy and R. K. Surridge, "A New Thin Film Encapsulant for Ion-Implanted GaAs," *Thin Solid Films*, **26**, p. L19, April 1974.

[7] J. R. Arthur, "Vapor Pressures and Phase Equilibria in the GaAs System," *J. Phys. Chem. Solids*, **28**, p. 2257, 1967.

[8] L. J. Van der Pauw, "A Method of Measuring Specific Resistivity and Hall Effect of Discs of Arbitrary Shape," *Philips Res. Repts.*, **13**, p. 1 (1958).

[9] L. C. Northcliffe and R. F. Schilling, *Nuclear Data Tables*, **47**, p. 233–463, 1970.

[10] J. Linhard, M. Scharff, and H. E. Schiott, *Mat. Fys. Medd. Dan. Vid. Selsk.*, **33**, No. 14, 1963.

[11] D. L. Rode and S. Knight, "Electron Mobility in GaAs," *Phys. Rev.*, **B3**, p. 2534, 1971.

[12] J. P. Donnelly, "Ion Implantation in GaAs," 1976 North American Symposium on GaAs and Related Compounds, Conference Series number 33b, The Institute of Physics, Bristol and London.

[13] Y. Kato et al., "Electrical Conductivity of Disordered Layers in GaAs Crystal Produced by Ion Implantation," *J. Appl. Phys.*, **45**, p. 1044, 1974.

[14] C. O. Thomas, D. Kahng, and R. C. Manz, "Impurity Distribution in Epitaxial Silicon Films," *J. Electronchem. Soc.*, **109**, p. 1055, 1962.

[15] C. P. Wu, E. C. Douglas, and C. W. Mueller, "Limitations of the CV Technique for Ion-Implanted Profiles," *IEEE Trans. on ED*, **22**, p. 319, 1975.

[16] A. B. Y. Young and G. L. Pearson, "Diffusion of Sulfur in GaP and GaAs," J. Phys. Chem. Solid, **31**, p. 517, 1970.

[17] A. Asai and H. Kodera, "Electrical Properties of n-type Layers in GaAs prepared by Solid Sulfur Dif-

fusion," *Proc. 4th Int. Symp. Boulder, CO*, p. 130, 1972.

[18] P. L. Kendall, *Semiconductors and Semimetals*, Volume IV, Academic Press, New York (1968).

[19] R. Baron, G. A. Shifrin, and O. J. Marsh, "Electrical Behavior of Group III and V Implanted Dopants in Silicon," *J. Appl. Phys.*, **40**, p. 3702, 1969.

[20] J. W. Mayer, L. Eriksson, and J. A. Devies, *Ion Implantation in Semiconductors*, Academic Press, p. 193, New York (1970).

[21] R. A. Pucel and C. F. Krumm, "Simple Method of Measuring Drift Mobility Profiles in the Semi-conductor Films," *Elec. Letts.*, **12**, p. 240, 1976.

[22] M. G. Kendall and A. Stuart, *The Advanced Theory of Statistics*, Vol. 1, p. 148, Charles Griffin, London (1958).

[23] W. P. Elderton, *Frequency Curves and Correlation*, Cambridge University Press, 4th ed. (1953).

[24] W. K. Hofker, "Implantation of Boron in Silicon," *Philips Research Supplements*, 1975, No. 8.

[25] See for example, J. I. Pankove, *Optical Processes in Semiconductors*, p. 10, Prentice-Hall Inc., Englewood Cliffs, NJ (1971).

[26] A. Lidow, J. F. Gibbons, V. R. Deline, and C. A. Evans, Jr., "Solid Solubility of Selenium in GaAs as Measured by Secondary Ion Mass Spectrometry," *Appl. Phys. Lett.*, **32**, p. 572 (1978).

[27] C. W. White, W. H. Christle, B. R. Appleton, S. R. Wilson, P. P. Pronko, and C. W. Magee, *Appl. Phys. Lett.*, **33**, p. 662 (1978).

[28] J. C. Wang, R. F. Wood and P. P. Pronko, *Appl. Phys. Lett.*, **33**, p. 455 (1978).

Patents Issued to RCA Inventors—First Quarter 1980

January

C. H. Anderson and S. Bloom Guided Beam Flat Display Device (30,195)
F. Aschwanden Phase Locked Loop Tuning System Including Stabilized Time Interval Control Circuit (4,182,994)
F. Aschwanden Comb Filter System (4,184,174)
W. E. Babcock Television S-Correction Circuit With Improved Linearity (4,181,874)
W. E. Barnette and F. W. Spong Capacitance Distance Sensor Apparatus For VideoDisc Player/Recorder (4,183,060)
A. Bloom and L. K. Hung Novel Liquid Crystal Dyestuffs And Electro-Optic Devices Incorporating Same (4,184,750)
W. Bohringer Voltage Regulator For A Television Deflection Circuit (4,186,330)
D. W. Breithaupt Remote Control TV Subcarrier Phase Shifter System (4,183,044)
C. A. Catanese and J. G. Endriz Electron Multiplier Device With Surface Ion Feedback (4,182,969)
A. G. Dingwall High Speed Resettable Dynamic Counter (4,181,862)
A. G. Dingwall Inhibitable Counter Stage And Counter (4,182,961)
K. F. Etzold Matching Network For Switchable Segmented Ultrasonic Transducers (4,181,864)
R. A. Gange Proximity Focused Electron Beam Guide Display Device Including Mesh Having Apertures No Greater Than 26 Microns In One Dimension (4,181,871)
J. Goel Self Biasing Of A Field Effect Transistor Mounted In A Flip-Chip Carrier (4,183,041)
G. P. Grill and C. E. Doner Double-Tuned Output Circuit For High Power Devices Using Coaxial Cavity Resonators (4,184,123)
W. E. Ham Method For Cleaning and Drying Semiconductors (4,186,032)
J. R. Harford Synchronization Signal Separator Circuit (4,185,299)
H. E. Haslau Winding Structure (4,183,002)
F. Z. Hawrylo Laser Diode With Thermal Conducting, Current Confining Film (4,182,995)
J. G. Henderson Liquid Crystal Channel Number Display Responsive To Ambient Light Level (4,181,916)
D. C. Herrmann and L. J. Bazin Chroma Keying Selector System (4,183,045)
S. A. Keneman and J. G. Endriz Electron Multiplier With Ion Bombardment Shields (4,182,968)
N. Kucharewski Electrical Circuits (4,185,211)
W. A. Lagoni LED Channel Number Display Responsive To Ambient Light Level (4,181,915)
A. J. Leidich Level Shifting Circuit (4,185,212)
S. Liu and F. C. Duigon Thin Film Pattern Generation By An Inverse Self-Lifting Technique (4,181,755)
R. C. Palmer Track Skipper For A VideoDisc Player (4,183,059)
O. H. Schade, Jr. Amplifier With Field Effect And Bipolar Transistors (4,183,020)
R. C. Shambelan Apparatus For Simultaneously Processing A Plurality Of Substrates (4,185,585)
R. G. Stewart Non-Volatile Memory Device (4,185,319)
S. Weisbrod Row Addressing Apparatus For A Bistable Display Device (4,183,062)
O. M. Woodward Broad Band, Four Loop Antenna (4,184,163)
B. Zuk Contact De-Bouncing Circuit With Common Mode Rejection (4,185,210)

February

K. C. Adam Analog-To-Digital Circuit With Adjustable Sensitivity (4,189,714)
A. E. Bell, R. A. Bartolini, R. A. Shahbender, and B. F. Williams Record Playback Apparatus And Information Record Therefor (4,189,735)
S. L. Bendell Video Image Tube Highlight Suppression Circuit (4,190,865)
A. D. Checki, Jr. Semiconductor Device Package (4,190,735)
R. J. D'Amato and R. A. Nolan Color Picture Tube Having Improved Corrugated Apertured Mask And Method Of Making Same (4,187,443)
A. G. Dingwall Circuitry With Unbalanced Long-Tailed-Pair Connections of FET'S (4,188,588)
A. G. Dingwall Memory Organization (4,189,782)
R. A. Dischert and L. J. Thorpe Remote Control System For A Television Camera (4,190,863)
R. A. Dischert Remote IRIS Control For Television Cameras (4,190,864)
J. E. Hicks Switching Regulator For Television Deflection Circuit With Improved Ultor Voltage Regulation (4,190,791)
L. R. Hulls, L. R. Armstrong, and S. C. Hadden Engine Fault Diagnosis (4,189,940)

L. A. Kaplan RC Oscillator (4,188,593)
H. P. Kleinknecht Optically Measuring The Carrier Concentration In A Semiconductor (4,188,123)
R. J. McCurdy Sampling Method And Apparatuses (4,188,583)
J. G. Ottos Apparatus And Method For Automatically Aligning A Multibeam Electron Gun Assembly With A Cathode-Ray Tube Bulb (4,189,814)
F. N. Sechi Microwave FET Power Circuit (4,189,682)
F. N. Sechi and R. L. Camisa Microwave FET Power Oscillator (4,189,688)
F. W. Spong Recording Methods For A Multilayer Optical Record (4,190,843)
F. Sterzer Apparatus And Method For Hyperthermia Treatment (4,190,053)
J. Valachovic Method And Apparatus For Determining Focus Conditions (4,189,746)

March

J. A. Allen and L. A. Torrington VideoDisc Player having Unitary Record Handling Platform Construction (4,191,380)
A. E. Bell and R. A. Bartolini Recorder and Antireflective Record Blank having an Optically Passive Transparent Layer (4,195,312)
A. E. Bell and R. A. Bartolini Antireflective Information Record having an Optically Passive Transparent Layer (4,195,313)
T. J. Christopher and L. L. Tretter Video Processing System Including Comb Filters (4,195,309)
J. J. Colgan, Jr. Image Pickup Assembly (4,191,936)
R. J. D'Amato and R. P. Stone Color Picture Tube having Improved Corrugated Mask (4,195,248)
E. B. Davidson Water Based Photoresist (4,194,912)
W. F. Dietz Deflection Circuit (4,193,018)
R. A. Dischert and L. J. Thorpe System for Connecting a Plurality of Video Sending Television Apparatus (4,191,971)
M. Ettenberg and H. Kressel Two-Way Single Fiber Optical Communication System (4,195,269)
E. J. Fjarlie Spectrometer (4,193,691)
J. Goel Method of Making a Field Effect Transistor (4,194,285)
J. C. Hartmann and N. F. Maxemchuk Bidirectional Digital Position Encoder (4,194,184)
F. Z. Hawrylo Ohmic Contact for P Type Indium Phosphide (4,195,308)
L. B. Kimbrough and M. Vanrenssen Apparatus for Applying Sealing Material to a Cathode-Ray Tube (4,194,463)
P. A. Levine and D. J. Sauer Low Noise CCD Input Circuit (4,191,895)
E. S. Naidus Double Dome Heat and Smoke Vent Structure (4,190,987)
J. L. Ovnick, Jr. CATV Block Converter (4,191,966)
D. J. Sauer and P. A. Levine Low Noise CCD Input Circuit (4,191,896)
J. F. Springer and D. H. Kaplan Switch Matrix for Data Transfers (4,191,941)
F. R. Stave Apparatus for Facilitating Carriage Return in VideoDisc Player (4,191,381)
F. J. Tams, 3rd Processing Rack (4,191,295)
M. Vanrenssen Apparatus and Method for Determining Deviation of Mask-to-Faceplate Spacing in a Cathode-Ray Tube (4,190,936)
H. E. White and R. J. Petri Digital Phase Synchronizing System (4,191,975)

AUTHORS

Raymond S. Berkowitz received the B.S. in EE (1943), MS in EE (1948), and Ph.D. (1951) degrees from the University of Pennsylvania. He was in the USNR from 1944 to 1946 and has been a graduate student, research staff and faculty member at the Moore School of Electrical Engineering, University of Pennsylvania from 1946 to the present where he is now Professor of Electrical Engineering. He has been continuously involved in research and consulting activities concerned with communications and radar systems, particularly concerned with techniques for processing signals and random processes. He has consulted for many years with the RCA Missile and Surface Radar Division in Moorestown, N.J., performing studies concerned with the optimization of the performance of radar and weapon systems in the presence of interference and countermeasures. More recently he has worked on the evaluation and refinement of the AEGIS-AN/SPY-1 multifunction phased array radar system. Recent and current research activities include projects concerned with large adaptive antenna arrays for space technology applications; a spaceborne array surveillance radar; an agile high resolution airborne array radar; adaptive beam forming and nulling techniques; automatic testing techniques including automatic generation of test programs.

He and his students have contributed extensively to the technical literature in communications and radar systems. He has supervised over 110 Master's Theses and over 40 Ph.D. dissertations in these areas. He was editor and co-author of *Modern Radar*, published by John Wiley and Sons, New York, 1965.

Carmen N. Campopiano received the B.Sc. (1949) and the M.Sc. (1951) in mathematics from Rutgers University. Mr. Campopiano worked for Sperry Gyroscope Co., Republic Aviation, and the Microwave Research Institute of Brooklyn Polytechnic Institute prior to joining RCA in Camden, N.J., in 1958. There he worked for a number of years in digital and spread spectrum communications systems, specializing particularly on error correction codes and digital modulation schemes. Upon transferring to RCA, Missile and Surface Radar, in Moorestown, N.J., he worked initially in satellite intelligence systems, then on aviation collision avoidance. His most recent activity has been on the AEGIS Weapon System, with emphasis on radar analysis. Mr. Campopiano is presently a Unit Manager in charge of an analytical group in the AEGIS activity. He has published in the areas of information theory, diffraction, error correction codes, and digital modulation.

Edward C. Douglas was granted a B.A. degree with honors in Physics in 1962 from the College of Wooster, Wooster, OH. His graduate work was performed in the Electrical Engineering Department at New York University, where he also worked as a graduate assistant, taught undergraduate courses, and was awarded a NSF graduate Fellowship. In 1964 he received an M.E.E. degree and, in 1969, was granted his Ph.D. Dr. Douglas became a Member of Technical Staff at RCA's David Sarnoff Research Center in Princeton, N.J., in 1969. He has worked in the area of lensless, high-resolution projection techniques and has studied the high-light-level overload characteristics of RCA's silicon vidicon. He has studied the physics of implanted ions and has worked on the application of ion-implantation techniques to integrated-circuit devices, including the fabrication of high-performance bipolar transistors, the development of implanted P-wells for CMOS structures, and the development of implanted surface guard layers for optimum packing density of CMOS structures. He has worked on the development of low-temperature, all-implant processes for the fabrication of large-array CCD imagers and has experimented with the use of very high implant energies (up to 2 MeV) for implantation into dense substrates. In 1979, Dr. Douglas became Manager of LSI Technology Development in the Solid State Technology Center of RCA Laboratories, at Somerville, N.J.

Dr. Douglas is the author of several patents, and received RCA Outstanding Achievement Awards in both 1972 and 1973. He is a member of Eta Kappa Nu, Sigma Xi, IEEE, and the Electrochemical Society.

Sangya Jain received her B.Sc. degree in chemistry from Imperial College, London University, in 1975. She spent the following year at Kings College, London University, studying for a postgraduate certificate of education. From 1976 to 1978 she worked at the British Petroleum Research Laboratories, UK, and carried out research in the field of surface science. Since 1978, she has been employed with RCA Laboratories in the Microwave Technology Center and is currently involved in the characterization of ion-implanted GaAs. At present she is also studying part-time for an M.S. in chemistry at Rugers University, New Brunswick, N.J.

Lubomir Jastrzebski completed his undergraduate studies at Warsaw University in 1970 and he received a M.S. degree in Physics from Warsaw University in 1971 and a Ph.D. degree from the Institute of Physics, Polish Academy of Science in 1974. Between 1975 and 1978 he worked in the Materials Science and Engineering Department at M.I.T. In 1978 he joined RCA Laboratories. His main area of interest is analysis of the relationships between defects affecting performance of solid state devices and defects introduced to material during processing or crystal growth process. His work has resulted in about 45 original papers published in various scientific journals and presented at international conferences. Dr. Jastrzebski is a member of the American Physical Society and American Association of Crystal Growth.

S. T. Jolly received his B.Sc. degree in Metallurgy from the University of Wales in 1939. From 1940 to 1946 he served in the British Army. From 1946 to 1952 he was employed by EMI Ltd., supervising the materials and components test and evaluation laboratory. Since 1953 he has been employed by RCA, initially as Engineering Leader responsible for the development of packaging hardware, power supplies, magnetic head design, and production for the Bizmac, 301, and 501 computers. As Manager of the Magnetic Head Design Department from 1959 to 1963, he supervised the design and development of all magnetic recording heads for professional audio, video, and digital recording, and assisted in the setup of associated production facilities. From 1963 to 1968, Mr. Jolly was an Engineering Group Leader with

RCA Defense Electronics Products, responsible for the development work in computer memories (ferrite core, plated wire, NDRO, and ROM); the automated test equipment studies including design and construction of an automated tester for computer tape recorders; and setting up a facility for the production of high-resolution photomasks to be used in the manufacture of integrated-circuit devices. Mr. Jolly was the Senior Engineer responsible for the initial design and process development of liquid-crystal displays.

His present responsibility is the development of epitaxial-growth processes and the production of gallium arsenide for solid-state microwave devices with the Microwave Technology Center located at the David Sarnoff Research Center in Princeton, N.J. In this assignment he has developed processes for the growth of thin (less than 1-μm thickness) multiple layers required in the fabrication of GaAs field-effect transistors, and has also shown feasibility of growing chromium- and oxygen-doped buffer layers on semi-insulating GaAs substrate material. He is currently developing alternative methods of chromium and iron doping to produce dislocation-free buffer layers on semi-insulating GaAs substrates for the development of improved high-speed transistors and other logic devices.

Mr. Jolly holds two patents in the field of magnetic memories and magnetic recording and one patent concerned with the construction of vapor-phase reactors.

Werner Kern received his education in chemistry in schools in Switzerland and the U.S.A. The research thesis he published in 1947, on the discovery of fluorescing carcinogenic hydrocarbons in soil, established an important new branch of environmental science. He was a research chemist with Hoffmann-La Roche in Switzerland and New Jersey, and later with Nuclear Corporation of America; there he became chief chemist directing research in radiation chemistry. In 1959 Mr. Kern joined RCA Electronic Components and Devices Division to investigate semiconductor processes by radiochemical methods, was project scientist and consultant on several research projects, and was in charge of radiological safety. Since 1964 he has been at RCA Laboratories, Princeton, N.J., as a Member of Technical Staff. He has been working in semiconductor process research, specializing in the characterization and device applications of dielectric films, chemical vapor deposition, and etching processes. From 1974 to 1979 he was project scientist for government-sponsored research contracts on glass passivation, dielectric defects, and silicon solar cells.

Mr. Kern is Vice Chairman of the Dielectric and Insulation Division of the Electrochemical Society, is a member of the American Chemical Society, the American Vacuum Society, the Electrochemical Society, and the Research Honorary Society of Sigma Xi, and is listed in *American Men and Women of Science* and *Who's Who in the East*. He is the author or coauthor of over 60 scientific publications, holds five U.S, patents, has presented numerous invited technical lectures, and has organized scientific symposia. He received an RCA Achievement Award in 1966 for his work in integrated-circuit process research, and is the recipient of the Callinen Award for 1971 of the Electrochemical Society, in recognition of his pioneering research in chemical vapor deposition. Mr. Kern received a 1973 RCA Laboratories Outstanding Achievement Award for his team contributions to the glass passivation of silicon device structures. He also coedited and coauthored a book, *Thin Film Processes,* published by Academic Press in 1978.

Frank Kolondra graduated in 1963 from New Jersey Institute of Technology with a B.S. degree in Electrical Engineering. He started to work for RCA at the Harrison plant and was responsible for all testing in the Transistor Development Shop. He spent several years with the Electron Tube Division, maintaining testing equipment in the Quality Control Department and the Chemistry and Physics Laboratory working on Nuvistor electron tubes and thermoelectric materials. After joining RCA Laboratories at Princeton, N.J., he built a 100-kilogauss Nb_3Sn superconducting magnet. Later he was active in the development of radiation-hard devices and operated the 1-million-volt Van de Graaff accelerator. He is now responsible for the ion-implantation facility.

Jacek Lagowski received his M.A. degree in Physics from Warsaw University in Poland in 1962, Doctor of Science from the Polish Academy of Sciences in 1968, and Habilitated Doctor of Science from the Polish Academy of Sciences in 1972. In 1962, he joined the Institute of Physics, Polish Academy of Sciences in Warsaw as a research staff member. In 1973 he was appointed Associate Professor and Associate Head of the Semiconductor Division. Also in 1973 he became Deputy Director in Charge of Research at the Institute of Physics, a position which he held until August 1976. In 1970, 1974 and 1975 he spent over two years at M.I.T. as a Visiting Scientist. In 1978 he joined the academic staff of M.I.T. (Department of Materials Science and Engineering). The research interests of Dr. Lagowski have been in semiconductor surfaces and interfaces, structural defects, energy conversion, electronic characterization and growth of semiconductor materials. He has published over seventy original papers. In 1974 and 1975 he received the Polish Academy of Sciences awards for outstanding scientific achievement.

Dr. Lagowski is a member of the American Physical Society, American Association for Crystal Growth and Electrochemical Society.

Shing-gong Liu received the B.S. degree in Electrical Engineering from Taiwan University, Taipei, Taiwan, in 1954, the M.S. degree in Electrical Engineering from North Carolina State College, Raleigh, in 1958, and the Ph.D. degree in Electrical Engineering from Stanford University, Stanford, California, in 1963. From 1958 to 1959, he worked with IBM Laboratories, Poughkeepsie, New York; from 1960 to 1963, he did research work on microwave ferrites in the Hansen Microwave Laboratories, Stanford University. At RCA Laboratories, Princeton, New Jersey, which Dr. Liu joined in August 1963, he has been engaged in research on the use of high-field nonlinear effects in GaAs for microwave devices and optical modulation, beam deflection devices, and avalanche-diode microwave oscillators, using both Si and GaAs materials. From 1974 to 1976, he has worked on high-efficiency solar cells for concentrator application and on GaAs Schottky diodes for low-noise mixers for satellite ground stations. Since 1977 he has been working on ion implantation in GaAs material and on the development of field-effect transistors containing ion-implanted material. He received three RCA Outstanding Achievement Awards for his work on high-power high-efficiency avalanche diodes.

Dr. Liu is a member of Phi Kappa Phi, IEEE, Sigma Xi, and the American Physical Society.

Charles W. Magee was graduated by the University of Virginia with a B.S. degree in Chemistry in 1969, and with a Ph.D. in 1973. While in graduate school at the University of Virginia, he concentrated on electrical methods of ion detection in spark-source mass spectrometry. He was also involved in the development of new types of ion sources for the mass-spectrometric analysis of solids. He joined the Technical Staff of RCA Laboratories immediately upon completion of his graduate work and is presently a member of the Materials Characterization Research Group. His work deals mainly with the trace-elemental analysis of thin solid films by means of secondary-ion mass spectrometry and spark-source mass spectrometry.

Dr. Magee is an active member of the American Society for Mass Spectrometry, having presented numerous technical papers at its National meetings. He is also a member of the steering subcommittee for the Solids and Surface Analysis Committee of the ASMS. In addition, Dr. Magee is a member of the American Vacuum Society and serves on the steering committee for the Greater New York Chapter of the AVS. He is also a member of Sigma Xi.

S. Yegna Narayan received his B.Sc. (Honors) from the University of Delhi, India, in 1959; his B.E. with Distinction from the Indian Institute of Science, Bangalore, India, in 1962; and his M S. and Ph.D. degrees from Cornell University in 1964 and 1966, respectively. His graduate research dealt with the coupling of microwave energy to electron beam-plasma systems. Since joining RCA in 1966, Dr. Narayan has been working mainly in the area of semiconductor microwave devices such as GaAs transferred-electron devices, Schottky-barrier devices, high-quality GaAs varactor diodes, GaAs field-effect transistors, and multigigabit-rate logic technology. Dr. Narayan, as Head, Microwave Device Technology, has responsibility for the development of compound semiconductor microwave devices at the Microwave Technology Center, RCA Laboratories, Princeton, N.J.

Dr. Narayan was the recipient of two RCA Laboratories Outstanding Achievement Awards; one in 1968 for his work in the development of GaAs transferred-electron device technology and the other in 1972 for the development of high-quality GaAs varactor diodes. He has also been issued five U.S. patents. Dr. Narayan is a Senior Member of the IEEE and a member of the American Physical Society.

Edwin C. Tracy completed his B.A. degree in physical science in 1968, at which time he joined RCA Laboratories to work on vapor deposition of ferromagnetic semiconductors. In 1971 he joined the Glass Research Group and worked on a variety of projects including ion depletion, plasma-generated ion injection, and reactive plasma deposition of thin films on glass surfaces. From 1975 to 1980 Mr. Tracy was involved with integrated-circuit technology as a member of the Solid State Process Research Group where he participated in the development of electrophorectic decoration techniques for detecting structual defects in passivation layers and in the deposition and characterization of silicon nitride films. He developed a microscopic method for determining the index of refraction of dielectric films on integrated-circuits. Most recently, he has been evaluating deposition techniques for antireflection coatings on silicon solar cells. In April 1980 he joined the technical staff of SERI in Golden, Colorado.

Mr. Tracy is author of co-author of four publications and holds three joint patents in plasma processing. He is a member of the Electrochemical Society, the American Vacuum Society, and the American Association for the Advancement of Science.

L. C. Upadhyayula received the B.Sc. degree in Physics and the M.Sc. in Applied Physics from Andhra University, India, in 1955 and 1958, respectively, and the Ph.D. in Engineering from Brown University in 1968. During 1958–59, he was a trainee in the Atomic Energy Establishment, Bombay, India. From 1959 to 1964, he worked in the Electronics Division of the Atomic Energy Establishment. His work was in the area of nuclear electronic instrumentation. From 1964 to 1967, he was a research research assistant and teaching assistant in engineering at Brown University, where he was engaged in the study of electrical transport properties of semiconductors. During 1968–69, Dr. Upadhyayula was a Post Doctoral Fellow in Engineering at Brown University, studying tunneling through superconducting metal-insulator-metal structures at cryogenic temperatures. In 1969, Dr. Upadhyayula joined the Microwave Technology Center at RCA Laboratories in Princeton, N.J. His work at RCA includes transferred-electron amplifiers and oscillators, high-efficiency IMPATTs, and transferred-electron logic devices. He has published several technical papers in these areas. He is also currently engaged in the development of GaAs MESFET technology for MSI and LSI logic circuits.

He received general proficiency awards in high school and was awarded a General Telephone and Electronics Fellowship in 1967–68 for his graduate study. In 1970, he received an RCA Laboratories' Outstanding Achievement Award for a team effort in the development of GaAs transferred-electron amplifiers. He is a member of Sigma Xi and IEEE. He was issued nine U.S. patents and has several disclosures pending.

Chung P. Wu received the B.S., M.S., M.Phil., and Ph.D. degrees in Physics from Yale University in 1965, 1966, 1967, and 1968, respectively. He was a research staff physicist at the Yale Electron Linear Accelerator Laboratory from 1968 to 1970, working on photonuclear reactions and neutron time-of-flight spectroscopy. From 1970 to 1972 he was an Assistant Professor of Physics at Nanyang University in Singapore. Since 1973, Dr. Wu has been a Member of Technical Staff at RCA Laboratories, Princeton, N.J. He has worked on different techniques for determining the electrically active ion-implanted doping profiles, the utilization of ion implantation in the fabrication of semiconductor devices, and the characterization and evaluation of such devices. He is currently working on the laser annealing of semiconductor materials, including polysilicon, crystalline silicon, SOS, and GaAs, for the fabrication of solar cells, devices, and circuits.

Dr. Wu has more than 20 technical publications and 15 patents granted or pending. He is a member of the American Physical Society, IEEE, and Sigma Xi.